



2019

PATHWAY CONNECTIVITY IN AN EPIGENETIC FLUVIOKARST SYSTEM: INSIGHT FROM A NUMERICAL MODELLING STUDY IN KENTUCKY USA

Ethan Adams

University of Kentucky, ethanladams@gmail.com

Digital Object Identifier: <https://doi.org/10.13023/etd.2019.322>

[Right click to open a feedback form in a new tab to let us know how this document benefits you.](#)

Recommended Citation

Adams, Ethan, "PATHWAY CONNECTIVITY IN AN EPIGENETIC FLUVIOKARST SYSTEM: INSIGHT FROM A NUMERICAL MODELLING STUDY IN KENTUCKY USA" (2019). *Theses and Dissertations--Civil Engineering*. 88.

https://uknowledge.uky.edu/ce_etds/88

This Master's Thesis is brought to you for free and open access by the Civil Engineering at UKnowledge. It has been accepted for inclusion in Theses and Dissertations--Civil Engineering by an authorized administrator of UKnowledge. For more information, please contact UKnowledge@lsv.uky.edu.

STUDENT AGREEMENT:

I represent that my thesis or dissertation and abstract are my original work. Proper attribution has been given to all outside sources. I understand that I am solely responsible for obtaining any needed copyright permissions. I have obtained needed written permission statement(s) from the owner(s) of each third-party copyrighted matter to be included in my work, allowing electronic distribution (if such use is not permitted by the fair use doctrine) which will be submitted to UKnowledge as Additional File.

I hereby grant to The University of Kentucky and its agents the irrevocable, non-exclusive, and royalty-free license to archive and make accessible my work in whole or in part in all forms of media, now or hereafter known. I agree that the document mentioned above may be made available immediately for worldwide access unless an embargo applies.

I retain all other ownership rights to the copyright of my work. I also retain the right to use in future works (such as articles or books) all or part of my work. I understand that I am free to register the copyright to my work.

REVIEW, APPROVAL AND ACCEPTANCE

The document mentioned above has been reviewed and accepted by the student's advisor, on behalf of the advisory committee, and by the Director of Graduate Studies (DGS), on behalf of the program; we verify that this is the final, approved version of the student's thesis including all changes required by the advisory committee. The undersigned agree to abide by the statements above.

Ethan Adams, Student

Dr. James Fox, Major Professor

Dr. Timothy Taylor, Director of Graduate Studies

PATHWAY CONNECTIVITY IN AN EPIGENETIC FLUVIOKARST SYSTEM:
INSIGHT FROM A NUMERICAL MODELLING STUDY IN KENTUCKY USA

THESIS

A thesis submitted in partial fulfillment of the requirements
for the degree of Master of Science in Civil Engineering
in the College of Engineering at the University of Kentucky

By

Ethan Adams

Lexington, Kentucky

Director: Dr. James Fox, Professor of Civil Engineering

Lexington, Kentucky

2019

Copyright © Ethan Adams 2019

ABSTRACT OF THESIS

PATHWAY CONNECTIVITY IN AN EPIGENETIC FLUVIOKARST SYSTEM: INSIGHT FROM A NUMERICAL MODELLING STUDY IN KENTUCKY USA

Fluviokarst landscapes are dominated by both fluvial and karst features. Interpreting hydrologic pathways of fluviokarst can be confounded by the unknown connectivity of the various flow regimes. A combined discrete-continuum (CDC) hybrid numeric model for simulating the surface and subsurface hydrology and hydraulics in fluviokarst basins was formulated to investigate fluviokarst pathways. This model was applied to the Cane Run Royal Springs basin in Kentucky USA. *A priori* constraints on parameterization were avoided via multi-stage optimization utilizing Sobol sequencing and high performance computing. Modelling results provide evidence of hydrologic pathways dominated by fracture flow, epikarst transfer and runoff. Fractures in karst basins with high fracture-matrix permeability ratios may influence both springflow and streamflow. Swallet features can be as important as spring features as they are sink features in streamflow during hydrologic events. Inflections in spring hydrographs represent shifts in the surface-subsurface connectivity via the fractures, as opposed to shifts in dominant storage zones. Existing methods of dual- and triunal hydrograph separation of karst springflow may not be directly transferrable to fluviokarst springs. The numerical model herein has advantages of suggesting dominant pathways in complex terrane and highlighting unforeseen surface-subsurface connectivity. However, disadvantages include computational expense and previous site studies.

Keywords: karst SWAT, combined discrete-continuum, karst hydrology, swallet, estevelle

Ethan Adams

05-09-2019

PATHWAY CONNECTIVITY IN AN EPIGENETIC FLUVIOKARST SYSTEM:
INSIGHT FROM A NUMERICAL MODELLING STUDY IN KENTUCKY USA

By

Ethan Adams

Dr. James Fox

Director of Thesis

Dr. Timothy Taylor

Director of Graduate Studies

05-09-2019

Acknowledgements

The following thesis benefitted from the input of several people. Firstly, I would like to thank my Thesis Chair, Dr. James Fox, for his support and encouragement. I would also like to thank the other members of my Thesis Committee: Dr. Scott Yost and Dr. Junfeng Zhu. I would like to thank the University of Kentucky Civil Engineering Department for providing me with academic support throughout my studies. Finally, I would like to thank my parents and my wife, Holly, for their love and encouragement.

Table of Contents

Acknowledgements	iii
List of Tables	vi
List of Figures	vii
Chapter 1 Introduction	1
Chapter 2 Theoretical Background	6
Chapter 3 Study Site	10
Chapter 4 Methods	23
4.1) Model Formulation Overview	23
4.2) Model Equations	29
4.2.1) Surface and Soil Hydrology Equations	29
4.2.2) Inputs for the GW Model across the Land Surface	37
4.2.3) Surface Streamflow	38
4.2.4) Swallets	41
4.2.5) Epikarst	45
4.2.6) Vadose Zone	47
4.2.7) Fracture Network	50
4.2.8) Aquitards and Perched Water	54
4.2.9) Saturated Rock Matrix	57
4.2.10) Phreatic and Epiphreatic Conduits	61
4.2.11) Springflow	63
4.2.12) Fracture to Matrix Flux	63
4.3) Modeling Inputs, Discretization, and Parameterization	64
4.3.1) Model Inputs and Discretization	64
4.3.2) Model Parameterization	69
4.4) Model Setup	71
4.5) Model Evaluation	73

4.5.1) Calibration and Validation	73
4.5.1.1) Stage One: SWAT	74
4.5.1.2) Stage Two: Stream and Groundwater Model	75
4.5.2) Sensitivity and Uncertainty Analysis	77
Chapter 5 Results	101
5.1) Model Evaluation Results	101
5.1.1) Calibration and Validation of SWAT Model	101
5.1.2) Calibration and Validation of Stream and GW Model	102
5.1.3) Sensitivity and Uncertainty Analysis of SWAT Model	105
5.1.4) Sensitivity and Uncertainty Analysis of Stream and GW Model	105
5.2) Pathways during Hydrologic Events and Recession Periods.....	107
5.3) Annual Averages of Karst Pathways	110
5.4) Residence Time and Storage Estimates	111
Chapter 6 Discussion	132
6.1) Net Hydraulic Pathway Results	132
6.2) Fluviokarst Features	134
6.3) Implications for Studying Fluviokarst Springflow	136
6.4) Advantages and Disadvantages for the Numeric Model for Fluviokarst	139
Chapter 7 Conclusion	144
List of Symbols	146
References	151
Vita	161

List of Tables

Table 1: Geospatial Data Sources	16
Table 2: Model Inputs	79
Table 3: Swallet Coordinates	80
Table 4: Weather Data Sources	81
Table 5: Conduit Inputs	82
Table 6: Swallet Diameters	83
Table 7: Groundwater Inputs	84
Table 8: Stream Reach Inputs	85
Table 9: Karst Model Parameters Ranges	86
Table 10: SWAT Parameter Sets used in Cane Run Watershed and Performance of Set in the Upper South Elkhorn Watershed	87
Table 11: Comparison between Upper South Elkhorn and Cane Run Creek Watersheds	88
Table 12: Initial and Final SWAT Parameter Selection and Parameter Ranges	89
Table 13: Karst Model Parameters Calibrated Values	113
Table 14: Best Model Run Performance	114
Table 15: Sensitivity Analysis Results for SWAT Parameters in Upper South Elkhorn	115
Table 16: Sensitivity Analysis Results for Karst Parameters on Spring Discharge	116
Table 17: Sensitivity Analysis Results for Karst Parameters on Streamflow	117
Table 18: Karst Pathways	118
Table 19: Fracture Storage Sources	119
Table 20: Mean Residence Times for Karst Features	120
Table 21: Mean Storage Volume in Karst Aquifer Storage Reservoirs	121

List of Figures

Figure 1: Conceptual Diagram of the Mature Fluviokarst System	5
Figure 2: Fluviokarst Pathway Diagram	9
Figure 3: Study Site	17
Figure 4: Groundwater Cells	18
Figure 5: Cane Run Bed Elevations	19
Figure 6: Hypothesized Conduit Profile	20
Figure 7: KWIS Well Locations	21
Figure 8: KWIS Stage Recordings	22
Figure 9: Stratigraphic Curvature	90
Figure 10: Averaged Stratigraphic Curvature	91
Figure 11: Average Stratigraphic Curvature over All Groundwater Cells	92
Figure 12: SWAT Spatial Discretization	93
Figure 13: Averaged Cane Run Bed Elevations	94
Figure 14: Average Surface Elevations	95
Figure 15: Centroids of Groundwater Cells	96
Figure 16: Active Groundwater Wells	97
Figure 17: Model Workflow Schematic	98
Figure 18: Model Calibration Flow Diagram	99
Figure 19: Map of South Elkhorn Watershed	100
Figure 20: Spring Discharge for a Well Performing Model Run	122
Figure 21: Simulated and Observed Spring Hydrographs for two Hydrologic Events	123
Figure 22: Simulated and Observed Stream Hydrographs for two Hydrologic Events	124
Figure 23: Model Uncertainty	125
Figure 24: Model Results for 2-Month Window	127
Figure 25: Model Results during Extreme Hydrologic Events	129

Figure 26: Model Results during Moderate Hydrologic Events 131

Figure 27: Major hydrologic pathways of the fluviokarst systems evidenced by
the numerical modelling 143

Chapter 1 Introduction

Rainfall enters epigenetic fluviokarst and its possible pathways to an outlet of a basin are many. Fluviokarst landscapes are dominated by both fluvial and karst features, and hydrologic pathways may be dominated by the fluvial processes, subsurface karst flow, or connectivity of both features (Phillips and Walls, 2004). Surface streams can transfer runoff out of a fluviokarst basin, similarly to non-karst basins. Landscape sinkholes and sinking streams can pirate the fluvial system to the subsurface while soil water may transfer to epikarst, conduits, fracture networks and rock matrix. This subsurface morphology reflects the presence of a range of bedrock porosities, arising from the dissolution of calcium carbonate rock that can often span several orders of magnitude (White, 2002). Knowledge of water flow via different pathways allows for improved modelling of water security, transport and fate of pollutants, and water resources in karst basins.

Our concept of the potential karst pathways of water has taken shape in recent years (Hartmann et al., 2014), however connectivity of fluvial and karst pathways as well as their quantifying the mixed pathways influence on the hydrograph remains as knowledge gaps. Less obvious fluvial-karst connectivity can occur when swallets reverse flow from the subsurface to the surface streams as well as fracture network overflows (Chen and Goldscheider, 2014; Hensley and Cohen, 2014), but studies of these processes for fluvial karst are few. The relative timing and contribution of different pathways on the karst spring hydrograph has been studied for karst springs (Bicalho et al. 2017; Hosseini et al. 2017; Zhang et al. 2018), but extension of these concepts to fluviokarst basins is understudied.

For example, hydrologists have sometimes separated karst hydrographs into quick-, intermediate- and slow-flow pathways (Baedke and Krothe 2001; Kovács and Perrochet 2008; Fiorillo 2011). Recent studies have shown this triunal classification does not explain spring solute concentrations in fluviokarst (Husic et al. 2019b). It is possible that traditional hydrograph separation methods are overdetermined for the suite of pathways present in mature karst systems (Figure 1). Successful separation of the spring signal into its constituent pathways is important for understanding flow and solute transport during wet versus dry times of the year, extreme versus moderate events, and baseflow recession.

We argue that filling the knowledge gaps of timing and relative contributions of fluviokarst pathways can be addressed with karst numerical modelling. Numerical modelling of karst basins receives some criticism because models can easily become data-starved, over-parameterized, or contain deficiencies in model structure (e.g., Hartmann et al. 2014; Chang et al. 2019; Husic et al. 2019b). Nevertheless, numerical modelling results can be useful and defensible when the model is appropriately scaled, represents known morphology and processes in the basin, has a wide variety of data, and considers all acceptable solutions during model evaluation (Husic et al. 2019b). To remedy potential karst modelling pitfalls, it is helpful to study watersheds with extensive datasets when karst models with increased complexity are used to address knowledge gaps of processes. In the present study, we embrace this sentiment and investigate residence time and pathway contributions by numerical modelling the data-rich Cane Run Royal Spring karst basin in Kentucky USA. The karst system is characterized as the most heavily studied and modelled karst basin in the karst dominated terrain of Kentucky, mature fluviokarst geomorphology with almost all of the morphologic features of epigenetic karst (Husic et

al., 2019a, b). In addition, we avoid bias of the modeller by relaxing *a priori* constraints on parameterization and instead we optimized the model via a multi-stage approach using thousands of Sobol sequences on the University of Kentucky's new supercomputer cluster, the Lipscomb Computer Cluster, rated at over 104 teraflops.

Herein, we develop a numerical model for mature fluviokarst and specifically set up and apply the model to the Cane Run-Royal Spring basin to answer fluviokarst connectivity and relative contribution questions for karst pathways. The new model integrates numerous model components from the recent karst modelling literature. Rather than numerical modelling advancement of a specific karst feature, the novelty of the proposed model is its comprehensive nature, simulation of spatially heterogeneous pathways, and ability to couple the timescales of water transported through the many morphologic components. The features represented in the model include surface runoff, stream flow, the soil layer, sinkhole depression drainage, in-stream swallet pirating, the epikarst, fracture flow, unsaturated and saturated matrix flow, aquitards and perched water, overflow springs, and conduit flow. In addition to the comprehensive nature of our modelling, there are a number of features of the modelling that have not been widely reported, to our knowledge, in the karst literature including: the numerical treatment of swallets in the stream corridor and the numerous conditions for which they can exist (i.e., filling, overtopping swallets, emptying); and we use a combined-discrete continuum that explicitly represents a fracture network, vadose zone (unsaturated) flow, an epikarst zone, and perched aquifers. The developed numerical model is semi-lumped, in which surface and subsurface domains are discretized into sub-basins, and inter- and intra-transport of

morphologic components is modeled using conservation laws or their semi-empirical derivatives.

Our motivation for this study was to gain insight, through numerical modelling, on the relative impact of various pathways on the spring and overflow hydrographs, and pathway connectivity of a mature fluviokarst basin. We seek knowledge of the relative importance of the different water pathways in mature fluviokarst at different times of the year, for a range of hydrologic event magnitudes, and cumulatively. Specifically, our objectives were to: (1) develop and apply a numerical model for mature fluviokarst, (2) use the model to gain insight of water pathways impact on spring and overflow hydrographs, (3) use the model to quantify water residence time along different pathways in mature fluviokarst, and (4) analyze and discuss “pathway classification” in mature fluviokarst basins.

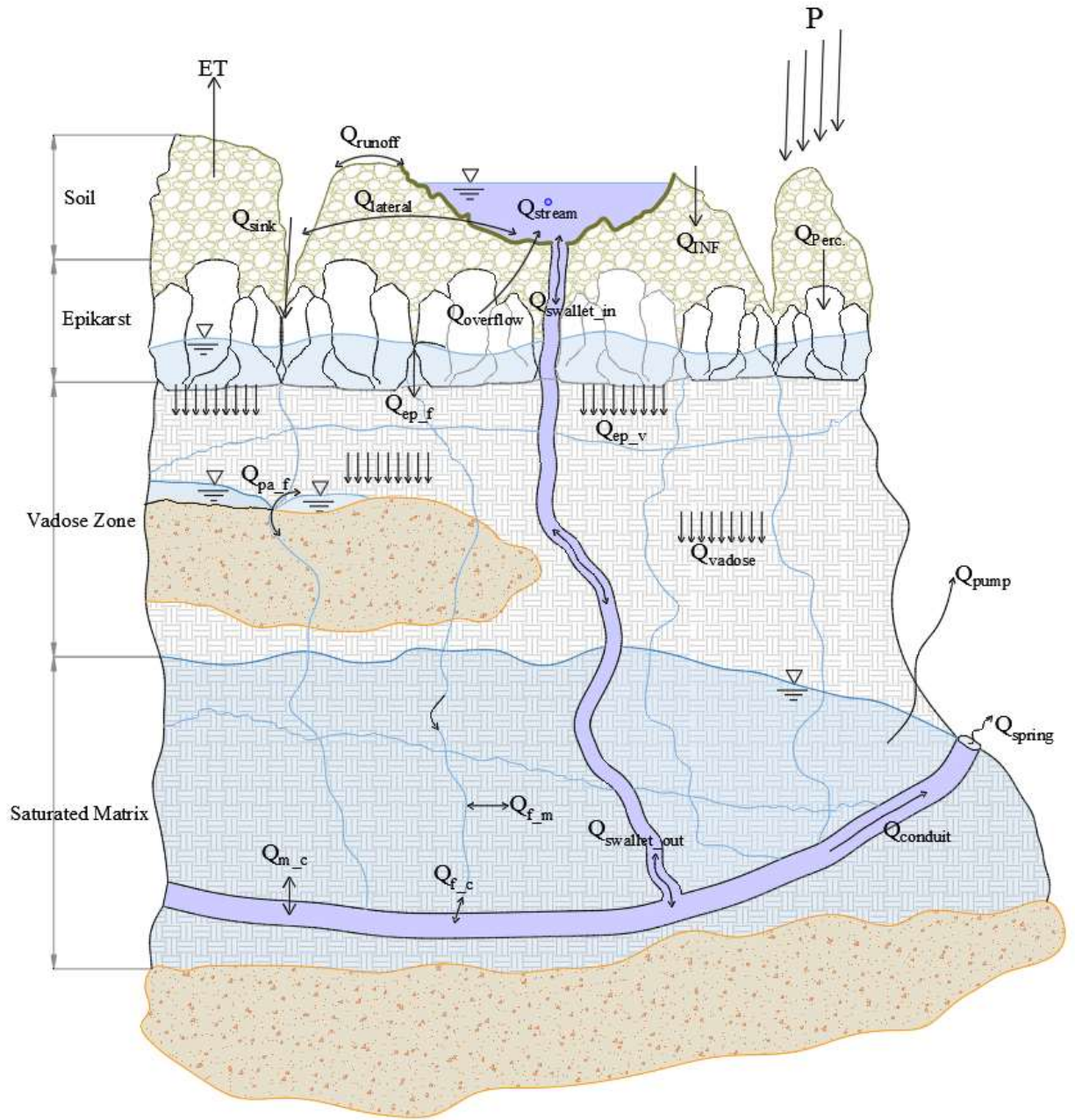


Figure 1. Conceptual Diagram of the Mature Fluviokarst System

Chapter 2 Theoretical Background

We focus our theoretical background on a classification of hydrologic systems defined as mature fluviokarst. ‘Mature karst’ specifies carbonate bedrock with pronounced dissolution and multiple levels of porosity such as turbulent conduit flow, fracture flow, and Darcian flow pathways can exist in the subsurface (White, 1999; Hartmann et. al., 2013). The ‘fluviokarst’ classification invokes the presence of runoff and streamflow at the surface of the landscape, water storage and transfer across numerous karst subsurface features with varying porosity, and the potential for high connectivity between surface and subsurface flow via karst sinkholes and springs. We include the presence of a soil layer, surface streams, both landscape and in-stream sinkholes, and a subsurface phreatic or epiphreatic cave network. Our theoretical treatment is rather robust in its inclusion of fluvial and karst morphology and therefore encompasses morphology of karst systems studied by past researchers (Smart and Freidrich, 1986; Doerflinger and Zwahlen, 1998; Drysdale et al., 2001; White, 2002; Massei et al., 2003; Herman et al., 2008; Hartmann et al., 2014). The theoretical context emphasizes phreatic conduit networks that are typical of water-table and looping cave systems, such as elongated branchwork or anastomotic maze configurations (e.g., Ford and Ewers 1978; Jouvès et al., 2017). The context herein is limited to epigenic (i.e., epigenetic), gravity driven processes, and we do not explicitly account for hypogenic recharge from a deep pressure driven source of groundwater or vadose zone caves.

The water pathways through a fluviokarst basin rely on the surface and subsurface geomorphology. The geomorphology of mature fluviokarst is depicted in Figure 1 and includes a number of commonly cited features. In the figure, land surface geomorphology includes a soil layer, stream network, sinkholes across the landscape, and sinkholes in the stream corridor. The most highly dissolved subsurface geomorphology includes sinking streams leading to vertical conduits and a network of phreatic conduits. Intermediate dissolved bedrock includes an epikarst at the top of the bedrock with higher dissolution than deeper bedrock, a network of active fractures, an unsaturated granular rock matrix, and a phreatic granular rock matrix. Near zero transfer features are included as well, such as limestone members formed with high clay or silt content and in turn low to impermeable quality. These low permeability aquitards create perched aquifers and limit fracture development relative to the surrounding rock matrix. In general, the description of the above geomorphologic features is consistent with definitions in seminal work by others (e.g., Smart and Freidrich, 1986; Doerflinger and Zwahlen, 1998; White, 2002; Hartmann et. al., 2013).

The water pathways, their relative contribution to the hydrograph, and their transit times depend on the storage capacity of karst geomorphology and the hydrologic transfer rates within and between each geomorphologic feature. The hydrologic transfer rates are shown as Q 's in Figure 1. Precipitation fell at the land surface either infiltrates to the soil (Q_{inf}) or runs off to sinkholes or the stream network (Q_{sur}). Soil water moves laterally to sinkholes or the stream network (Q_{lat}), percolates vertically through the soil profile to the epikarst (Q_{perc}), or re-enters the atmosphere through evapotranspiration (ET). Stream water moves down gradient in the stream network (Q_{trib} or Q_{stream} , where the former indicates

first order tributary flow and the latter indicates a higher order or trunk stream) or moves vertically to the subsurface *via* swallet holes ($Q_{swall-in}$). Swallet flow ($Q_{swall-in}$) reverses direction during upwelling of groundwater flow to the stream. Water stored in the epikarst percolates vertically to the vadose zone (Q_{ep-v}) or moves to the fracture network (Q_{ep-f}), where it is generally considered the latter is activated during hydrologic events and wet times of the year (Tritz et al., 2011). Sinkhole water also moves to the fracture network (Q_{sink}), although excess soil erosion clogs and deactivates sinkholes. Water stored in the vadose zone percolates as unsaturated flow (Q_v) until it reaches the water table. Water in perched aquifers or phreatic matrix exchanges with fractures (Q_{pa-f}) or higher porosity conduits (Q_{f-c}). Depending on human population density and land uses, water leaves the aquifer via well pumping (Q_{pump}). Water conveys through conduits to springs (Q_c). During very wet conditions such as an extreme hydrologic event, fracture networks and epikarst reaches their capacity, and overflow occurs to the stream network (Q_{over}), which leaves the basin via surface water outlets.

Herein, we numerically model the hydrologic transfer rates, time-varying mass storage, and transit time associated with karst geomorphologic features. We then use the modelling results to analyze the relative contribution and dimensionless transit time along the 20+ pathways shown in Figure 2. The analyses is performed for a mature fluviokarst system at different times of the year, for a range of hydrologic event magnitudes, and cumulatively over a multi-year simulation period. Examples of karst pathways shown in Figure 2 include: precipitation to soil to epikarst to fracture to conduit to spring; or precipitation to runoff to stream to swallet to conduit to spring.

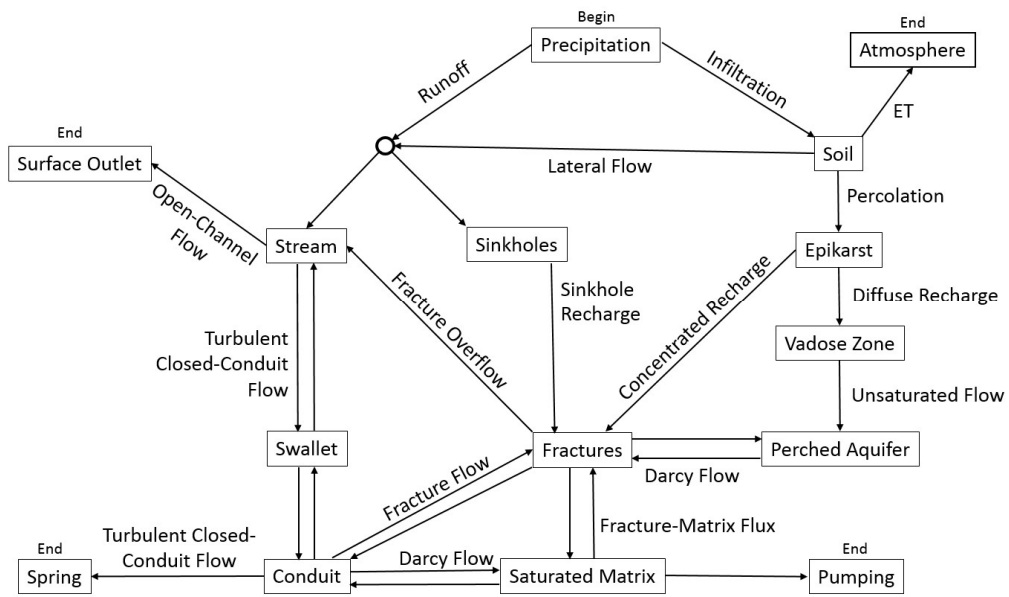


Figure 2. Fluviokarst Pathways Diagram.

Chapter 3 Study Site

The data-rich Cane Run Royal Spring karst basin in inner bluegrass region of Kentucky USA was selected as a study site for developing a numerical model that will help provide knowledge about water pathways in mature fluviokarst. 55% of the state of Kentucky USA is underlain by bedrock with karst potential, and the Cane Run Royal Spring basin has been the most heavily studied karst basin in the state. The system is so heavily studied because (i) it classifies as highly characteristic of mature fluviokarst basins for the region with almost all of the morphologic features of epigenetic karst occurring to some degree (e.g., see Figure 1) and (ii) at the same time is located just 10 km from the Kentucky Geological Survey's headquarters and the University of Kentucky research institution. In turn, researchers have spent the past 40 years studying the system and performing tracer tests, lidar mapping, electrical resistivity mapping, research well drillings and data collection, isotope tracer studies, data-driven water budgets, and routine long term and event-based water quality measurements (Cressman, 1967; Spangler, 1982; Thrailkill and Gouzie, 1984; Cressman and Peterson 1986; Thrailkill et al., 1991; Drahovzal et al. 1992; Taylor, 1992; Paylor and Currens, 2004; Zhu et al., 2011; Currens et al., 2015; Sawyer et al, 2015; Tibouo, 2016; Husic et al., 2017a and 2017b, Bandy et al., 2019; Husic et al., 2019a and 2019b). The result has been a collection of a suite of data sources helpful for pre-characterization of the systems geomorphology as well as inputs and parameters in numerical modelling.

The Cane Run Royal Spring karst basin is located in the Inner Bluegrass region of central Kentucky (Figure 3), which is characterized by gently rolling topography with abundant karst features such as sinkholes across the landscape (Paylor and Currens 2004). The sinkholes and their drainage basins have been mapped and ground-truthed in recent years by the Kentucky Geological Survey (Tibouo, 2016). This topography makes the land surface suitable for agricultural use, and much of it is horse farm pasture (UKCAFE, 2011). The climate is temperate (MAT: 13.0 ± 0.7 °C; MAP: $1,170 \pm 200$ mm). The underlying soil in the watershed is silt-loam with approximately 85% of the soil in the Maury series and 15% in the Lowell series. Approximately 40% of the watershed has shallow surface slopes (0-3%), 50% with moderate slopes (3-6%) and 10% with steeper slopes (>6%).

The Cane Run surface stream originates from north of Lexington, Kentucky, flows northwest, and shares a significant portion of drainage area with Royal Spring basin (58 km²) through numerous sinkholes that connect surface water to the underlying karst aquifer feeding Royal Spring. More than twenty swallets, estavelles, and sinks have been identified within Cane Run creek (see Figure 4). The swallet equivalent diameters range from approximately 10 centimeters to 5 meters at the creeks bed surface. Flow pirating by the swallets result in the creek being dry for approximately 90% of the year (Husic et al., 2017a).

The stream's fluviokarst features and surrounding subsurface of Royal Spring aquifer are formed in Middle Ordovician aged limestones, named Lexington Limestone, with interbeds of thin shales (Thraillkill, 1984; Cressman and Peterson 1986). Epikarst features are visible throughout the watershed both in naturally exposed karren as well as roadcuts (Husic et al., 2019 b). Subsurface geology, pathways and aquifer boundaries have

been mapped with dye traces, water discharge and temperature measurements, bore holes, and geological surveys (Spangler, 1982; Taylor, 1992; Paylor and Currens, 2004; Zhu et al., 2011; Currens et al., 2015). Karst geomorphology and preferential groundwater flow in the Royal Spring basin is strongly influenced by the presence of faults and joints. Major faults trend northeast to southwest, whereas predominant joints and minor faults preferentially trend north to northwest and southeast (Drahovzal et al. 1992). The local syncline indicates a northwest axis with the faults paralleling this axis (Cressman, 1967). A stratigraphic low occurs near the longitudinal three-quarter point of the basin's drainage near the Kentucky Horse Park (see Figure 5). Geological survey and exposed bedrock indicate the Lexington Limestone is fractured throughout, and is likely coincident with the surface of bedding planes and joints (Ewers, 1982; Filipponi., 2009). Regional and local structures likely influencing fracture density includes regional uplift of the Cincinnati Arch and Jessamine Dome and by local structural deformations (McFarlan, 1943; Ford and Ewers 1978; Florea et. al., 2005). The net groundwater flow trends from the southeast to the northwest to the base level of North Elkhorn Creek (Thrailkill et al., 1991; Husic et al., 2019a). Limestone members formed with high clay or silt content locally act as aquitards in the Lexington Limestone, and geologic surveys mapped the depth and named these members including the Cane Run Bed, Brannon Member, argillaceous limestone members, and fossiliferous shale and limestone members (Cressman, 1967; Miller, 1967; MacQuown and Dobrovolny, 1968). We found additional validation of the cross section geology using hillside springs at the elevations of the aquitards, perched aquifers found in well drillings, and correlation analyses of wells located normal to the primary groundwater flow direction.

Water flow from the fluviokarst features and surrounding limestone matrix converges to a phreatic conduit 18 meters below the surface that flows northwest and surfaces at Royal Spring. Thrailkill et al. (1991) and Paylor and Currens (2004) speculated that flow feeding Royal Spring is concentrated through a major conduit and the flow in the conduit is fast and likely turbulent. Later, electrical resistivity surveys helped locate the conduit at the near center of the groundwater basin in the Kentucky Horse Park shown in Figure 4 (Zhu et al., 2011). The phreatic conduit is approximately 5 m wide and 1 m high, as identified through downhole video, tracer testing, and acoustic methods (Husic et al., 2017a). The work of Thrailkill et al. (1991) hypothesized the conduit profile would follow an exponential function through the groundwater basin. Further evidence from resistivity measurements (Landrum et al., 2013), well drilling directly intersecting the conduit, the elevation of the North Elkhorn base level, and the elevation of Royal Spring suggests the conduit profile follows a bedding plane approximately 14 m below Cane Run Bed. This theory is in general consistent with other conduits in this Kentucky region and more generally phreatic conduit development is strongly controlled by bedding planes and water table boundaries (Fillipponi et al., 2009; Ford and Ewers 1978; Malard et al., 2015). The result is positive gradient conduit profile to an elevational low at Kentucky Horse Park, and then a net adverse gradient to Royal Spring (see Figure 6). The adverse gradient produces the phreatic condition for much of the conduit (Husic et al., 2017a). The conduit outlet at Royal Spring, rather than North Elkhorn Creek, is suggested to be the result of local, secondary fractures creating a preferred pathway with greater hydraulic efficiency. Sawyer et al. (2015) recently used time-lapse electrical resistivity survey combined with salt injection and suggested the conduit is likely accompanied by branches of smaller conduits,

from which they form an anastomosing conduit network prior to resurfacing at Royal Spring.

The Royal Spring springhead has the largest base flow discharge of any spring in the region and conveys perennial flow from the phreatic conduit (Currens et al., 2015). Royal Spring (243 m a.s.l.) has an average perennial discharge of $0.67 \text{ m}^3 \text{ s}^{-1}$, and supplies water for distilleries, grist mills, horse farms, and crop irrigation, and the main springhead serves as the raw municipal water source for the City of Georgetown, Kentucky.

Materials used to assist with setting up, carrying out, and calibrating the numerical modelling research included existing geospatial and subsurface geology models, weather data from meteorological stations and generated weather data, soil data, well stage data, streamflow gage data, springflow gage data, and supercomputing resources. Geospatial and geology materials used are provided in detail in Table 1 and included KSG sinkhole maps, aquifer boundary maps, swallet maps, land use maps, stream flow network maps, soil maps, topography models, mapping of the streams bathymetry, and the previously mentioned geologic cross sections and conduit profiles. Meteorological data were available from the Bluegrass Airport (NOAA ID: USW00093820) as well as three nearby rain gauges (NOAA IDs: US1KYSC0001, US1KYFY0009, and USC00153194). The weather stations recorded relative humidity, temperature, and wind speed but were also supplemented using the WXGEN weather generator model (Sharpley and Williams, 1990). Soil temperature and moisture data was available at Spindletop Research Farm near the center of the groundwater basin (UKAg, 2007). Numerous well data was available for model validation (see Figure 7 and 8). Wells directly intersecting the conduit provided data for validating stage in concentrated flow of the aquifer. Wells intersecting perched

aquifers provided validation of stage above the impermeable layers. Streamflow stage data for estimating discharge was available for the surface stream outlet (see Figure 3, see Husic et al., 2017a for stream data details). Streamflow stage data was also available on two tributary streams; one dominated by urban/suburban land use and the second agricultural. Gaging stations located upstream of any in-stream swallets provided secondary calibration and validation data for hydrologic modelling. Streamflow data was also available for Cane Run Creek at a gage operated by the United States Geological Survey (USGS 03288180). Additionally, historic streamflow data was available from a gage formerly operated by the USGS (USGS 0328200). Springflow data was available from the USGS at Royal Spring (USGS 03288110). Royal Spring discharges into a pool behind the USGS gage, and serves as the drinking water source for Georgetown, KY. Raw water intake rates were provided by the Georgetown Municipal Water and Sewer Service to adjust the USGS gage data to accurately reflect the discharge at Royal Spring. Static head data for the karst conduit was available from stage recorders in a well drilled into the conduit and provided by the Kentucky Geological Survey. Computer resources included a number of existing software that assisted with calculations including: ArcMap 10.4.1, ArcSWAT 2012 version 10.4.19, SWAT-CUP version 5.1.6.2, and MATLAB R2017a. Computer resources also included an institutionally shared high performance computing cluster (Lispcomb Cluster) with 4800 processor cores, 18TB of RAM, and 1PB of high-speed disk storage.

Table 1. Geospatial Data Sources

Dataset	Title	Origin
Well Locations	Water Well and Spring Location Map	Kentucky Groundwater Data Repository
Soil	Kentucky Soil Survey (gSSURGO)	USDA Geospatial Data Gateway
Land Use	National Land Cover Dataset 2116 Kentucky	USDA Geospatial Data Gateway
30-m DEM	National Elevation Dataset 30-meter 37084 Winchester & 38084 Louisville	USDA Geospatial Data Gateway
5-ft DEM	Kentucky From Above 5-ft DEM Tiles: N082-N089, E298-E302	Kentucky Elevation Data and Aerial Photography Program
Sinkhole Locations	LiDar Sinkholes	Kentucky Geologic Survey
Sinkhole Drainage Area	GIS Sinkhole Coverage for the Karst Area of Kentucky	Kentucky Geologic Survey and Kentucky Speleological Survey
Geologic Stratigraphy	24k Structure Contours	Kentucky Geologic Survey
Hydrography	National Hydrography Dataset 051002050 Lower Kentucky	USDA Geospatial Data Gateway

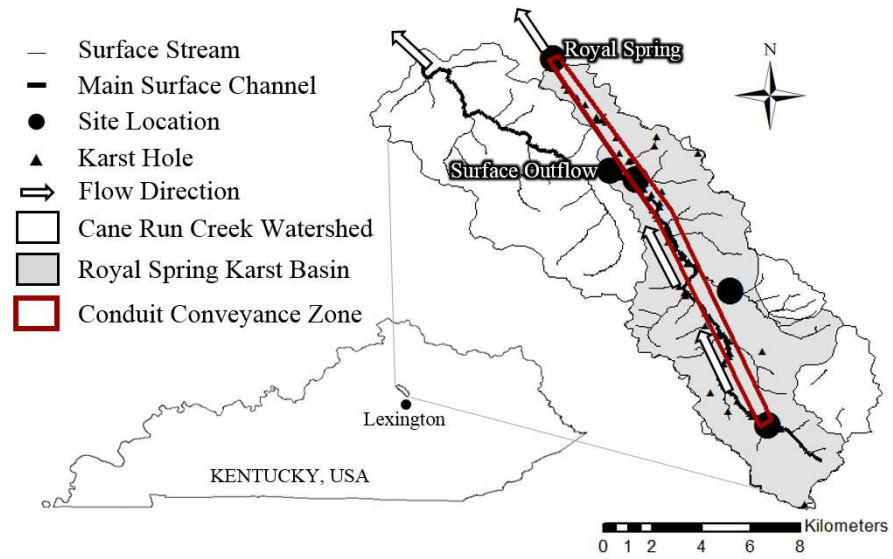


Figure 3. Study Site. Adapted from Husic et al., 2017a. Site locations are the five long term monitoring stations for the basin. “Royal Spring” and “Surface Outflow” are the groundwater and surface water exits from the karst basin.

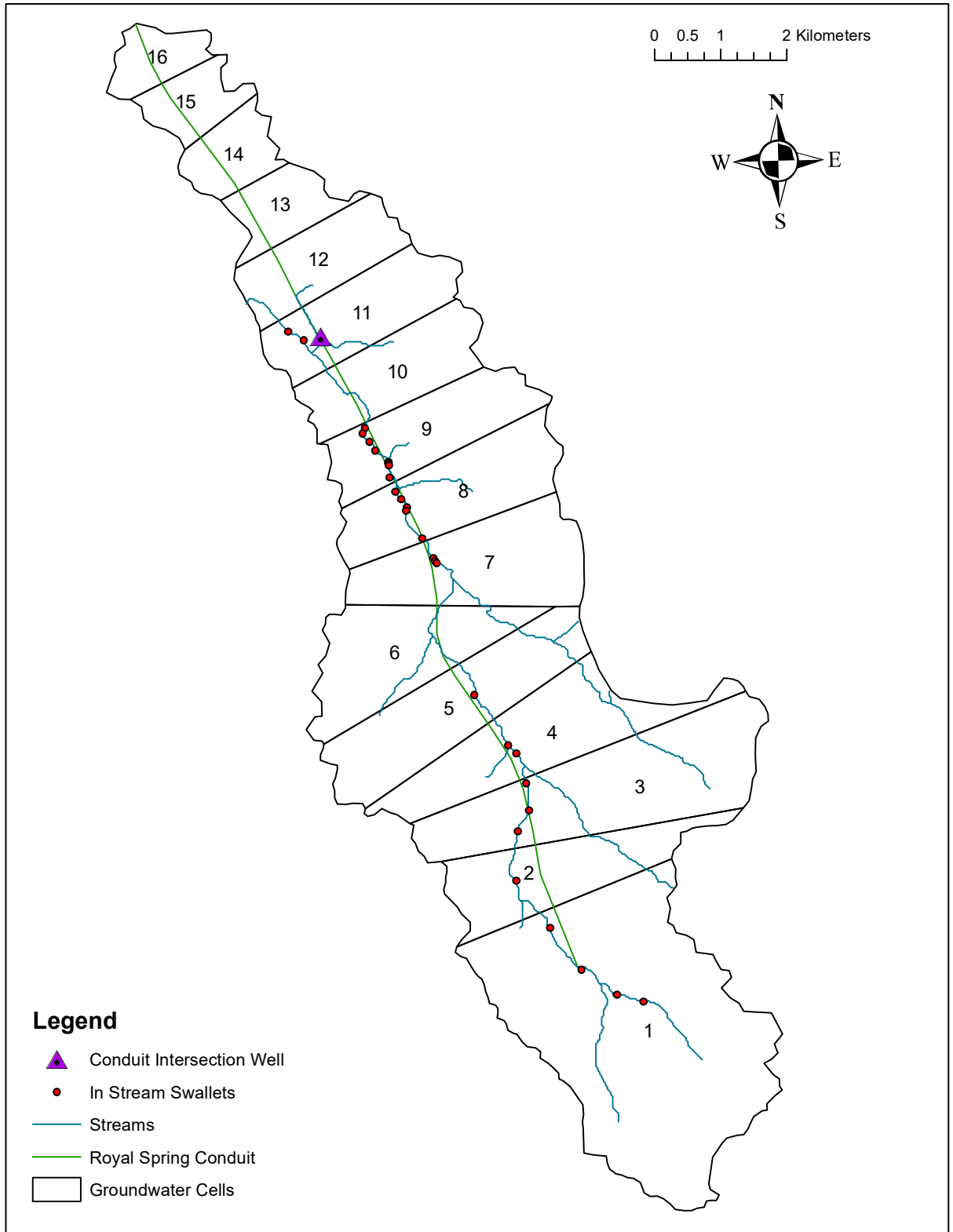


Figure 4. Groundwater Cells

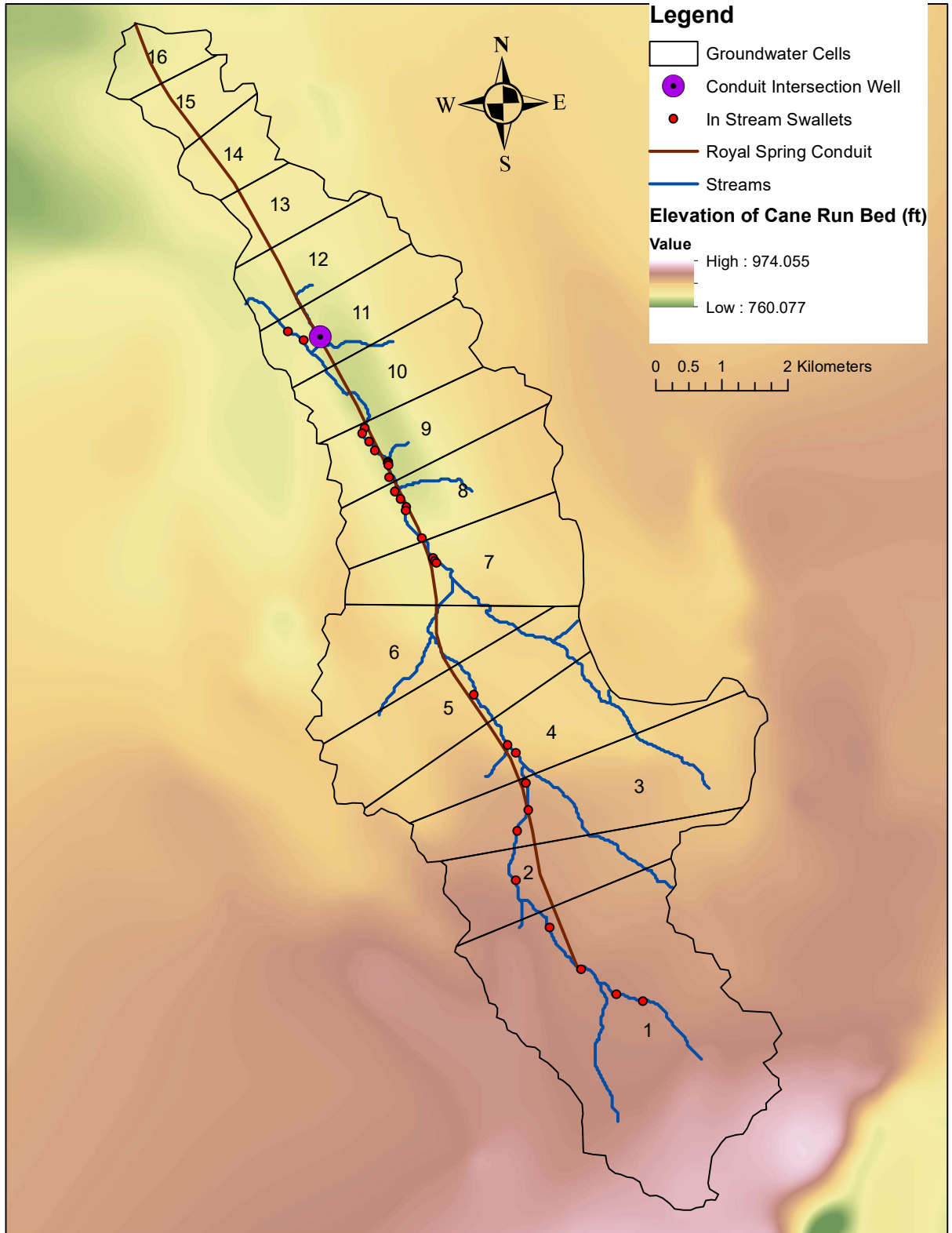


Figure 5. Cane Run Bed Elevations

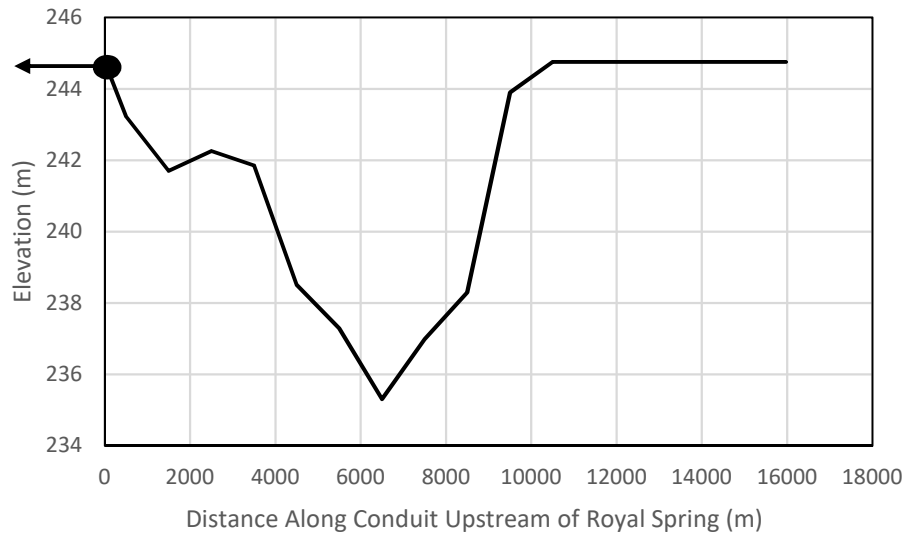


Figure 6. Hypothesized Conduit Profile

KYHP KWIS Wells in Field 53

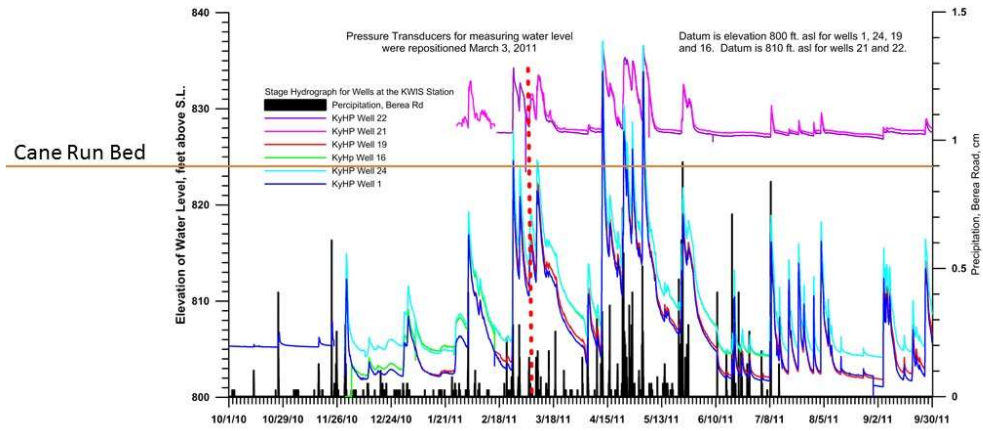


James C. Currens photograph, 2012

UK
UNIVERSITY OF
KENTUCKY
Kentucky Geological Survey

Figure 7. KWIS Well Locations

Stage changes in the wells that constitute the KWIS



Adapted from Jim Currens

2010-11 Water Year



Figure 8. KWIS Stage Recordings

Chapter 4 Methods

4.1) Model Formulation Overview

A combined discrete-continuum (CDC) hybrid approach for simulating the surface and subsurface hydrology and hydraulics was formulated. This formulation utilized a multiple-layer continuum approach for the hydrology of surface runoff, soil, epikarst, fractures, and unsaturated and saturated matrix flow. We used a semi-lumped approach for the continuum components by dividing the surface and subsurface domains into sub-basins that were consistent with spatial variation in hydrologic and geologic characteristics across the study site. Our surface runoff, surface routing, and soil water modelling was performed using the Soil Water Assessment Tool, or SWAT, which in turn accounts for seasonality of vegetation across the study site. Our groundwater continuum components explicitly represent a fracture network, vadose zone (unsaturated) flow, an epikarst zone, and perched aquifers, and this coupling in a CDC model has rarely, to our knowledge, been performed in previous work. We used discrete components for modelling the hydraulics of the surface stream, primary conduit and vertical shafts connecting the two. A one-dimensional, unsteady, kinematic approximation was used for the stream, and the conduit network was represented as a pipe network. As will be discussed below, conservation laws or their semi-empirical derivatives were used for modelling inter- and intra-transport for each geomorphologic component.

Surface and soil hydrology modelling included calculating infiltration (Q_{inf}), runoff (Q_{sur}), evapotranspiration (ET), percolation (Q_{perc}), lateral soil flow (Q_{lat}), and tributary flow (Q_{trib}). The surface hydrology modelling follows exactly from the method of Neistch

et al. (2011) because the SWAT model was used to calculate these components. In brief, SWAT uses the Green-Ampt Mein-Larson method to estimate surface runoff and infiltration volumes (Mein and Larson 1973). The Green-Ampt method assumes that there is always excess water at the surface, the soil profile is homogeneous, moisture content in the soil is evenly distributed, and a sharp wetting front exists in the soil profile (Green and Ampt, 1911; Neitsch et al., 2011). Precipitation volume that exceeds the infiltration volume will contribute to surface runoff. SWAT estimates the time of concentration, including the overland flow and tributary components, using Manning's like approach. The method used to calculate the total surface runoff that reached the stream or tributary at a sub-watershed outlet (Q_{Runoff}). SWAT uses the Penman-Monteith method (Monteith, 1965) to calculate potential evapotranspiration (PET). Actual evapotranspiration (ET) is calculated using an approach similar one used by Richey (1972) and later adapted by the SWAT model (Neitsch et al., 2011), where the actual transpiration is a function of the leaf area index and actual soil evapotranspiration is a function of the soil water content. SWAT models soil water via mass balance for two soil layers, and the model calculates a field capacity for each layer as the difference in available water content and the wilting capacity for the specific soil. SWAT models soil percolation via a storage routing method. Percolation occurs when the field capacity of the soil exceeds the storage volume of the layer, and the rate depends on the saturated hydraulic conductivity of the soil layer. (Neitsch et al., 2011) SWAT simulates lateral flow using a kinematic approximation of a mass continuity equation developed by Sloan et al. (1983). The total lateral flow in the sub-watershed (Q_{lat}) will depend on sub-watershed properties such as the slope lengths and angles, soil properties such as the saturated hydraulic conductivity, and the soil water

content that exceeds the soil's field capacity. Tributaries transfer runoff directly from a sub-watershed to the trunk stream or traverse several sub-watersheds to the trunk stream. The latter requires routing, and SWAT routes tributary flow through each reach using a variable storage routing method (Williams, 1969; Williams and Hann, 1973; Arnold et al., 1995), the Muskingum routing method, and Manning's equation to calculate flowrates and velocities.

Output from the surface modelling is input to the coupled stream and groundwater model, after some manipulation. The tributary flow (Q_{trib}), surface runoff portion that flows to the stream (xQ_{sur}), and lateral soil flow portions that flow to the stream (xQ_{lat}) are inputs to the streamflow component. Percolation from the bottom soil layer (Q_{perc}) are input to the epikarst layer of the groundwater model. The portion of the surface runoff ($(1-x)Q_{sur}$), and lateral soil flow ($((1-x)Q_{lat})$) draining to sinkholes serve as input to the sinkholes across the landscape (Q_{sink}), as part of the groundwater model. For each sub-basin of the surface model, we used an area-weighted approach as a function of sinkhole drainage area to separate surface runoff and lateral flow that is delivered to surface streams and tributaries versus that delivered to sinkholes, which is analogous to the work of others (e.g., Baffaut and Benson, 2009; Malago et al., 2016).

The numerical model simulates streamflow (Q_{stream}) using a one-dimensional, unsteady water storage routing and accounts for water loss, or gains, to fluviokarst swallets ($Q_{swall-in}$) located in the stream corridor. The streamflow model used the Jones' Formula to account for non-uniformity in the model (Chow, 1959; Jain, 2001). Swallets may pirate a portion, or all of the flow in a stream reach, and may possibly act as estuvelles when adverse hydraulic gradients exist. The model represented the swallets as constant-diameter

cylindrical segments connected to the surface stream reach and groundwater conduit nodes. We formulated swallet flow by applying the unsteady conservation of mass to storage associated with the geometry of the swallets (e.g., Munson et al., 2013). The numerical model explicitly solved flow through the swallets using the Darcy-Weisbach approach, similarly to turbulent conduit flow (Jeannin, 2001; Shoemaker, 2008). The formulation considers two conditions for stream to swallet linkage. We used a weir equation (e.g., Gupta, 2008) for $Q_{swall-in}$ for the condition when the swallet is filling. We solved the groundwater conduit model using the stream's free surface elevation to estimate $Q_{swall-in}$ for the condition when the swallet is full.

The model formulates the epikarst as a storage and routing zone with multiple transfers possible. The formulation accounts for percolation of epikarst water to vadose rock zone (Q_{ep-v}) and connectivity of the epikarst to the fractures (Q_{ep-f}). An activation threshold height in the epikarst is used to trigger fracture flow during seasonally wet conditions and hydrologic events, consistent with the work of Tritz et al. (2011). The model solves the conservation of mass equation for the epikarst to find the volume and height of water stored in the epikarst. Q_{ep-v} is calculated in the vadose zone model. Water is routed to the fracture network when the epikarst activation threshold is exceeded. During very wet conditions, the fracture network may fill with water, the epikarst storage may reach capacity, and therefore epikarst overflow occurs and water is routed to the surface stream (Q_{over}).

The model simulates the vadose rock matrix as a variably saturated granular rock mass, where percolated epikarst water will be transported to a perched aquifer or the saturated rock matrix. Also, the model assumes that the effect of fractures and void

volumes on unsaturated flow are negligible given that fracture flow is also accounted for. The formulation solves the Richard's Equation for unsaturated flow in the vadose zone similarly to models specifically for vadose zone processes (Niswonger et al. 2006; Simunek et al. 1998). The numerical model assumes that flow is gravity driven so that the diffusive term can be removed (Niswonger et al., 2006). The hydraulic conductivity is calculated using the Brooks-Corey function. The number of the vadose layers is found so that the CFL condition will not be violated, and the spatial discretization is equal to the thickness of each vadose layer. The velocity used for the unsaturated flow is that of the trailing wave, which is generally faster than the leading wave (Niswonger et al., 2006).

The model represents the fracture network as thin plate-like void spaces in the rock matrix that can store water and provide a pathway directly to the conduit. The fracture network exchanges water with the sinkholes, epikarst, perched aquifers, the saturated matrix and conduit. The formulation assumed flow to the vadose section of the fracture network will occur quickly, within the temporal step of the model, to the saturated water volume. An equivalent porous medium approach is used, where the geometry of the fracture network is represented by a set of parameters that are uniform across each sub-basin (Snow, 1969; Kresic, 2010). The numerical model explicitly solves the conservation of mass for the fracture network in each groundwater cell as a function of fracture density and fracture aperture, as well as the conservation of momentum. The model assumes that fractures have continuous width equal to the extent of the spatial distraction of a groundwater cell, therefore the representative fracture density encapsulates the physical fracture density of the network and the average width of fractures in the network. The

conservation of momentum is applied in the form of the Cubic Law, similarly as others (Snow, 1969; Long et al., 1985; Bear et al., 1993; Zimmerman and Yeo, 2000).

The model formulation considers the potential for perched water tables in groundwater sub-basins due to the presence of an aquitard. The numerical model explicitly applies the conservation of mass principle to the variable-volume perched aquifer. The explicit linking of the perched aquifer with fracture flow considered herein is consistent with source/sink terms in other fracture network formulation (Snow, 1969; Zimmerman and Yao, 2000). Two types of flux are considered. The model computes Darcian flow exchange between the perched aquifer and the fracture network. The model assumes that the exchange flow between the perched aquifer and the fracture network is typically Darcian. In the case, the flowpath distance and the area the flow exchange between the perched aquifer and the fracture network is computed using the fracture network geometry. The model also considers non-Darcian transfer to the fracture network when an activation height is reached. This condition reflects the perched aquifer reaching horizontal fractures, such as along a bedding plane, that are well-connected to the bulk fracture network.

The formulation represents the saturated rock matrix as a saturated variable-volume water storage reservoir in a porous medium with a lower permeability than the fracture network and the conduit network (White, 1999; Hartmann et al., 2013). The numerical model explicitly applies the unsteady conservation of mass principle to the storage zone, in a similar manner to how other authors model a saturated matrix storage reservoir for karst aquifers (Husic et al., 2017b). The model also uses Darcy's Law to compute the flow between the saturated matrix and the conduit and cave network, in a similar manner to other karst models (Rooji et al., 2013, Reimann et al., 2013).

The model represents conduits as subterranean pipes that dominate sub-surface flow because of the fast-turbulent conditions. Additionally, phreatic and epi-phreatic conduits can interact and exchange flow with swallets, the fracture network, and the saturated rock matrix, and convey water to a spring. The numerical model represents a conduit network as a set of pipe sections that intersect at nodes. The numerical model uses the Darcy-Weisbach equation and the conservation of mass principle to calculate the conduit flowrates, similarly to others (Jeannin, 2001; Shoemaker et al., 2008; Rooji et al., 2013; Chen and Goldscheider, 2014).

The numerical model calculates springflow by a simultaneous solution of the flowrate and mass balance equations for the conduit, swallets, fracture network, and saturated matrix at every groundwater cell. The simultaneous solution requires a boundary condition at the spring. This boundary condition is the elevation of surface water at the spring. This condition eliminates a pressure head term in the Darcy-Weisbach equation for the final conduit segment because the surface water at the spring has a free surface.

4.2) Model Equations

4.2.1) Surface and Soil Hydrology Equations

Surface and soil hydrology modelling included calculating infiltration (Q_{inf}), runoff (Q_{sur}), evapotranspiration (ET), percolation (Q_{perc}), lateral soil flow (Q_{lat}), and tributary flow (Q_{trib}). The surface hydrology modelling follows exactly from the method of Neistch et al. (2011) because the SWAT model was used to calculate these components.

The numerical model utilizes the Green-Ampt Mein-Larson method to determine surface runoff and infiltration volumes (Mein and Larson 1973). The equations used to calculate the infiltration rate and volumes are published in Neitsch et al. (2011) and are

$$f_{inf,t} = K_e \left(1 + \frac{\Psi_{wf} \cdot \Delta\theta_v}{F_{inf,t}} \right) \quad (1)$$

$$F_{inf,t} = F_{inf,t-1} + R_{\Delta t} \quad (2)$$

$$K_e = \frac{56.82 \cdot K_{sat}^{0.286}}{1 + 0.051 e^{0.062 \cdot CN}} - 2 \quad (3)$$

$$\Delta\theta_v = \left(1 + \frac{SW}{FC} \right) (0.95 \phi_{soil}) \quad (4)$$

where $f_{inf,t}$ is the infiltration rate at time t (mm/hr), K_e is the effective hydraulic conductivity (mm/hr), Ψ_{wf} is the wetting front matric potential (mm), $\Delta\theta_v$ is the change in volumetric moisture content across the wetting front (mm/mm), $F_{inf,t}$ is the cumulative infiltration at time t (mm), $F_{inf,t-1}$ is the cumulative infiltration for the previous time step, $R_{\Delta t}$ is the amount of rain falling during the time step (mm), K_{sat} is the saturated hydraulic conductivity (mm/hr), CN is the curve number, SW is the soil water content of the entire profile (mm), FC is the amount of water in the soil profile at field capacity (mm) and ϕ_{soil} is the porosity of the soil (mm/mm).

Precipitation volume that exceeds the infiltration volume becomes surface runoff. SWAT estimates the time of concentration, including the overland flow and tributary components, using a Manning's like approach. The method used to calculate the total surface runoff that reached the stream or tributary at a sub-watershed outlet (Q_{Runoff}) is summarized by equation 2:1.4.1 and figure 2:1-3 in Neitsch et al. (2011) as

$$Q_{surf} = (Q'_{surf} + Q_{stor,i-1}) \left(1 - \exp \left[\frac{-surlag}{t_{conc}} \right] \right) \quad (5)$$

where Q_{surf} is the amount of surface runoff discharged to the main channel on a given day (mm), Q'_{surf} is the amount of surface runoff generated in the subbasin on a given day (mm), $Q_{stor,i-1}$ is the total surface runoff stored or lagged from the previous day (mm), $surlag$ is the surface runoff lag coefficient, and t_{conc} is the time of concentration for the subbasin (hrs).

The time of concentration will include an overland flow component and a channelized component, because every sub-watershed will either have a tributary stem or a stream within it. Manning's equation is utilized to calculate both the overland flow component and the channel flow component of the total time of concentration. The method the numerical model uses to calculate the time of concentration follows the method used in the SWAT model and are summarized by equations 2:1.3.2 through 2:1.3.14 in Neitsch et al. (2011) as

$$t_{conc} = t_{ov} + t_{ch} \quad (6)$$

$$t_{ov} = \frac{L_{slp}^{0.6} \cdot n_{ov}^{0.6}}{18 \cdot slp^{0.3}} \quad (7)$$

$$t_{ch} = \frac{0.62 \cdot L \cdot n_{ch}^{0.75}}{Area^{0.125} \cdot slp_{ch}^{0.375}} \quad (8)$$

where t_{conc} is the time of concentration for a subbasin (hr), t_{ov} is the time of concentration for overland flow (hr), t_{ch} is the time of concentration for channel flow, L_{slp} is the subbasin slope length (m), n_{ov} is Manning's roughness coefficient for overland flow for the subbasin, n_{ch} is Manning's roughness coefficient for the channel, slp is the average slope

in the subbasin (m/m), L is the channel length from the most distant point to the subbasin outlet (km), slp_{ch} is the channel slope (m/m), and $Area$ is the subbasin area.

SWAT uses the Penman-Monteith method (Monteith, 1965) to calculate potential evapotranspiration (PET), and actual evapotranspiration (ET) is calculated using an approach similar one used by Richey (1972) and later adapted by the SWAT model (Neitsch et al., 2011). The Penman-Monteith method utilizes solar radiation, air temperature, relative humidity, and wind speed data to calculate the energy needed to evaporate and remove the water vapor, and is summarized by equations following from Neitsch et al. (2011) as

$$\lambda E = \frac{\Delta \cdot (H_{net} - G) + \rho_{air} \cdot c_p \cdot [e_z^0 - e_z] / r_a}{\Delta + \gamma_p \left(1 + \frac{r_c}{r_a}\right)} \quad (9)$$

where λ is the latent heat flux density ($\text{MJ m}^{-2} \text{d}^{-1}$), E is the depth rate evaporation (mm/d), Δ is the slope of the saturation vapor pressure-temperature curve, de/dT ($\text{kPa } ^\circ\text{C}^{-1}$), H_{net} is the net radiation ($\text{MJ m}^{-2} \text{d}^{-1}$), G is the heat flux density to the ground ($\text{MJ m}^{-2} \text{d}^{-1}$), ρ_{air} is the air density (kg/m^3), c_p is the specific heat at constant pressure ($\text{MJ kg}^{-1} \text{ } ^\circ\text{C}^{-1}$), e_z^0 is the saturation vapor pressure of air at height z (kPa), e_z is the water vapor pressure of air at height z (kPa), γ_p is the psychrometric constant ($\text{kPa } ^\circ\text{C}^{-1}$), r_c is the plant canopy resistance (s/m), and r_a is the diffusion resistance of the air layer (s/m). The method used to calculate actual evapotranspiration follows from Neitsch et al. (2011) as

$$E_s = E_0' \cdot cov_{sol} \quad (10)$$

$$cov_{sol} = \exp(-5 \times 10^{-5} \cdot CV) \quad (11)$$

$$E_s'' = \min \left[E_s, \frac{E_s \cdot E_0'}{E_s + E_t} \right] \quad (12)$$

$$E_{soil,ly} = E_{soil,zl} - E_{soil,zu} \cdot esco \quad (13)$$

$$E_{soil,z} = E_s'' \frac{z}{z + \exp(2.374 - 0.00713z)} \quad (14)$$

$$E'_{soil,ly} = E_{soil,ly} \cdot \exp \left(\frac{2.5(SW_{ly} - FC_{ly})}{FC_{ly} - WP_{ly}} \right) \text{ for } SW_{ly} < FC_{ly} \quad (15)$$

$$E'_{soil,ly} = E_{soil,ly} \text{ for } SW_{ly} \geq FC_{ly} \quad (16)$$

$$E''_{soil,ly} = \min \left(E'_{soil,ly}, 0.8(SW_{ly} - WP_{ly}) \right) \quad (17)$$

where E_s is the maximum soil evaporation on a given day (mm), E_0' is the potential evapotranspiration (mm), cov_{so} is the soil cover index, CV is the aboveground biomass and residue (kg/ha), $E_{soil,ly}$ is the evaporative demand for given soil layer (mm), $E_{soil,zl}$ is the evaporative demand at the bottom of the soil layer (mm), $E_{soil,zu}$ is the evaporative demand at the top of the soil layer (mm), $esco$ is the soil evaporation compensation coefficient, $E_{soil,z}$ is the evaporative demand at depth z (mm), E_t is the maximum transpiration on a given day (mm), E_s'' is the maximum soil water evaporation on a given day adjusted for plant water use (mm), z is the depth below the surface, $E'_{soil,ly}$ is the evaporative demand for a given soil layer adjusted for water content (mm), SW_{ly} is the soil water content for the layer (mm), FC_{ly} is the water content of the layer at field capacity (mm), WP_{ly} is the water content of the layer at the wilting point (mm), and $E''_{soil,ly}$ is the actual amount of water removed from the layer by evaporation (mm),

SWAT accounts soil water via mass balance for two soil layers, and the model calculates a field capacity for each layer as the difference in available water content and the wilting capacity for the specific soil. SWAT models soil percolation via a storage routing method. Percolation occurs when the field capacity of the soil exceeds the storage volume of the layer, and the rate depends on the saturated hydraulic conductivity of the soil layer (Neitsch et al., 2011). The equations used to calculate the field capacity of the soil are published as equations 2:3.1.1 through 2:3.1.6 in Neitsch et al. (2011) as

$$FC_{ly} = WP_{ly} + AWC_{ly} \quad (18)$$

$$WP_{ly} = 0.4 \cdot \frac{m_c \cdot \rho_b}{100} \quad (19)$$

where FC_{ly} is the water content at field capacity as a fraction of the total soil volume, WP_{ly} is the water content at wilting point as a fraction of the total soil volume, AWC_{ly} is the available water capacity of the soil layer as a fraction of the total soil volume, m_c is the percent clay of a soil layer (%), and ρ_b is the bulk density for the soil layer (Mg/m^3). The percolation out of the bottom soil layer is summarized by equations 2:3.2.1 through 2:3.2.4 in Neitsch et al. (2011) as

$$w_{perc,ly} = SW_{ly,excess} \cdot \left(1 - \exp \left[\frac{-\Delta}{TT_{perc}} \right] \right) \quad (20)$$

$$SW_{ly,excess} = SW_{ly} - FC_{ly}, \text{ if } SW_{ly} > FC_{ly} \quad (21)$$

$$SW_{ly,excess} = 0, SW_{ly} \leq FC_{ly} \quad (22)$$

$$TT_{perc} = \frac{SA_{ly} - FC_{ly}}{K_{sat}} \quad (23)$$

where $w_{perc,ly}$ is the amount of water percolating to the underlying soil layer (mm), $SW_{ly,excess}$ is the drainable volume of water in the soil layer on a given day (mm), Δt is the length of the time step (hrs), TT_{perc} is the travel time for percolation (hrs), SW_{ly} is the water content in the soil layer (mm), FC_{ly} is the water content of the soil layer at field capacity (mm), SAT_{ly} is the amount of water in the soil layer when completely saturated (mm), and K_{sat} is the saturated hydraulic conductivity for the layer (mm/hr).

SWAT simulates lateral flow using a kinematic approximation of a mass continuity equation developed by Sloan et al. (1983). The total lateral flow in the sub-watershed (Q_{lat}) will depend on sub-watershed properties such as the slope lengths and angles, soil properties such as the saturated hydraulic conductivity, and the soil water content that exceeds the soil's field capacity. The method is summarized by equations 2:3.5.1 through 2:3.5.9 and figures 2:3-3 and 2:3-4 in Neitsch et al. (2011) as

$$Q_{lat} = 0.024 \cdot \left(\frac{2 \cdot SW_{ly,excess} \cdot K_{sat} \cdot slp}{\phi_d \cdot L_{hill}} \right) \quad (24)$$

$$Q_{lat} = (Q'_{lat} + Q_{latstor,i-1}) \left(1 - \exp \left[-\frac{1}{TT_{lag}} \right] \right) \quad (25)$$

$$TT_{lag} = 10.4 \frac{L_{hill}}{K_{sat,max}} \quad (26)$$

where Q_{lat} is the water discharged from the hillslope outlet (mm/d), L_{hill} is the hillslope length (m), ϕ_d is the drainable porosity of the soil (mm/mm), K_{sat} is the saturated hydraulic conductivity (mm/hr), slp is the slope, Q'_{lat} is the amount of lateral flow generated in a given day (mm), $Q_{latstor,i-1}$ is the lateral flow stored or lagged from the previous day

(mm), TT_{lag} is the lateral flow travel time (days), and $K_{sat,max}$ is the highest layer saturated hydraulic conductivity in the soil profile (mm/hr).

Tributaries transfer runoff directly to the trunk stream or traverse several sub-watersheds to the trunk stream. The latter requires routing, and SWAT routes tributary flow through each reach using a variable storage routing method (Williams, 1969; Williams and Hann, 1973; Arnold et al., 1995), the Muskingum routing method, and Manning's equation to calculate flowrates and velocities. This method follows the methods used by the SWAT model and is summarized by equations 7:1.1.1 through 7:1.4.12 and figures 7:1-1 through 7:1-3 in Neitsch et al. (2011) as

$$q_{ch} = \frac{1}{n} A_{ch} R_{ch}^{\frac{2}{3}} slp_{ch}^{\frac{1}{2}} \quad (27)$$

$$V_{out,2} = SC(V_{in} + V_{stored,1}) \quad (28)$$

$$V_{out,2} = C_1 V_{in,2} + C_2 V_{in,1} + C_3 V_{out,1} \quad (29)$$

$$C_1 = \frac{\Delta t - 2KX}{2K(1-X) + \Delta t} \quad (30)$$

$$C_2 = \frac{\Delta t + 2KX}{2K(1-X) + \Delta t} \quad (31)$$

$$C_3 = \frac{2K(1-X) - \Delta t}{2K(1-X) + \Delta t} \quad (32)$$

$$C_1 + C_2 + C_3 = 1 \quad (33)$$

where q_{ch} is the channel flowrate (m^3/s), A_{ch} is the channel cross-sectional area (m^2), R_{ch} is the channel hydraulic radius (m), slp_{ch} is the channel slope (m/m), n is Manning's roughness coefficient, $V_{out,2}$ is the volume of outflow at the end of a time-step (m^3), SC is

the storage coefficient, V_{in} is the volume of inflow during the timestep (m^3), $V_{stored,1}$ is the storage volume at the beginning of the timestep (m^3), K is the storage time constant (s), X is a weighting factor, $V_{in,2}$ is the volume of inflow from the previous reach at the end of the time-step (m^3), $V_{in,1}$ is the volume of inflow from the previous reach at the beginning of the time-step (m^3), $V_{out,1}$ is the volume of outflow at the beginning of a time-step (m^3), and Δt is the length of a timestep (s).

4.2.2) Inputs for the Groundwater Model across the Land Surface

Output from the surface modelling is input to the coupled stream and groundwater model, after adjusting for differences in spatial discretization. The tributary flow (Q_{trib}), surface runoff portion that flows to the stream (xQ_{sur}), and lateral soil flow portions that flow to the stream (xQ_{lat}) are inputs to the streamflow component. Percolation from the bottom soil layer (Q_{perc}) are input to the epikarst layer of the groundwater model. The portion of the surface runoff ($(1-x)Q_{sur}$), and lateral soil flow ($(1-x)Q_{lat}$) draining to sinkholes serve as input to the sinkholes across the landscape (Q_{sink}), as part of the groundwater model.

For each sub-basin of the surface model, we used an area-weighted approach as a function of sinkhole drainage area to separate surface runoff and lateral flow that is delivered to surface streams and tributaries versus that delivered to sinkholes, which is analogous to the work of others (e.g., Baffaut and Benson, 2009; Malago et al., 2016). The total flow into the sinkholes in a groundwater cell is expressed as:

$$Q_{sink} = \sum_{A_{ws \cap cell}} \left((Q_{Runoff} + Q_{Lateral}) \frac{A_{sink \cap ws \cap cell}}{A_{ws}} \right) \quad (34)$$

where Q_{sink} is the total volumetric sinkhole flowrate entering the fracture network of a groundwater cell (m^3/s), Q_{Runoff} is the total surface runoff in a sub-watershed (m^3/s), $Q_{Lateral}$ is the total lateral flow in a sub-watershed (m^3/s), $A_{sink \cap ws \cap cell}$ is the area of sinkhole drainage within an intersecting groundwater cell and sub-watershed (m^2), A_{ws} is the area of a sub-watershed (m^2), and $A_{ws \cap cell}$ is an area of intersecting groundwater cell and sub-watershed (m^2).

The surface runoff and lateral flow delivered to the streams and tributaries at the outlet of the sub-watershed is the remainder of the total surface runoff and lateral flow in the sub-watershed that does not drain to sinkholes and is expressed as:

$$Q_{sur} = Q_{Runoff} \frac{A_{ws} - A_{sink}}{A_{ws}} \quad (35)$$

$$Q_{lat} = Q_{Lateral} \frac{A_{ws} - A_{sink}}{A_{ws}} \quad (36)$$

where Q_{sur} is the surface runoff delivered to the stream reach(s) or tributary in the sub-watershed (m^3/s), Q_{lat} is the lateral flow delivered to the stream or tributary in the sub-watershed (m^3/s), and A_{sink} is the area of sinkhole drainage area within the sub-watershed (m^2).

4.2.3) Surface Streamflow

The numerical model simulates streamflow (Q_{stream}) using a one-dimensional, unsteady water storage routing and accounts for water loss, or gains, to fluviokarst swallets ($Q_{swall-in}$) located in the stream corridor. The streamflow model used Manning's Equation to calculate streamflow the Jones' Formula to account for non-uniformity in the model (Chow, 1959; Jain, 2001).

The numerical model simulates streamflow using a one-dimensional, unsteady water storage routing method for an incompressible fluid adapted (Munson et al., 2013) as

$$\frac{\partial V}{\partial t} - \oiint \vec{v} \cdot \hat{n} dA = 0 \quad (38)$$

where V is volume (m^3), t is time (s), dA is the differential control surface area, \vec{v} is the fluid velocity vector (m/s), and \hat{n} is a unit vector normal to the control surface.

A numerical approximation and temporal discretization of the routing equation for a reach yields:

$$V_{i+\frac{1}{2}}^j = V_{i-\frac{1}{2}}^j + Q_{up,i}^j \Delta t + S - \left[k_s Q_{dn,i-\frac{1}{2}}^j + (1 - k_s) Q_{dn,i+\frac{1}{2}}^j \right] \Delta t \quad (39)$$

$$Q_{up,i}^j = k_s Q_{dn,i-\frac{1}{2}}^{j-1} + (1 - k_s) Q_{dn,i+\frac{1}{2}}^{j-1} \quad (40)$$

where V is the volume water in a stream reach (m^3), Q_{up} is the flowrate into a stream reach from an upstream reach (m^3/s), Q_{dn} is the flowrate out of a stream reach into a downstream reach (m^3/s), k_s is a flood-wave coefficient, Δt is the temporal discretization step of the model (s), the j superscript represents the current stream reach, the $j + 1$ superscript represents the preceding stream reach, the i subscript represents the current model

temporal step, the $i - \frac{1}{2}$ superscript represents the beginning of the current temporal step, and the $i + \frac{1}{2}$ superscript represents the end of the current temporal step. The source/sink term (S) may include any of the following terms that are applicable:

$$S = Q_{sur} + Q_{trib} + Q_{lat} - Q_{in} \quad (41)$$

where Q_{in} is the flowrate from a stream reach into a swallet (m^3/s).

The numerical model requires an additional equation to solve both unknowns in the discretized routing equation, i.e., $(Q_{dn,i+\frac{1}{2}}^j)$ and $(V_{i+\frac{1}{2}}^j)$. The equation will be of the form:

$$Q_{dn,i+\frac{1}{2}}^j = f(V_{i+\frac{1}{2}}^j), \text{ or} \quad (42)$$

$$Q_{dn,i+\frac{1}{2}}^j = f(H_{i+\frac{1}{2}}^j) \quad (43)$$

given knowledge of the stream geometry:

$$V = L_{reach}A(H) \quad (44)$$

where H is the height of water in a stream reach (m), L_{reach} is the length of a stream reach (m), and $A(H)$ is the cross-sectional area of a stream reach as a function of height (m^2).

In streams where the assumption of quasi-uniform flow is valid, the numerical model will use Manning's Equation as the function required to solve for the unknowns in the discretized routing equation as:

$$Q_{dn} = \frac{1}{n} R^{\frac{2}{3}} A S_0^{\frac{1}{2}} \quad (45)$$

where n is Manning's channel roughness coefficient ($m^{1/6}$), A is the cross-sectional area of the stream reach (m^2), R is the hydraulic radius of the stream reach cross-section (m), and S_0 is the bed slope of the stream reach.

In streams where the assumption of quasi-uniform flow is invalid, a different form of the Manning's functional dependence of the unknowns in the discretized routing equation will be required. The Jones' Formula is commonly used to approximate stage discharge relationships in streams where uniform flow assumptions are invalid (Chow, 1959; Jain, 2001), and the Jones' Formula is shown below as

$$\frac{Q}{Q_r} = \sqrt{\frac{1}{cS} \frac{\partial h_{stream}}{\partial t}} \quad (46)$$

$$c = \frac{dQ}{dA} = \frac{5k}{3n} R^{\frac{2}{3}} S^{\frac{1}{2}} \quad (47)$$

where Q_{dn} is the downstream flow (m^3/s), Q_r is the downstream flowrate per Manning's Equation (m^3/s), c is the flood-wave celerity (m/s), S is the channel slope (m/m), h_{stream} is the height of water in the channel (m), t is time (s), A is the cross-section area of the stream reach (m^2), k is 1 for SI units, n is Manning's roughness coefficient ($m^{1/6}$), and R is the hydraulic radius of the stream reach (m).

4.2.4) Swallets

Swallets within the stream corridor may pirate a portion, or all of the flow in a stream reach, and may possibly act as esteveselles when adverse gradients exist. The model represented the swallets as constant-diameter cylindrical segments connected to the surface

stream reach and groundwater conduit nodes. We formulated swallet flow by applying the unsteady conservation of mass to storage associated with the geometry of the swallets (e.g., Munson et al., 2012). The numerical model explicitly solved flow through the swallets using the Darcy-Weisbach approach, similarly to turbulent conduit flow (Jeannin, 2001; Shoemaker, 2008). The formulation considers two conditions for stream to swallet linkage. We used a weir equation (e.g., Gupta, 2008) for $Q_{swallet-in}$ for the condition when the swallet is filling. We solved the groundwater conduit model using the stream's free surface elevation to estimate $Q_{swallet-in}$ for the condition when the swallet is full.

Geometry considers the length and volume of the swallets. The length of each swallet segment is given as

$$L_{swallet} = \tau_{swallet}(H_{swallet} + X_{stream}) \quad (48)$$

where $L_{swallet}$ is the length of the swallet segment (m), $\tau_{swallet}$ is the tortuosity of the swallet, X_{stream} is the horizontal distance between the conduit node and the stream reach the swallet is located (m), and $H_{swallet}$ is the elevation difference between the creek and conduit (m). The volume of water in a swallet is given by:

$$V_{swallet} = h_{swallet} \left(\frac{L_{swallet}}{H_{swallet}} \right) \frac{\pi D^2}{4} = h_{swallet} \left(\frac{L_{swallet}}{H_{swallet}} \right) A_{swallet} \quad (49)$$

where $V_{swallet}$ is the volume of water in a swallet (m³), $h_{swallet}$ is the height of water in a swallet relative to the conduit node (m), $A_{swallet}$ is the cross-sectional area of the swallet (m²), and D is the diameter of a swallet.

Individual swallets that connect the same groundwater cell and creek reach are combined as a representative swallet with an equivalent hydraulic diameter to the former

individual swallets. The model uses the Darcy-Weisbach head loss equation and the conservation of mass principle to solve for the flow velocity in the swallet and the volume of stored water in the swallet. The conservation of mass equation for an incompressible, unsteady, variable storage volume is (Munson, 2013):

$$\frac{\partial V}{\partial t} - \oiint \vec{v} \cdot \hat{n} dA = 0 \quad (50)$$

$$Q_{net} = \oiint \vec{v} \cdot \hat{n} dA \quad (51)$$

where V is volume (m^3), t is time (s), dA is the differential control surface area, \vec{v} is the fluid velocity vector (m/s), \hat{n} is a unit vector normal to the control surface, and Q_{net} is the net flowrate in/out of the control volume.

The model considers two conditions which can vary the form of the Darcy-Weisbach and conservation of mass equations. The first condition is when the swallet is full and the free surface is the surface stream's free-surface. The second condition is when the swallet is not full and the free surface is within the vertical column in the subsurface. For the first condition, the conservation of mass equation becomes:

$$Q_{in} = v_{swallet} A_{swallet} \quad (52)$$

where Q_{in} is the flowrate from the creek into the swallet (m^3/s), and $v_{swallet}$ is the velocity through the swallet. The Darcy-Weisbach head-loss equation becomes:

$$h_{stream} + H_{swallet} - \frac{P_c}{\gamma} = \left(1 + f \frac{L_{swallet}}{D}\right) \frac{v_{swallet}^2}{2g} \text{ for } v_{swallet} > 0 \quad (53)$$

$$h_{stream} + H_{swallet} - \frac{P_c}{\gamma} = \left(1 - f \frac{L_{swallet}}{D}\right) \frac{v_{swallet}^2}{2g} \text{ for } v_{swallet} < 0 \quad (54)$$

where h_{stream} is the height of water in the stream reach (m), P_c is the pressure in the conduit (kPa), γ is the specific weight of water (9.8 kN/m³), f is the Darcy-Weisbach friction factor, D is the diameter of the swallet (m), g is gravitational acceleration (9.8 m/s²), and $v_{swallet}$ is the velocity through the swallet (m/s).

Positive swallet velocities represent flow conditions where the water is flowing from the creek into the swallet and into the conduit. Negative swallet velocities represent conditions when flow is in the direction opposite of gravity and when the swallet is full, it acts as a spring to the creek.

While the swallet is full, the stream model considers the flowrate through the swallet and into the conduit from the previous timestep equal to the flowrate from the stream into the swallet in the current timestep:

$$Q_{in}^i = v_{swallet}^{i-1} A_{swallet} \text{ for } h_{swallet} = H_{swallet} \quad (55)$$

where the i and $i-1$ superscripts represent current and previous timesteps.

For the second condition, when the swallet is not full or connected to the creek, the conservation of mass equation becomes:

$$\frac{dV_{swallet}}{dt} = Q_{in} - v_{swallet} A_{swallet} \quad (56)$$

The equation can be further discretized and combined with the volume of water in a swallet as:

$$h_{swallet,i+1} = h_{swallet,i} + \frac{H_{swallet}\Delta t}{A_{swallet}L_{swallet}} Q_{in,i} - \frac{H_{swallet}\Delta t}{2L_{swallet}} (v_{swallet,i+1} + v_{swallet,i}) \quad (57)$$

where Δt is the temporal discretization of the model (s), and the subscripts i and $i+1$ represent previous and current timesteps.

For the second condition when the swallet is not full or connected to the creek, the flowrate into the creek is the lesser of the available water in the stream reach or quantified by a weir equation (Gupta, 2008):

$$Q_{in} = \frac{\pi D^2}{4} C_{weir} h_{stream}^{1.5} \quad for \quad h_{swallet} < H_{swallet} \quad (58)$$

where C_{weir} is a weir coefficient. The Darcy-Weisbach head-loss equation becomes:

$$h_{swallet} - \frac{P_c}{\gamma} = f \frac{h_{swallet} L_{swallet}}{H_{swallet} D} \frac{v_{swallet}^2}{2g} \quad for \quad v_{swallet} > 0 \quad (59)$$

$$h_{swallet} - \frac{P_c}{\gamma} = -f \frac{h_{swallet} L_{swallet}}{H_{swallet} D} \frac{v_{swallet}^2}{2g} \quad for \quad v_{swallet} < 0 \quad (60)$$

where $h_{swallet}$ is the height of water stored in the swallet (m).

4.2.5) Epikarst

The model formulates the epikarst as a storage and routing zone with multiple transfers possible. The formulation accounts for percolation of epikarst water to vadose rock zone (Q_{ep-v}) and connectivity of the epikarst to the fractures (Q_{ep-f}). An activation threshold height in the epikarst is used to trigger fracture flow during seasonally wet conditions and hydrologic events, consistent with the work of Tritz et al. (2011). The

model solves the conservation of mass equation for the epikarst to find the volume and height of water stored in the epikarst. Q_{ep-v} is calculated in the vadose zone model. Water is routed to the fracture network when the epikarst activation threshold is exceeded. During very wet conditions, the fracture network may fill with water, the epikarst storage may reach capacity, and therefore epikarst overflow occurs and water is routed to the surface stream (Q_{over}).

The application of the conservation of mass to the epikarst is

$$\frac{dV_{ep}}{dt} = Q_{inf} - Q_{perc} \text{ for } h_{ep} < h_{ep\ th} \quad (61)$$

where V_{ep} is the volume of water stored in the epikarst (m^3), Q_{inf} is infiltrated flow from the soil (m^3/s), Q_{perc} is water percolated from the epikarst to the vadose zone (m^3/s), t is time (s), h_{ep} is the height of water stored in the epikarst (m), and $h_{ep\ th}$ is the threshold height when epikarst water will be routed to the fracture network (m).

In the mass balance, the volume of water stored in the epikarst is

$$V_{ep} = h_{ep}A_{cell}n_{ep} \quad (62)$$

where A_{cell} is the area of the groundwater cell (m^2) and n_{ep} is the effective porosity of the epikarst. The previous equations are combined and discretized as

$$h_{ep}^{i+1} = h_{ep}^i + \frac{(Q_{inf} - Q_{perc})\Delta t}{A_{cell}n_{ep}} \quad (63)$$

where the i and $i+1$ superscripts represent previous and current temporal steps.

The activation of the fractures are also considered in the epikarst. When the height of water in the epikarst exceeds the threshold activation height then the excess water is routed to the fracture network and the height of water in the epikarst is

$$Q_{e,f} = \frac{(h_{ep}^{i+1} - h_{ep\ th})A_{cell}n_{ep}}{\Delta t} \quad \text{for } h_{ep} > h_{th} \quad (64)$$

$$h_{ep}^{i+1} = h_{ep\ th} \quad \text{for } h_{ep} > h_{th} \quad (65)$$

where $Q_{e,f}$ is the flowrate from the epikarst to the fracture network (m^3/s).

If during an extreme hydrologic event, the fracture network becomes filled with water, then the epikarst will route excess water to the surface stream system, i.e., an overflow, as

$$Q_{ep,stream} = \frac{(h_{ep}^{i+1} - h_{ep\ th})A_{cell}n_{ep}}{\Delta t} \quad \text{for } h_f = h_{f\ max} \quad (66)$$

$$Q_{e,f} = 0 \quad \text{for } h_f = h_{f\ max} \quad (67)$$

where $Q_{ep,stream}$ is the excess flowrate from the epikarst to the surface stream system (m^3/s), h_f is the height of water in the fracture network relative to the elevation of the conduit(m), and $h_{f\ max}$ is the maximum height that water in the fracture network can reach (m). The maximum height water in the fracture can reach is equal to the elevation difference between the bottom of the epikarst and the conduit node in the groundwater cell.

4.2.6) Vadose zone

The model simulates the vadose rock matrix as a variably saturated granular rock mass, where percolated epikarst water will be transported to a perched aquifer or the saturated rock matrix. Also, the model assumes that the effect of fractures and void volumes on unsaturated flow are negligible given that fracture flow is also accounted for. The formulation solves the Richard's Equation for unsaturated flow in the vadose zone similarly to models specifically for vadose zone processes (Niswonger et al. 2006; Simunek et al. 1998). The numerical model assumes that flow is gravity driven so that the diffusive term can be removed (Niswonger et al., 2006). The hydraulic conductivity is calculated using the Brooks-Corey function. The number of the vadose layers is found so that the CFL condition will not be violated, and the spatial discretization is equal to the thickness of each vadose layer. The velocity used for the unsaturated flow is that of the trailing wave, which is generally faster than the leading wave (Niswonger et al., 2006).

Richard's unsaturated flow equation is

$$\frac{\partial \theta}{\partial t} = \frac{\partial}{\partial z} \left[D(\theta) \frac{\partial \theta}{\partial z} - K(\theta) \right] - S \quad (68)$$

where θ is the volumetric water content, t is time (s), z is elevation (m), $D(\theta)$ is diffusivity (m^2/s), $K(\theta)$ is hydraulic conductivity (m/s), and S is a sink term.

The numerical model assumes that flow is gravity driven so that the diffusive term can be removed. This assumption was also used by Niswonger et al. (2006). Also, the numerical model assumes that there no sources or sinks of water in the vadose zone. In order to solve the Richard's Equations, the vadose zone is discretized into several thin layers, each with a volumetric water content. Using these assumptions and a mass-lumped

linear finite element discretization scheme, as in Simunek et al. (2013), Richard's equation becomes:

$$\frac{\theta_j^{i+1,k+1} - \theta_j^i}{\Delta t} = \frac{1}{2\Delta x} (K_{j+1}^{i+1,k} - K_{j-1}^{i+1,k}) \quad (69)$$

where the i and $i+1$ superscripts represent current and future time steps, the $j-1$ and $j+1$ subscripts represent previous and next vadose layer, and the k and $k+1$ superscripts represent current and future iteration levels.

The hydraulic conductivity is calculated using the Brooks-Corey function:

$$K(\theta) = K_s \left[\frac{\theta - \theta_r}{\theta_s - \theta_r} \right]^\epsilon \quad (70)$$

where K_s is the saturated hydraulic conductivity of the rock mass, θ_r is the residual volumetric water content of the rock mass, θ_s is the saturated water content of the rock mass, and ϵ is the Brooks-Corey coefficient.

The model of the vadose layers is estimated with the condition that the CFL condition will not be violated. The CFL condition is given generally from Courant et al. (1928) and specifically for the Richard's equation as

$$u \frac{\Delta t}{\Delta x} \leq 1 \quad \text{and} \quad \Delta x_{vadose} = \frac{\epsilon \Delta t K_s}{\theta_s - \theta_r} \quad (71)$$

where u is the velocity of the model (m/s), Δt is the temporal discretization of the model (s), Δx is the spatial discretization of the model (m), and Δx_{vadose} is the vertical length of a vadose zone layer (m). In the vadose zone, the spatial discretization is equal to the thickness of each vadose layer.

The velocity in this case is the velocity of the trailing wave, which is generally faster than the leading wave, and is given by Niswonger et al. (2006):

$$v(\theta) = \frac{\epsilon K_s}{\theta_s - \theta_r} \left[\frac{\theta - \theta_r}{\theta_s - \theta_r} \right]^{\epsilon-1} \quad (72)$$

where $v(\theta)$ is the velocity of the trailing wave (m/s).

4.2.7) Fracture Network

The model represents the fracture network as thin plate-like void spaces in the rock matrix that can store water and provide a pathway directly to the conduit. The fracture network exchanges water with the sinkholes, epikarst, perched aquifers, the saturated matrix and conduit. The formulation assumed flow to the vadose section of the fracture network will occur quickly, within the temporal step of the model, to the saturated water volume. An equivalent porous medium approach is used, where the geometry of the fracture network is represented by a set of parameters that are uniform across each sub-basin (Snow, 1969; Kresic, 2010). The numerical model explicitly solves the conservation of mass for the fracture network in each groundwater cell as a function of fracture density and fracture aperture, as well as the conservation of momentum. The model assumes that fractures have continuous width equal to the extent of the spatial distraction of a groundwater cell, therefore the representative fracture density encapsulates the physical fracture density of the network and the average width of fractures in the network. The conservation of momentum is applied in the form of the Cubic Law, similarly as others (Snow, 1969; Long et al., 1985; Bear et al., 1993; Zimmerman and Yeo, 2000). The Cubic

Law is derived from the Navier-Stokes equations and represents flow through a fractured rock zones (Lamb 1932; Muskat 1937; Snow, 1969; Zimmerman and Yao, 2000; Kresic, 2010). The derivation is based on the assumptions of “slow nonturbulent single-phase flow of an incompressible fluid” through two parallel plates (Snow 1969).

Each groundwater cell in the numerical model contains a fracture network with a geometry that can be parameterized by a representative fracture density N (1/m), and a fracture aperture b (m). The model assumes that fractures have continuous width equal to the extent of the spatial distraction of a groundwater cell, therefore the representative fracture density encapsulates the physical fracture density of the network and the average width of fractures in the network. The representative fracture network has a variable water storage volume with a free surface that can differ from the free water surface in the swallets or the groundwater table. The volume of water stored in the fracture network in a groundwater cell without an impermeable geologic member is:

$$V_f = h_f N b A_{cell} \quad (73)$$

where V_f is the volume of water stored in the fracture network, h_f is the height of the free water surface in the fracture network relative to the conduit node (m), and A_{cell} is the area of the groundwater cell (m²).

The fracture density and fracture aperture in an impermeable member may be different than the surrounding bedrock, depending on the composition and thickness of the member. The application of the conservation of mass to a fracture network yields

$$\frac{dV_f}{dt} = Q_{sink} + Q_{e,f} + Q_{pa,f} - Q_{f,c} \quad (74)$$

where Q_{sink} is the flow delivered to the fractures by sinkholes (m^3/s), $Q_{e,f}$ is the flow from the epikarst to the fracture network (m^3/s), $Q_{pa,f}$ is the flow between a perched aquifer and the fracture network (m^3/s), $Q_{f,c}$ is the flow between the fracture network and the conduit (m^3/s), and t is time (s). Positive values of $Q_{pa,f}$ indicate flow from the perched aquifer into the fracture network. Positive values of $Q_{f,c}$ indicate flow from the fracture network into the conduit, negative values indicate the conduit is recharging the fracture network.

The two previous equations can be combined and discretized to yield:

$$h_f^{i+1} = h_f^i + \frac{\Delta t}{NbA_{cell}} (Q_{sink} + Q_{e,f} + Q_{pa,f}) - \frac{\Delta t}{2NbA_{cell}} (Q_{f,c}^{i+1} + Q_{f,c}^i) \quad (75)$$

where the i and $i+1$ superscripts represent current and future temporal steps, and Δt is the temporal discretization of the model (s).

The Cubic Law is derived from the Navier-Stokes equations and represents flow through a fractured rock zones (Lamb 1932; Muskat 1937; Snow, 1969; Zimmerman and Yao, 2000; Kresic, 2010). The derivation is based on the assumptions of “slow nonturbulent single-phase flow of an incompressible fluid” through two parallel plates (Snow 1969). The application of the Cubic Law to a three-dimensional fracture network is:

$$q_f = \frac{\rho g}{6\mu} \frac{dh}{dx} Nb^3 \quad (76)$$

where q_f is the flow per unit area, or flow velocity of the flow in the fracture network (m/s), ρ is the density of water (1000 kg/m³), g is gravitational acceleration (9.8 m/s²), μ is the viscosity of water (Pa.s), h is the hydraulic head (m), x is a spatial coordinate.

The application of the cubic law to a phreatic conduit-dominated karst aquifer assumes that the hydraulic gradient $\frac{dh}{dx}$ is equal to the hydraulic head difference between the free surface of the water stored in the fracture network and the conduit, divided by the average total flowpath distance. This application of the cubic law is expressed as

$$q_f = \frac{\rho g}{6\mu} \frac{Nb^3}{(\Delta x_{cell} + h_f)} \left(h_f - \frac{P_c}{\gamma} \right) \quad (77)$$

where dx is the distance between the conduit node and the area-weighted center of the groundwater cell (m), P_c is the pressure at the conduit node (Pa), Δx_{cell} is the distance between the conduit and the area-weighted center of the groundwater cell, and γ is the specific weight of water (9.8 kN/m³).

Fracture flow to the surface stream via hillside springs may also be described with the cubic law equation. The hydraulic gradient is equal to the difference in elevation of the fracture height and the height of water in the stream relative to the conduit, divided by the lateral distance between the stream and the area-weighted center of the groundwater cell, which is assumed to be equal to the distance between the conduit and the area-weighted centroid of each groundwater cell. The application of the cubic law equation to the fracture network is:

$$q_{f,s} = \frac{\rho g}{6\mu} \frac{Nb^3}{(\Delta x_{cell})} (h_f - (H_{stream} + \Delta H_{stream})) \quad (78)$$

where $q_{f,s}$ is the fracture flow per unit area into the stream (m/s), h_{stream} is the height of water in the stream reaches located in the given groundwater cell (m), and ΔH_{stream} is the elevation difference between the stream reaches in the given groundwater cell and the conduit node located in the cell (m).

The total flow into the stream reach from the fracture network is the product of the per unit area fracture flow and the surface area of the stream reach:

$$Q_{f,s} = L_{stream} \left(B + 2m \sqrt{1 + h_{stream}^2} \right) \frac{\rho g}{6\mu} \frac{Nb^3}{(\Delta x_{cell})} (h_f - (H_{stream} + \Delta H_{stream})) \quad (79)$$

where $Q_{f,s}$ is the fracture flow into the stream reach (m³/s), L_{stream} is the length of the stream reach (m), B is the streambed width (m), and m is the stream channel side-slope (m/m).

4.2.8) Aquitards and Perched Water

The model formulation considers the potential for perched water tables in groundwater sub-basins due to the presence of an aquitard. The numerical model explicitly applies the conservation of mass principle to the variable-volume perched aquifer. The explicit linking of the perched aquifer with fracture flow considered herein is consistent with source/sink terms in other fracture network formulation (Snow, 1969; Zimmerman and Yao, 2000). Two types of flux are considered. The model computes Darcian flow exchange between the perched aquifer and the fracture network. In the case, the flowpath

distance and the area the flow exchange between the perched aquifer and the fracture network is computed using the fracture network geometry. The model also considers non-Darcian transfer to the fracture network when an activation height is reached. This condition reflects the perched aquifer reaching horizontal fractures, such as along a bedding plane, that are well-connected to the bulk fracture network.

The numerical model represents perched aquifers as a saturated variable-volume water storage reservoir in a porous medium. Each groundwater cell with the presence of an impermeable geologic member will have a perched aquifer. The volume of water stored in the perched aquifer is:

$$V_{pa} = h_{pa}n_m A_{cell} \quad (80)$$

where V_{pa} is the volume of water stored in the perched aquifer (m^3), h_{pa} is the height of the perched aquifer free water surface relative to the top of the impermeable geologic member (m), n_m is the porosity of the surrounding rock matrix, and A_{cell} is the surface area of the groundwater cell (m^2).

The model assumes that the impermeable geologic member is at a uniform elevation in a groundwater cell, and the height of the perched water table relative to the impermeable geologic member is uniform throughout a groundwater cell. The numerical model uses the conservation of mass principle to determine the volume of stored water in the perched aquifer and the height of the perched water table in each groundwater cell. The application of the conservation of mass to a perched aquifer is:

$$\frac{dV_{pa}}{dt} = Q_{vadose} - Q_{pa,f} \quad (81)$$

where t is time (s), Q_{vadose} is the flowrate of the percolating vadose zone water reaching the perched aquifer (m^3/s), and $Q_{pa,f}$ is an exchange flow between the fracture network and the perched aquifers (m^3/s), where positive flows indicate a flow direction from the perched aquifer to the fracture network. The two previous equations are combined and discretized as:

$$h_{pa}^{i+1} = h_{pa}^i + \frac{\Delta t}{nA_{cell}} (Q_{vadose}^i - Q_{pa,f}^i) \quad (82)$$

where i and $i+1$ superscripts represent previous and current model timesteps.

The conceptual model assumes that the exchange flow between the perched aquifer and the fracture network is saturated, incompressible, steady, laminar, groundwater flow through a porous medium. Darcy's law is the governing equation under these conditions, and the application of Darcy's law to a perched aquifer yields:

$$q_{pa,f} = K_s \frac{(h_{pa} + (h_f - H_{pa}))}{dx} \text{ for } h_f > H_{pa} \quad (83)$$

$$q_{pa,f} = K_s \frac{h_{pa}}{dx} \text{ for } h_f < H_{pa} \quad (84)$$

where $q_{pa,f}$ is the flowrate per unit width between the perched aquifer and the fracture network (m/s), k is the permeability of the rock matrix (m^2), μ is the viscosity of water (Pa.s), H_{pa} is the height of the top of the impermeable member relative to the conduit node (m), h_f is the height of the fracture network free surface relative to the conduit node (m), and h_f is the distance of the flow path (m).

The flowpath distance is related to the fracture network geometry:

$$dx \approx \frac{1.122}{4N} \quad (85)$$

where N is the representative fracture density (1/m).

The area the flow exchange between the perched aquifer and the fracture network occurs is also related to the fracture network geometry:

$$A_{pa,f} = 6Nh_{pa}A_{cell} \quad (86)$$

where $A_{pa,f}$ is the area of the fracture and perched aquifer flow exchange (m^2).

Combination of the previous equations results in:

$$Q_{pa,f}^{i+1} = \frac{24N^2h_{pa}A_{cell}}{1.122} K_s ((H_{pa} + h_{pa}) - h_f) \text{ for } h_f > H_{pa} \quad (87)$$

$$Q_{pa,f}^{i+1} = \frac{24N^2A_{cell}}{1.122} K_s h_{pa}^2 \text{ for } h_f < H_{pa} \quad (88)$$

4.2.9) Saturated Rock Matrix

The formulation represents the saturated rock matrix as a saturated variable-volume water storage reservoir in a porous medium with a lower permeability than the fracture network and the conduit network (White, 1999; Hartmann et al., 2013). The numerical model explicitly applies the unsteady conservation of mass principle to the storage zone, in a similar manner to how other authors model a saturated matrix storage reservoir for karst aquifers (Husic et al., 2016b). The model also uses Darcy's Law to compute the flow

between the saturated matrix and the conduit and cave network, in a similar manner to other karst models (Rooji et al., 2013, Reimann et al., 2013)

Each groundwater cell in the numerical model contains a saturated matrix. The numerical model represents the saturated matrix as a saturated variable-volume water storage reservoir in a porous medium. The volume of water stored in the saturated matrix is given by:

$$V_m = h_m n_m A_{cell} \quad (89)$$

where V_m is the volume of water stored in the saturated matrix (m^3), h_m is the height of groundwater table relative to the conduit node (m), n_m is the porosity of the rock matrix, and A_{cell} is the surface area of the groundwater cell.

The model assumes that the groundwater table elevation is uniform throughout a groundwater cell. The numerical model uses the conservation of mass principle to determine the volume of stored water in the saturated matrix and the height of the groundwater table in each groundwater cell. The application of the conservation of mass to the saturated rock matrix yields:

$$\frac{dV_m}{dt} = Q_{vadose} - Q_{m,c} \quad (90)$$

where t is time (s), Q_{vadose} is the flowrate of the percolating vadose zone water reaching the saturated matrix (m^3/s), and $Q_{m,c}$ is the flow exchange between the saturated matrix and the conduit. Positive values of $Q_{m,c}$ indicate flow is from the saturated matrix to the conduit, negative values indicate that the conduit is recharging the matrix.

Groundwater cells that include the presence of an impermeable geologic member will not have vadose zone flow that percolates to the saturated matrix. In those cells, all vadose zone percolation is intercepted by the impermeable geologic member and contributes to water storage in a perched aquifer. The previous two equations are combined and discretized to yield:

$$h_m^{i+1} = h_m^i + \frac{\Delta t}{nA_{cell}} \left(Q_{vadose}, -\frac{1}{2} (Q_{m,c}^{i+1} + Q_{m,c}^i) \right) \quad (91)$$

where i and $i+1$ superscripts represent previous and current model time-steps.

The conceptual model assumes that the exchange flow between the saturated matrix and the conduit is saturated, incompressible, steady, laminar groundwater flow in a porous medium. Darcy's Law provides an equation for flow under those conditions (Gupta, 2008):

$$q = -\frac{k}{\mu} \nabla P \quad (92)$$

where q is the flowrate per unit area (m/s), k is the permeability of the porous medium (m^2), μ is the viscosity of the fluid (Pa.s), and ∇P is the pressure gradient (Pa/m).

An assumption the conceptual model makes is that the pressure gradient is perpendicular to the conduit, therefore no saturated groundwater flow will occur between groundwater cells. The model assumes that this is valid for karst systems where the conduit network is the dominant flow component.

The permeability of the porous media is related to the hydraulic conductivity:

$$k = K_s \left(\frac{\mu}{\gamma} \right) \quad (93)$$

where K_s is the saturated hydraulic conductivity of the porous media (m/s), and γ is the specific weight of the fluid (N/m³).

The application of previous equation to the flow exchange between the matrix and the conduit is:

$$q_{m,c} = K_s \frac{\left(h_m - \frac{P_c}{\gamma}\right)}{\Delta x_{cell}} \quad (94)$$

where $q_{m,c}$ is the flow per unit area between the conduit and saturated matrix (m/s), P_c is the pressure at the conduit node (kPa), γ is the specific weight of water (9.8 kN/m³), and Δx_{cell} is the distance between the conduit node and the area weighted center of the groundwater cell (m).

The area that flow between the saturated matrix and the conduit takes place is equal to the surface area of the conduit wall:

$$A_{m,c} = \pi D L_c \tau_c \quad (95)$$

where $A_{m,c}$ is the surface area of the conduit (m²), D is the diameter of the conduit (m), L_c is the straight-line length of the conduit in a groundwater cell (m), and τ_c is the tortuosity of the conduit.

The combination of the previous two equations provides the flow exchange between the matrix and the conduit:

$$Q_{m,c} = \pi D L_c \tau_c K_s \frac{\left(h_m - \frac{P_c}{\gamma}\right)}{\Delta x} \quad (96)$$

4.2.10) Phreatic and Epiphreatic Conduits

The model represents conduits as subterranean pipes that dominate sub-surface flow because of the fast-turbulent conditions. Additionally, phreatic and epi-phreatic conduits can interact and exchange flow with swallets, the fracture network, and the saturated rock matrix, and convey water to a spring. The numerical model represents a conduit network as a set of pipe sections that intersect at nodes. The numerical model uses the Darcy-Weisbach equation and the conservation of mass principle to calculate the conduit flowrates, similarly to others (Jeannin, 2001; Shoemaker et al., 2008; Rooji et al., 2013; Chen and Goldscheider, 2014).

The Darcy-Weisbach head-loss equation is:

$$\Delta h = f \frac{l}{d} \frac{v^2}{2g} \quad (97)$$

where Δh is the change in hydraulic head, or head loss, between two points (m), f is the Darcy-Weisbach friction factor, l is the length of the flowpath between the two points (m), d is the diameter of the pipe or conduit (m), v is velocity of water between the two points (m/s), and g is gravitational acceleration (9.8m/s²).

The application of the Darcy-Weisbach equation to the conduit network is written as:

$$\frac{p_c^j}{\gamma} + z_c^j - \frac{p_c^{j+1}}{\gamma} - z_c^{j+1} = f \frac{l_c \tau_c}{D} \frac{(v_c^j)^2}{2g} \quad (98)$$

where p_c^j is the hydrostatic pressure at the current node (Pa), z_c^j is the elevation of the current conduit node (m), p_c^{j+1} is the hydrostatic pressure at the next conduit node (Pa),

z_c^{j+1} is the elevation of the next conduit node, γ is the specific weight of water (9.8 kN/m³), l_c is the straight-line length of conduit between nodes (m), τ_c is the tortuosity of the conduit, D is the diameter of the next conduit section, and v_c^j is the velocity of water in the next conduit section (m/s).

The numerical model solves the conservation of mass at each conduit node:

$$Q_c^{j-1} + Q_{swallet} + Q_{f,c} + Q_{m,c} - Q_c^j = 0 \quad (99)$$

where Q_c^{j-1} is the flow into the conduit node from the previous conduit segment (m³/s), $Q_{swallet}$ is the flowrate into the conduit from a swallet (m³/s), $Q_{f,c}$ is the flowrate into the conduit from the saturated matrix (m³/s), and Q_c^j is the flowrate out of the conduit node and into and through the next conduit segment (m³/s).

The equation can also be written as a function of flow velocities:

$$v_c^{j-1} A_c^{j-1} + v_{swallet} A_{swallet} + (q_{f,c} + q_{m,c}) \pi D L_c \tau_c - v_c^j A_c^j = 0 \quad (100)$$

where v_c^{j-1} is the flow velocity in the previous conduit segment (m/s), A_c^{j-1} is the cross-sectional area of the previous conduit segment (m²), $v_{swallet}$ is the flow velocity through the swallet (m/s), $A_{swallet}$ is the cross-sectional area of the swallet (m²), $q_{f,c}$ is the flow velocity of water from the fracture network into the conduit (m/s), $q_{m,c}$ is the flow velocity from water in the saturated matrix into the conduit, D is the diameter of the conduit at the conduit node, L_c is the straight line length of the conduit in the groundwater cell (m), τ_c is the tortuosity of the conduit, v_c^j is the flow velocity into the next conduit segment (m/s), and A_c^j is the cross-sectional area of the next conduit segment (m²).

4.2.11) Springflow

The numerical model calculates springflow by a simultaneous solution of the flowrate and mass balance equations for the conduit, swallets, fracture network, and saturated matrix at every groundwater cell. The simultaneous solution requires a boundary condition at the spring. This boundary condition is the elevation of surface water at the spring. This condition eliminates a pressure head term in the Darcy-Weisbach equation for the final conduit segment because the surface water at the spring has a free surface. This updated equation is expressed as

$$z_{spring} - \frac{p_c^j}{\gamma} - z_c^j = f \frac{l_c \tau_c}{D} \frac{(v_c^j)^2}{2g} \quad (101)$$

where z_{spring} is the elevation of the free water surface at the spring (m).

4.2.12) Fracture to Matrix Flux

Groundwater can exchange between the fracture network and the saturated bedrock matrix. Darcy's Law governs the flux between the fracture network and saturated bedrock matrix. The flowpath distance is related to fracture geometry as represented by equation 85. The area the flow exchange between the perched aquifer and the fracture network occurs is also related to the fracture network geometry:

$$A_{f,m} = 6N h_m A_{cell} \quad (102)$$

where $A_{f,m}$ is the area of the fracture and perched aquifer flow exchange (m^2), N is the fracture density ($1/m$), h_m is the height of water stored in the saturated matrix (m), and A_{cell} is the area of the groundwater cell (m^2).

The application of Darcy's Law to the fracture network and saturated matrix flux is:

$$Q_{f,m} = \frac{24N^2 h_m A_{cell}}{1.122} K_s (h_f - h_m) \quad (103)$$

where $Q_{f,m}$ is the flowrate from the fracture network to the saturated matrix (m^3/s), h_f is the height of water stored in the fracture network (m), K_s is the hydraulic conductivity of the saturated matrix (m^2), and μ is the viscosity of water (Pa.s).

4.3) Modeling Inputs, Discretization, and Parameterization

4.3.1) Model Inputs and Discretization

The model spatial domain of the surface watershed and subsurface groundwater basin was constructed using inputs from geospatial data and previously collected measurements of subsurface resistivity and groundwater tracing for the basin. Model inputs are summarized in Table 2. Geospatial data sources are summarized in Table 1.

The surface watershed boundary was constructed using a digital elevation model and analyses in a GIS software. The Cane Run surface watershed has landscape sinkholes in numerous locations, and therefore a sinkhole map previously constructed by the Kentucky Geological Survey was input to provide sinkhole locations and mapped drainage

areas. The pathway of Cane Run Creek and its tributaries were input using USGS geospatial stream hydrology dataset. Cross section and longitudinal dimensions, such as stream gradient (s), bank height (h_{bkf}), bed width (B) and side slope (m), of Cane Run Creek were input using analyses of a 0.5 m topographic model of the basin, constructed using a 5-foot DEM of the area. Swallets, i.e., acting as in-stream sinkholes or estavelles, are located throughout Cane Run Creek, and therefore swallets in the stream corridor were input using a 20m buffer around the stream network masked over the previously mentioned sinkhole geospatial model. Geographic coordinates of the swallet locations are shown in Table 3. Swallet dimensions were input using data from a field survey constructed by the research team in which geometry of the openings were measured (Puckett, 2015). The soil layer covering the limestone bedrock was mapped using USDA NRCS digitized soil survey data. The epikarst layer was constructed immediately below the soil layer. The epikarst thickness (H_{ep}) was input using results from soil electrical resistivity across the basin (Landrum et al., 2013).

The Royal Spring groundwater basin boundary was previously constructed by the KGS using groundwater tracer studies (Taylor, 1992; Paylor and Currens, 2004). The limestone bedrock layer of the groundwater basin and its fracture network were constructed below the epikarst layer. The vertical dimension of the limestone layer was extended below the primary conduit that drains the groundwater basin to Royal Spring. The geometry of fractures and density of fractures across the bedrock were left as parameters in the model because our existing resistivity measurements could not resolve these characteristics. However, local variation of fracture density was input to the model's spatial domain with some physical considerations. Fractures occur as a result of stresses and folding during

tectonic activity (Ford and Ewers 1982; White 2002), and evidence suggests both regional and local folding can influence fracture density in karst (Harris et al., 1960; Hanks 1997; Florea 2005). We used stratigraphic curvature estimated with the geospatial layer of bedrock member elevation to predict local fracture density. Stratigraphic curvature was input to the spatial domain by approximating the second derivative of the bedrock surface using a spatial analyses function built into the geospatial software (see curvature result in Figure 9 through 11). An aquitard known as the Cane Run Bed exists throughout the groundwater basin, and geologic maps and survey data, analyses of stage recordings from wells in perched aquifers, and borehole logs were used to input the vertical location and thickness of the impermeable members.

We constructed the spatial domain of the primary conduit that daylight at Royal Spring by accounting for a number of considerations, including, previous measurements and dye tracing in the conduit (Thraillkill et al., 1991), resistivity measurements (Zhu et al., 2011), downhole video and additional recent dye traces (Husic et al., 2017a and references therein), borehole logs and elevations of wells directly intersecting the conduit (Zhu et al., 2011; Husic et al., 2017a), and physical controls on karst conduit development from bedding planes and water table elevations (Ewers, 1972; Ford and Ewers, 1978; McCoy and Kozar, 2007; Fillipponi et al., 2009; Malard et al., 2015). The measurements and past research allowed us to arrive at a hypothesized conduit profile that improves upon the original hypothesized conduit profile of Thraillkill et al. (1991). The hypothesized conduit profile (see Figure 6) follows a bedding plane approximately 12 meters below the Cane Run Bed for most of its length until the local anticline near the spring, where it shortcuts to the spring. Evidence of the profile is supported by the vertical location of the conduit

found with an intersecting well near the center of the basin (see KWHP site in Figure 9 and 10), which corresponds with the same bedding plane layer at the base level of North Elkhorn Creek. The shortcut to Royal Spring, rather than termination at North Elkhorn Creek, is attributed to karst formation that maximizes hydraulic efficiency and development along a shallow gradient (Phillips 2014). We suggest that early in conduit development, a fracture or overflow spring at the location of present day Royal Spring was preferred to maximize hydraulic efficiency and avoid the steep gradient of the bedding plane from the proximity of Royal Spring to North Elkhorn Creek. Thrailkill et al. (1991) suggested the shortcut was a result of an impermeable geologic structure but later investigated mapped lithology of this region did not reveal any evidence of such. The elevation of Royal Spring is used as a maximum conduit elevation, which is consistent with the concept that conduits develop at or below the water table elevation (Ford and Ewers, 1978; Malard et al., 2015). This condition also conveniently ensures the assumption of phreatic conduit flow will not be violated in the numeric model. Cross section dimensions of the elliptical conduit were input from a variety of measurements described in Husic et al. (2017a).

Spatial discretization of the model domain was performed and guided by the availability of hourly inputs for weather data. Precipitation and other weather variables were collected from local gaging stations and are detailed in Table 4. The availability of hourly rainfall data provided a minimum hourly time step for the model, although simulation was also performed a coarser time steps, as detailed in the model evaluation and results sections. Inputs for discretized spatial cell geometries and features are compiled herein for the watershed surface, stream network, groundwater basin, and conduit. In

addition, information from the discretization was calculated by differencing, averaging and post-processing of the discretized spatial domain, such as swallet and conduit straight-line distances and swallet equivalent diameters. This information is shown for their ranges in Table 2 and included specifically with variables for each cell in supplemental Tables 5 through 8 and in Figures 4 through 5 and Figures 9 through 16. These inputs included: number of watershed surface cells (Table 2), conduit lengths (L_c , Table 5), conduit elevations (z_c , Table 5), conduit diameter (D_c , Table 5), swallet diameter (D_s , Table 6), groundwater cell area (A_{cel} Table 7, Figure 4), Cane Run Bed height relative to conduit (H_{pa} Table 7, Figure 5), epikarst bottom height relative to conduit ($h_{f,max}$ Table 7), stratigraphic curvature (Table 7, Figure 9), maximum lateral distance for fracture and matrix flow (dx_{max} , Table 7, Figure 15), number of groundwater wells (Table 7, Figure 16), number of stream reaches (Table 2), stream bed widths (B , Table 8), stream bed slopes (s , Table 8), and bankfull heights (h_{bkf} , Table 8).

A number of additional inputs to the model were specified using the literature. The discharge-coefficient for weir flow (c_w) into the swallet while the swallet isn't full was selected based on reported broad-crested weir coefficients (Gupta 2008). The value of the Brooks-Corey exponent (E) is assumed to be equal to the value used by Brooks and Corey (1964) in the Brooks-Corey equation. The residual moisture content (θ_r) in the unsaturated zone is assumed to be zero, as suggested by Simunek et al. (1998) in order to reduce the number of model parameters. The value for conduit tortuosity (τ_c) is assumed to be within the ranges of conduit tortuosity reported for looping cave systems and water-table cave systems by Jouvès et al. (2010). Values for these inputs are displayed in Table 2. The pump rate in each groundwater cell is the product of the pump rate parameter and the number of

active wells in the groundwater cell. The locations of all wells in the groundwater basin were identified using a dataset provided by the Kentucky Geological Survey Groundwater Data Repository (Details in Table 1). This set of wells was filtered to only include active wells (Figure 16).

4.3.2) Model Parameterization

The numerical model was parameterized using 16 parameters. Table 9 shows the range and calibrated value of each parameter. One of the parameters for the stream and groundwater model was the “SWAT Run”, which corresponds to a SWAT model for the Cane Run watershed with a unique parameter set. The unique parameter sets were chosen from a set of calibrated SWAT model runs for the Upper South Elkhorn watershed, located approximately 16 kilometers from the Cane Run Watershed. The Upper South Elkhorn watershed does not exhibit mature karst development, but shares similar watershed characteristics to the Cane Run watershed. The SWAT model used in the Upper South Elkhorn used 14 parameters, similarly to previous SWAT models used by researchers studying the watershed (Al Aamery et al., 2016); however, the value of the deep aquifer percolation fraction (RCHRG_DP) was set to 1 for SWAT model runs in the Cane Run watershed. This also negated six other parameters that relate to groundwater. As a result, only seven SWAT parameters were important for the Cane Run watershed simulations. Out of the 25 SWAT parameter sets with acceptable performance metrics for the Upper South Elkhorn watershed chosen to be used in the Cane Run watershed, 14 sets represented a high and low value of each of the seven SWAT parameters important in the Cane Run

Watershed, 1 set produced the best performance in the Upper South Elkhorn watershed, and 9 sets were chosen randomly. The values of parameters used in each 25 SWAT runs are shown in Table 10.

The initial range for the matrix porosity (n_m) were selected based on values for limestone bedrock in karst aquifers reported in literature (Worthington et al., 2000; Williams, 2008). The range for saturated hydraulic conductivity of the limestone bedrock (K_s) were selected based on minimum and maximum values of hydraulic conductivity reported for limestone bedrock by Domenico and Schwartz (1990). The range for epikarst porosity (n_{ep}) were selected based on values suggested in epikarst literature (Klimchouk, 2004; Williams, 2008). The maximum value in the initial epikarst fracture threshold height parameter (ep_{th}) was selected based on the estimated maximum thickness of the epikarst layer, which was determined by the difference in high and low values of soil thickness determined by an electroresistivity survey (Landrum et al., 2013). The minimum value for ep_{th} was assumed to be a low value so that the parameter was not over constrained without justification. The minimum pump rate value was assumed to be zero, while the maximum pump rate was selected based on high-end values of reported pumping rates from wells in the Greir Member in Fayette Co, KY, where the Royal Springs Aquifer is located (Carey and Stickney, 2005). The SWAT run parameter range is equal to the number of individual SWAT input sets that were generated. The maximum value for fracture density (N) was selected based on reported fracture densities common in epikarst zones, and the minimum value was selected based on lower end values reported for karstified limestone bedrock (Kimchouk, 2004). The range for Manning's roughness coefficient (n) were selected based on values for clean, straight reaches to very weedy reaches (Chow, 1959). The range for

fracture aperture (b) was selected based on a range of fracture apertures that resulted from a karst evolution model (Worthington and Ford, 2009). The initial range for the flood wave coefficient (k_s) was selected based on the maximum theoretical range identified by Jain (2001). The initial range for the conduit friction factor (f_c) was selected based on the range of friction factors appearing on the Moody Diagram (Moody, 1944). The swallet friction factor (f_s) was assumed to have a higher upper bound than the conduit friction factor because of the losses associated with irregular geometries expected in the swallets. Swallet tortuosity (τ_s) was assumed to be equal to or greater than the conduit tortuosity. The range for the local curvature weighting factor (α_{LC}) was selected so that it would have as large of a range that was assumed to be physically possible. Ranges for both the fracture lateral distance adjustment factor (dx_f) and the matrix lateral distance adjustment factor (dx_m) were assumed to have a maximum value of one, corresponding to the centroid-based distance for each groundwater cell, and a low value corresponding to a lateral distance approximately equal to the height of the groundwater table.

4.4) Model Setup

The numeric model consisted of three components including a SWAT model that used precipitation and weather data to predict tributary flow, surface runoff, lateral flow, and soil percolation, a streamflow and groundwater model that simulated fluvio-karst processes to predict streamflow and spring discharge, and an intermediate component that transformed SWAT outputs into inputs for the stream and groundwater model. A schematic of the workflow process is shown in Figure 17. The initial steps required to run the model

include gathering various input data. This includes precipitation and weather data, as well as geospatial data such as land use, soil type, surface elevations, sinkhole drainage areas, swallet locations, aquifer boundaries, etc. A summary of data sources used in our model are shown in Table 1.

After required inputs have been gathered, the SWAT model is ran for the watershed. Researchers studying karst watersheds have often modified a SWAT model to better simulate streamflow in fluviokarst watersheds or to improve karst groundwater models by improving the simulation of surface and soil hydrologic processes (Baffaut and Benson, 2009; Yactayo et al., 2009; Amatya et al., 2001; Palanisamy and Workman, 2014; Malago et al., 2016).

The SWAT model was adjusted to better simulate the effects of karst on hydrologic processes, in a way that could easily be integrated with the stream and groundwater model that simulates fluviokarst. In addition the adjusting SWAT outputs to re-proportion some surface runoff and lateral flow into sinkholes, the deep aquifer percolation fraction (RCHRG_DP) was set to 1. This negates the shallow aquifer and will prevent baseflow to streams, a process that is simulated in the stream and groundwater component of the numeric model. This method is similar to the method presented in Malago et al. (2016), where the deep aquifer percolation fraction was also set to one to negate the shallow aquifer.

The spatial discretization of the SWAT component of the model and the stream and groundwater component of the model are different. Additionally, the surface runoff and lateral flow processes simulated in the SWAT model must be divided between sinkholes

and streams, to more accurately represent all fluviokarst processes. The intermediate component of the numeric model re-proportions and groups tributary flow, surface runoff, lateral flow, and percolation outputs into stream inputs, sinkhole drainage, and percolation into the epikarst which act as the inputs to the stream and groundwater model. The method used by the intermediate model component to achieve this uses the proportion of overlapping areas between SWAT spatial components, the stream and groundwater spatial components, and the drainage area of sinkholes to adjust and group SWAT outputs.

Once the outputs from SWAT have been transformed into stream and groundwater model inputs, the stream and groundwater model can be ran. The stream and groundwater model is composed of three model structures: a stream reach model, an upper groundwater model, and a lower groundwater model. The stream reach model routes streamflow and calculates weir-flow into the swallets during non-full conditions. The upper groundwater model calculates the mass balance for the epikarst and perched aquifer, and calculates unsaturated flow in the vadose zone. The lower groundwater model component solves a system of equations including mass balances and flowrate/head-loss equations for the conduit, swallet, fracture network, and saturated matrix in each groundwater cell.

4.5) Model Evaluation

4.5.1) Calibration and Validation

Calibration and validation of the numeric model was performed in two stages: 1) calibration of the surface and soil model, and 2) calibration of the karst and streamflow

model. The calibration and validation process are summarized with a flow diagram in Figure 18.

4.5.1.1) Stage One: SWAT

The SWAT model was utilized to provide surface runoff and lateral flow, and soil percolation inputs to the karst model. Calibration of the SWAT model was performed in the Upper South Elkhorn Watershed, a nearby watershed with similar size and watershed characteristics, but without the extensive fluviokarst development seen in the Cane Run Watershed. This decision was made because SWAT models alone are either insufficient or incapable of replicating stream hydrographs in karst systems (Baffout and Benson, 2009; Amatya et al., 2011; Palanisamy and Workman, 2014) and the limited availability of streamflow data at the basin outlet.

The Upper South Elkhorn Watershed outlet is located approximately 9 km from the outlet of the portion of the Cane Run Watershed within the Royal Springs Groundwater Basin. A comparison of watershed characteristics between the two watersheds is provided in Table 11, and a map of the watershed is provided in Figure 19. The SWAT model for each watershed was created using the same weather data, and both models used the same number of sub-basins. Streamflow data used to calibrate the SWAT model in the Upper South Elkhorn was provided from the Fort Springs, KY stream gauge (USGS 03289000). The SWAT model was calibrated for years 2010 through 2017 with 2008 and 2009 utilized as model spin-up years.

The selection of parameters and initial parameter values for the calibration of the SWAT model was selected based on a previous research in the Upper South Elkhorn Watershed that utilized a SWAT model (Al-Aamery et al., 2016). Initial parameter values are provided in Table 12. SWAT-CUP was executed using the SUFI2 procedure with 1000 iterations. Parameters that yielded model runs with a value of the R^2 objective function were accepted as acceptable model runs. If the number of accepted sets were too few to investigate uncertainty in the model or to create several sets of inputs to the karst and stream model, the new parameter set generated from the SUFI2 optimization algorithm (Abbaspour et al., 2007) was adopted and another set of 1000 iterations was performed. This was repeated no more than four times, after which additional SWAT parameters would be added to the model.

After the final set of acceptable runs was identified, twenty-five parameter sets with varied parameter values were applied to the Cane Run Watershed. Each parameter set generated surface runoff and lateral flow values that act as inputs to sinkholes and the stream, and percolation values that serve as inputs to the epikarst. The set of inputs to be selected for use in the karst model becomes a parameter in the karst model named “SWAT run”.

4.5.1.2) Stage Two: Stream and Groundwater Model

The goal of the karst and streamflow model calibration was to (i) refine the initial parameter space parameter space and then (ii) find optimal parameter values that met objective criteria including traditional statistical measures and visual fit. Initial parameter

ranges were selected based on values reported in literature and best guesses for parameter ranges unique to this model and are reported in Table 9. Using the initial parameter range, a Sobol sequence was used to generate 500 sets of parameter values. These parameter sets were then used to perform short-duration model runs. Shorter-duration model runs were chosen over full-duration so that more calibration iterations could be performed with the limited computational resources and time available.

Parameter sets that yielded model runs with spring flow and streamflow NSE values greater than zero, PBIAS values less than 25, and simulated hydrograph peaks and recessions had graphical agreement with observed hydrographs in the spring and in the stream were accepted. Values of individual parameter from the set of accepted model runs were plotted. Parameters that had a portion of the initial parameter range without any acceptable model runs were removed from next parameter ranges. The SUFI2 optimization algorithm for determining optimal parameter ranges as discussed in Abbaspour et al. (2007), was also utilized to predict new parameter ranges. These two methods were utilized to generate new parameter ranges. An additional 500 parameter sets were generated using Sobol sequencing, and short-duration model runs was performed. This procedure was repeated until the entire range for each parameter yielded acceptable model runs. If the procedure was repeated four times, then adding additional parameters or changing the model structure would be considered.

Spring discharge recorded at the Royal Springs gauge (USGS 03288110) in Georgetown, KY was adjusted for abstractions by the Georgetown Municipal Water and Wastewater Service and used as a primary calibration data set. Streamflow recorded by a gage at the basin outlet (UKCAFE, 2011) was used as a secondary calibration dataset.

Evaluation metrics of NSE, and PBIAS were chosen based on recommendations by Moriasi et al. (2007). Graphical comparison between the simulated and observed spring and stream hydrographs also provided insight into the performance of separate parameter sets.

The optimal parameter values for the karst and streamflow model were estimated by using an automated approach. This included generating 2,000 unique parameter sets using Sobol sequencing, and the refined parameter ranges from semi-manual calibration. The karst model ran for the time period from December 1, 2010 to December 31, 2017, using the first month of simulation as model spin-up, five years for calibration, and two years as validation. Evaluation objective functions of NSE and PBIAS were used because of recommendations from Moriasi et al. (2007). For simulations on a monthly time scale, Moriasi et al., (2007) recommends $NSE > 0.5$ and $PBIAS < 25$ as acceptable performance criteria. Model simulations on higher resolution time scales are known to have lower values of performance metrics when compared to performance of the model when data is aggregated for a lower resolution time scale (Engel et al., 2007; Moriasi et al., 2007). Therefore, model runs with $NSE > 0.4$ and $PBIAS < 25$ for spring discharge were accepted. If no model runs produced acceptable results, the parameter ranges would be adjusted using the SUFI2 optimization algorithm. This would be repeated no more than four times, at which point either additional parameters would be added or the model or the model structure would be modified.

4.5.2) Sensitivity and Uncertainty Analysis

Global sensitivity was measured using a multiple regression model. This was chosen based on the ease of performance and a lower number of model simulations required to calculate the sensitivity. The multiple regression model is considered to regress the parameters values (x) sampled by the Sobol sequence against the values of the objective function (y).

$$y = a + \sum_{i=1}^m b_i x_i \quad (105)$$

where m is the number of simulations, a is the model interception, and b is the parameter coefficient. The t-test is then used to identify the significance effect of each parameter of the objective function (Abbaspour et al., 2007). Model performance is assumed to be sensitive to parameters with a P-value less than 0.5 as a result from the t-test.

Model uncertainty as measured by evaluating the mean and standard deviation of acceptable model runs for each time step. Additionally, the average thickness of the 95% prediction uncertainty (95 PPU), was evaluated. The 95 PPU was constructed using the 2.5% and 97.5% quantiles of the streamflow values across all acceptable model runs for each time-step (Abbaspour et al., 2007).

Table 2. Model Inputs

Name	Symbol	Value	Units	Source
Brooks-Corey Exponent	ϵ	4	-	Brooks and Corey 1964
Conduit Tortuosity	τ_c	1.2	m/m	Jouves et al., 2010
Residual Moisture Content	t_r	0	%	Simunek et al., 1999
Gravitational Acceleration	g	9.8	m/s ²	Munson, 2012
Specific Wight	γ	9800	N/m ²	Munson, 2012
Dynamic Viscosity	μ	0.0013	(N-s)/m ²	Munson, 2012
Channel Side-Slope	m	2.5	m/m	5-ft DEM
Weir Coefficient	c_w	0.85	-	Gupta 2008
Epikarst Thickness	H_{ep}	1	m	Landrum et al., 2013
Number of Groundwater Cells		16	-	Assigned
Conduit Length	L_c	500 to 1470	m	Assigned
Conduit Elevation	z_c	235.3 to 244.8	m	Hypothesized Profile
Conduit Diameter	D_c	1.27 to 1.37	m	Husic et al., 2016b
Swallet Diameter	D_s	0.45 to 0.86	m	Pucket, 2015
Cell Area	A_{cell}	1.1 to 13.6	Km ²	Assigned
Cane Run Bed Height	H_{pa}	9.8 to 37.3	m	Cressman 1967
Epikarst Bottom Height	$h_{f,max}$	15.9 to 48.8	m	Landrum et al., 2013
Stratigraphic Curvature		0.03 to 0.29	-	Cressman, 1967
Maximum Fracture/Matrix Lateral Distance	dx_{max}	367 to 1296	m	Assigned
Number of Groundwater Wells		0 to 8	-	Kentucky Groundwater Data Repository
Number of Stream Reaches		17	-	Assigned
Stream Bed Width	B	3.57 to 7.45	m	5-ft DEM
Stream Bed Slope	s	0.0002 to 0.0055	m	5-ft DEM
Bankfull Height	h_{bkf}	0.64 to 1.36	m	5-ft DEM

Table 3. Swallet Coordinates

Swallet	Longitude	Latitude
1	-84.53734	38.16575
2	-84.53466	38.16453
3	-84.52454	38.15234
4	-84.52497	38.15163
5	-84.52377	38.15041
6	-84.52281	38.14923
7	-84.52062	38.14765
8	-84.52062	38.14752
9	-84.52065	38.14741
10	-84.52062	38.14718
11	-84.52051	38.14551
12	-84.51958	38.14352
13	-84.51862	38.14251
14	-84.51769	38.14141
15	-84.51779	38.14094
16	-84.51513	38.13709
17	-84.5133	38.13432
18	-84.51301	38.13391
19	-84.51277	38.13365
20	-84.50688	38.11554
21	-84.50127	38.10858
22	-84.49994	38.10744
23	-84.49832	38.10336
24	-84.49798	38.09962
25	-84.50005	38.09684
26	-84.50053	38.09008
27	-84.49494	38.0835
28	-84.48968	38.07771
29	-84.48367	38.07417
30	-84.4792	38.07312

Table 4. Weather Data Sources.

Dataset	Source
Hourly Precipitation	NOAA Bluegrass Airport
Daily Temperature (min,max)	NOAA Bluegrass Airport
Daily Relative Humidity	NOAA Bluegrass Airport
Daily Wind Speed	NOAA Bluegrass Airport

Table 5. Conduit Inputs

Conduit	Elevation (m)	Length(m)	Diameter (m)
1	244.8	1470	1.27
2	244.8	1000	1.28
3	244.8	1000	1.29
4	244.8	1000	1.30
5	244.8	1000	1.32
6	244.8	1000	1.33
7	243.9	1000	1.34
8	238.3	1000	1.37
9	237.0	1000	1.37
10	235.3	1000	1.37
11	237.3	1000	1.37
12	238.5	1000	1.37
13	241.9	1000	1.37
14	242.3	1000	1.37
15	241.7	1000	1.37
16	243.2	500	1.37

Table 6. Swallet Diameters

Swallet	Diameter (m)
1	0.59
2	0.45
3	0.45
4	0.45
5	0.70
6	0.45
7	0.45
8	0.45
9	0.70
10	0.45
11	0.78
12	0.86
13	0.78
14	0.59

Table 7. Groundwater Inputs

Cell	Area (m ²)	Cane Run Bed Height (m)	Epikarst Bottom Height (m)	Stratigraphic Curvature	Maximum Fracture and Matrix Lateral Distance (m)	Number of Wells
1	13644297	37.3	48.8	0.0932	1296.0	8
2	3363365	32.0	39.6	0.0924	938.0	1
3	6350942	26.9	36.8	0.1625	1686.5	1
4	4258691	22.8	33.0	0.1548	1139.4	0
5	4439923	21.3	31.0	0.1586	1125.5	1
6	3761571	19.4	29.0	0.2921	953.6	5
7	4118069	17.6	28.9	0.1901	1055.6	0
8	3759692	21.2	32.3	0.1978	1023.7	4
9	3136562	20.8	32.5	0.1804	1038.5	4
10	2910928	21.1	32.2	0.2230	907.1	1
11	3031705	18.3	28.8	0.1666	932.0	3
12	2531433	16.2	25.9	0.0885	759.0	1
13	1468076	14.0	27.5	0.0848	510.5	0
14	1416624	14.2	28.7	0.0356	418.3	0
15	1275362	13.9	25.8	0.0463	386.5	0
16	1132051	9.8	15.9	0.0556	367.2	0

Table 8. Stream Reach Inputs

Reach	Length (m)	Bed Width (m)	Bed Slope (m/m)	Bankfull Height (m)	Elevation (m)
1	1081.9	3.57	0.0055	0.64	288.4
2	1081.9	4.20	0.0055	0.81	282.5
3	986.4	4.96	0.0027	0.99	278.1
4	986.4	5.04	0.0027	1.00	275.4
5	1151.8	5.34	0.0027	1.06	272.6
6	1151.8	5.43	0.0027	1.08	269.5
7	379.3	5.75	0.0003	1.13	267.9
8	1149.0	5.97	0.0022	1.17	266.5
9	1149.0	6.06	0.0022	1.18	263.9
10	1064.9	6.31	0.0011	1.22	262.1
11	966.3	6.90	0.0014	1.30	260.8
12	966.3	6.96	0.0014	1.31	259.5
13	457.8	7.06	0.0013	1.32	258.5
14	1176.0	7.18	0.0022	1.33	256.9
15	1176.0	7.22	0.0022	1.34	254.3
16	729.0	7.43	0.0002	1.36	252.9
17	729.0	7.45	0.0002	1.36	252.8

Table 9. Karst Model Parameters Ranges

Parameter Name	Symbol	Initial Range		Final Range		Units	Reference/Justification
		Min	Max	Min	Max		
Matrix Porosity	n_m	1×10^{-3}	0.02	1×10^{-3}	0.02	%	Worthington et al., 2000; Williams, 2008
Saturated Hydraulic Conductivity	K_s	1×10^{-9}	5×10^{-6}	1×10^{-9}	5×10^{-7}	m s^{-1}	Domenico and Schwartz, 1990
Epikarst Porosity	n_{ep}	0.02	0.3	0.02	0.3	%	Klimchouk, 2004; Williams, 2008
Epikasrt-Fracture Threshold Height	ep_{th}	0.01	1	0.01	1	m	Zhu, 2011
Pump Rate	q_{pump}	5×10^{-6}	0.01	5×10^{-6}	0.01	$\text{m}^3 \text{s}^{-1}$	Carey and Stickney, 2005
SWAT Run	SWAT	1	25	1	25	-	25 of Accepted SWAT Runs
Fracture Density	N	0.01	5	0.01	0.9	m^{-1}	Klimchouk, 2004
Manning's n	n	0.025	0.15	0.008	0.2	$\text{m}^{1/6}$	Chow 1959
Fracture Aperture	b	0.001	0.05	0.001	0.05	m	Worthington and Ford, 2009
Flood Wave Coefficient	k_s	0	0.6	0	0.5	-	Jain, 2001
Conduit Friction Factor	f_c	0.01	0.1	0.01	0.1	-	Moody, 1944
Swallet Friction Factor	f_s	0.01	0.5	0.01	0.4	-	Assumed Bound
Swallet Tortuosity	τ_s	1.3	2.5	1.3	2.2	m/m	Assumed Bound
Local Curvature Weighting Factor	α_{LC}	0.01	1	0.01	0.9	-	Assumed Bound
Fracture Lateral Distance Adjustment	dx_f	0.01	1	0.01	1	-	Assumed Bound
Matrix Lateral Distance Adjustment	dx_m	0.01	1	0.5	1	-	Assumed Bound

Table 10. SWAT Parameter Sets used in Cane Run Watershed and Performance of Set in the Upper South Elkhorn Watershed

Groundwater-related parameters are not included in this table, because they have are negated in the stream and groundwater model for the Cane Run Watershed

SWAT Run	SURLAG	CH_N2	CN2	EPCO	ESCO	SOL_AWC	OV_N	R2
1	1.590	0.171	-0.117	0.146	0.974	0.101	0.036	0.65
2	1.233	0.183	0.006	0.101	0.976	0.106	0.122	0.62
3	0.583	0.185	-0.095	0.115	0.949	0.103	0.113	0.66
4	0.597	0.158	-0.106	0.094	0.953	0.141	0.085	0.60
5	1.897	0.196	-0.095	0.143	0.916	0.146	0.021	0.60
6	1.660	0.167	0.001	0.167	0.983	0.108	0.071	0.61
7	1.110	0.208	0.026	0.172	0.970	0.149	0.016	0.65
8	1.936	0.218	-0.100	0.128	0.907	0.139	0.028	0.62
9	1.444	0.174	-0.117	0.132	0.991	0.134	0.002	0.62
10	1.036	0.213	-0.056	0.162	0.991	0.142	-0.018	0.63
11	0.510	0.223	-0.040	0.095	0.985	0.117	0.051	0.61
12	1.603	0.225	-0.013	0.164	0.901	0.146	0.098	0.61
13	1.488	0.246	0.010	0.182	0.939	0.131	0.121	0.65
14	1.788	0.221	-0.118	0.131	0.946	0.117	0.000	0.60
15	1.080	0.240	0.013	0.186	0.915	0.140	0.100	0.62
16	1.860	0.215	-0.082	0.194	0.984	0.109	0.048	0.63
17	1.770	0.237	0.028	0.149	0.971	0.119	0.118	0.65
18	1.903	0.193	-0.104	0.099	0.931	0.122	0.129	0.61
19	1.720	0.238	-0.059	0.086	0.963	0.134	0.082	0.61
20	0.996	0.212	-0.017	0.159	0.998	0.118	0.016	0.62
21	0.891	0.233	0.003	0.101	0.976	0.088	0.096	0.69
22	1.165	0.226	-0.083	0.096	0.918	0.083	0.051	0.68
23	0.505	0.273	-0.050	0.095	0.985	0.104	0.058	0.68
24	1.187	0.271	-0.137	0.131	0.946	0.103	0.031	0.68
25	0.724	0.261	-0.059	0.185	0.916	0.095	0.021	0.70

Table 11. Comparison between Upper South Elkhorn and Cane Run Creek Watersheds

	Cane Run	Upper South Elkhorn
Watershed Size	60.5 km ²	60.8 km ²
Soil		
Maury	85.9	90.3
Lowell	14.1	0
McAfee	0	9.7
Land Use		
Agriculture	9.6	3.3
Forest	0	13.5
Hay	48.9	35
Urban	38.7	47.7
Other	2.8	0.5
Slope		
0%-3%	41.7	27.8
3%-6%	47.4	36.9
6%+	10.9	35.3

Table 12. Initial and Final SWAT Parameter Selection and Parameter Ranges

SWAT parameters that are “Replaced”, the given value becomes the parameter value.
 SWAT parameters that are “Relative”, the default parameter is adjusted by the given value as a percentage

Parameter	Relative or Replaced	Initial Range		Final Range	
		Min Value	Max Value	Min Value	Max Value
ALPHA_BF.gw	Replace	0.2	0.7	0.55	0.9
GW_DELAY.gw	Replace	1	35	0	5
SURLAG.bsn	Replace	1	3	0.5	1.3
CH_N2.rte	Replace	0.05	0.2	0.15	0.3
CN2.mgt	Relative	-0.1	0.1	-0.14	0.03
EPCO.bsn	Replace	0.1	0.3	0.08	0.2
ESCO.bsn	Replace	0.9	1	0.9	1
SOL_AWC().sol	Replace	0.1	0.15	0.08	0.15
OV_N.hru	Relative	-0.1	0.1	0.02	0.1
GW_REVAP.gw	Replace	0.01	0.05	0.025	0.065
GWQMN.gw	Replace	0	100	30	90
REVAPMN.gw	Replace	300	720	430	560
RCHRG_DP.gw	Replace	0	0.1	0.08	0.17

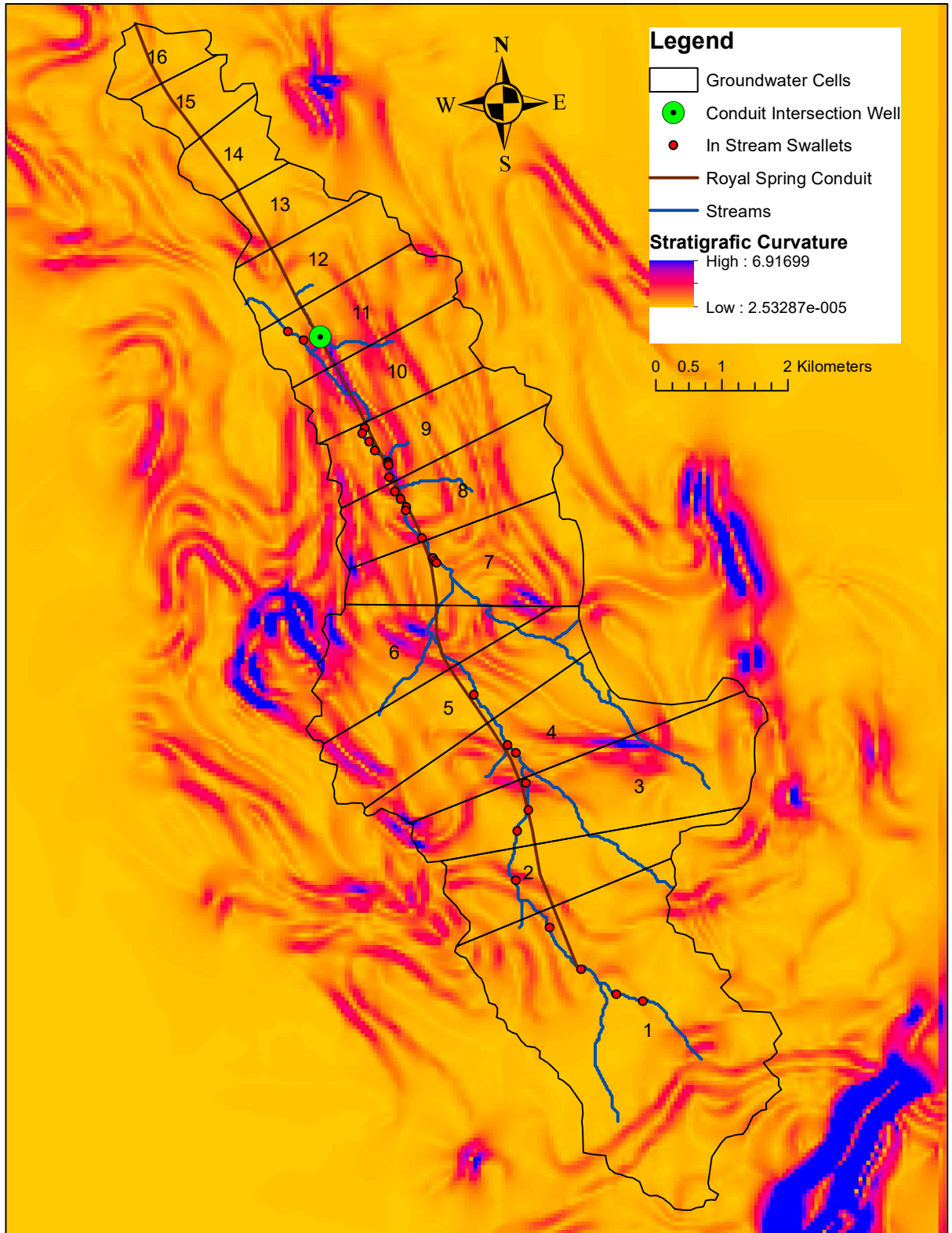


Figure 9. Stratigraphic Curvature

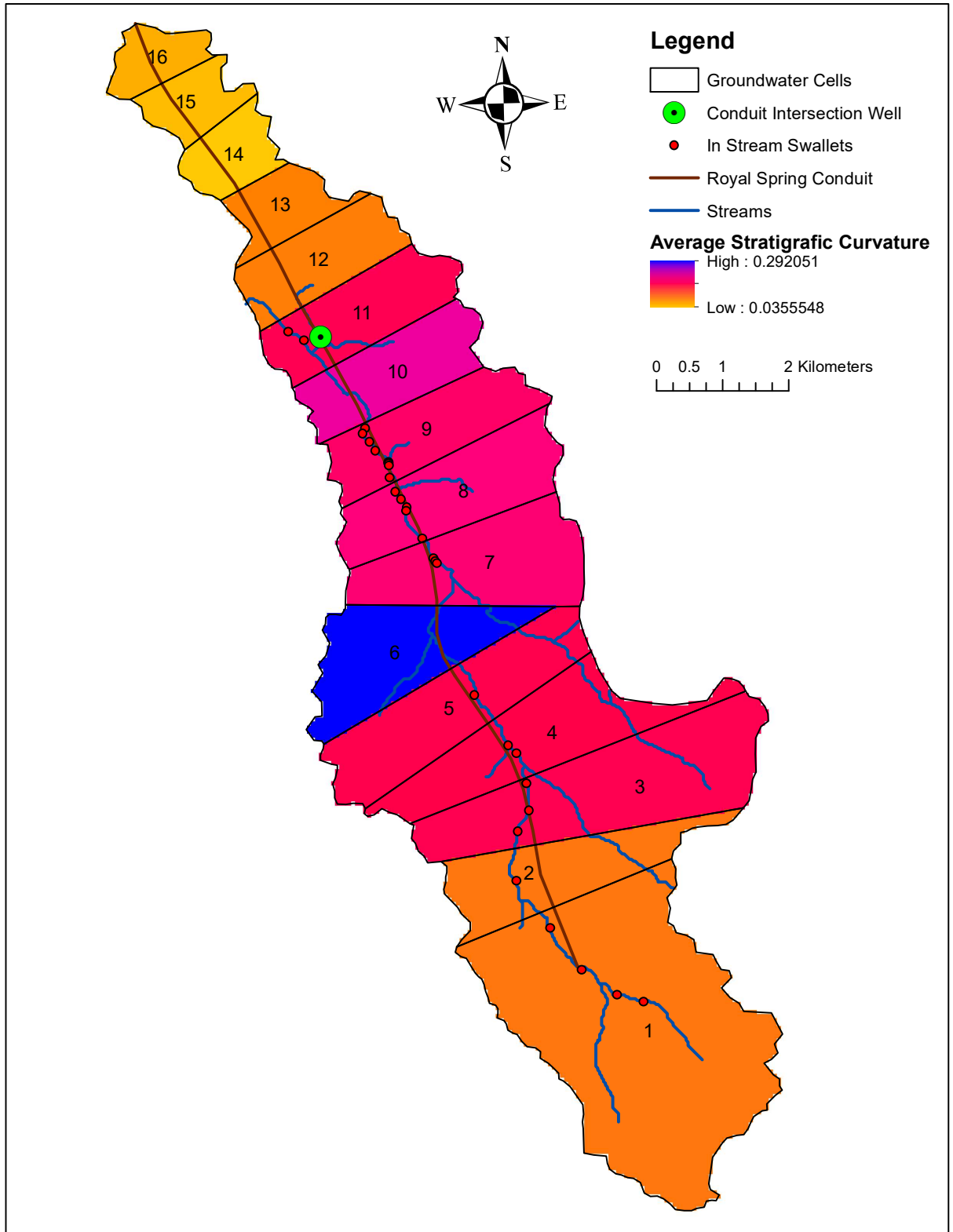


Figure 10. Averaged Stratigraphic Curvature

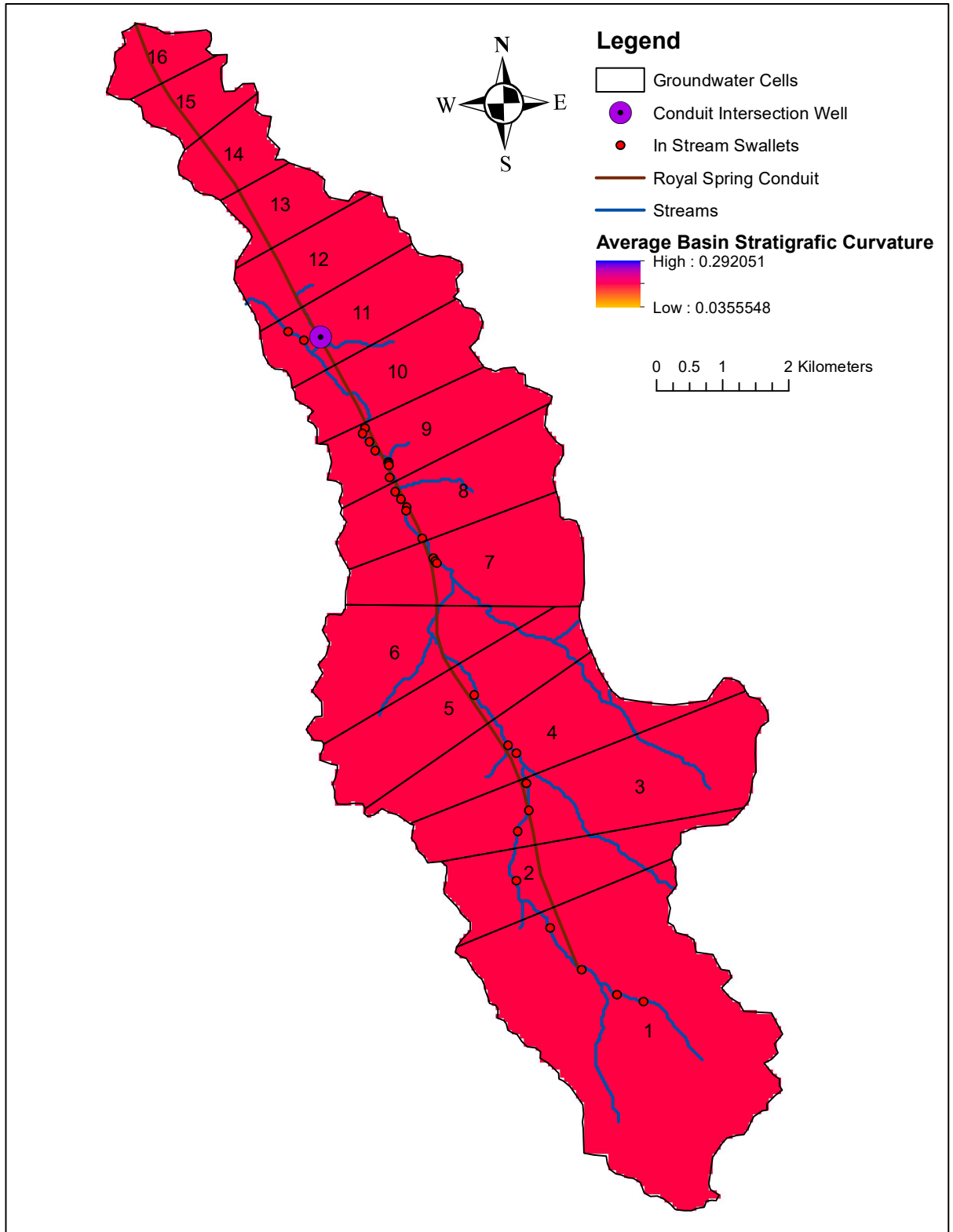


Figure 11. Average Stratigraphic Curvature over All Groundwater Cells

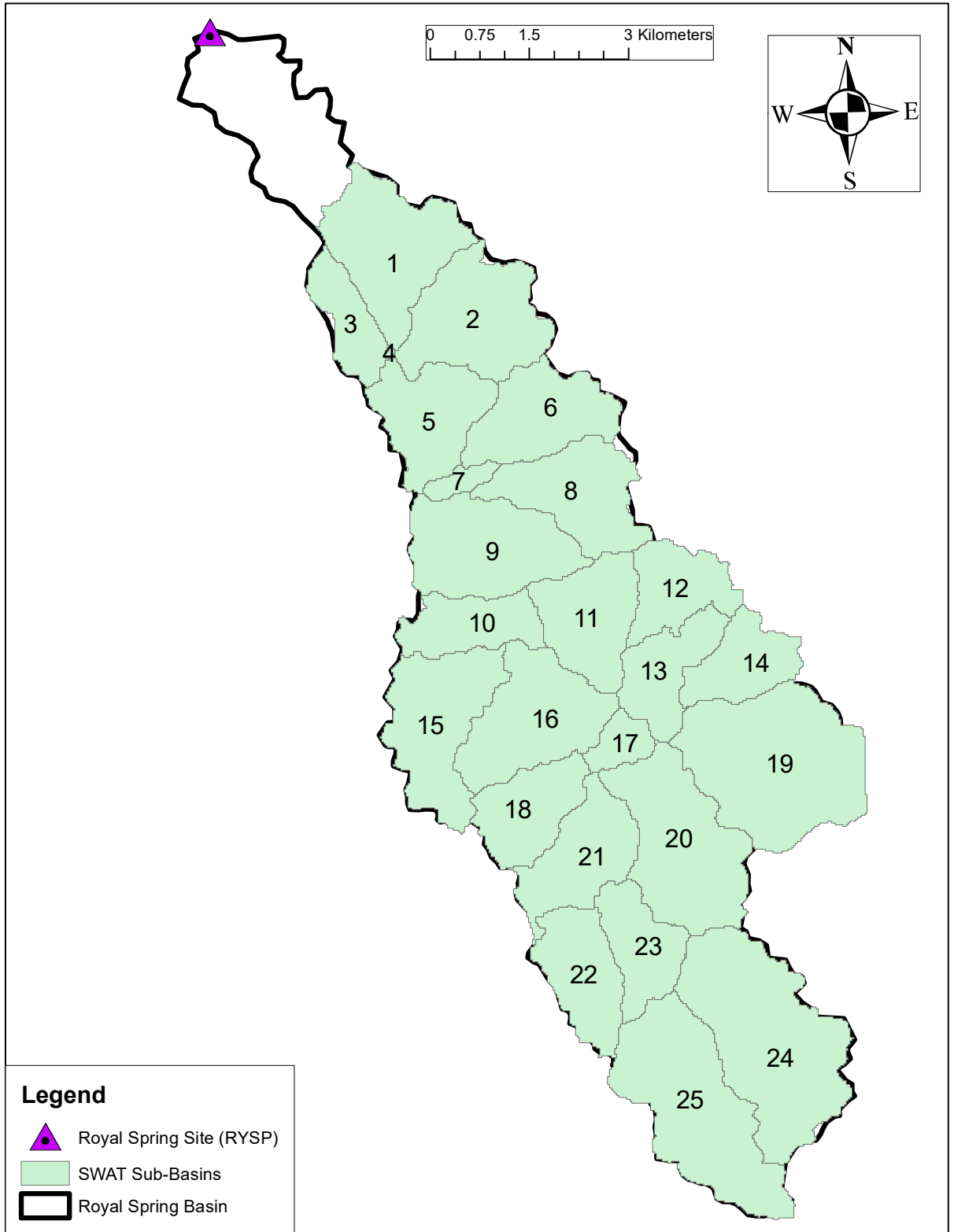


Figure 12. SWAT Spatial Discretization

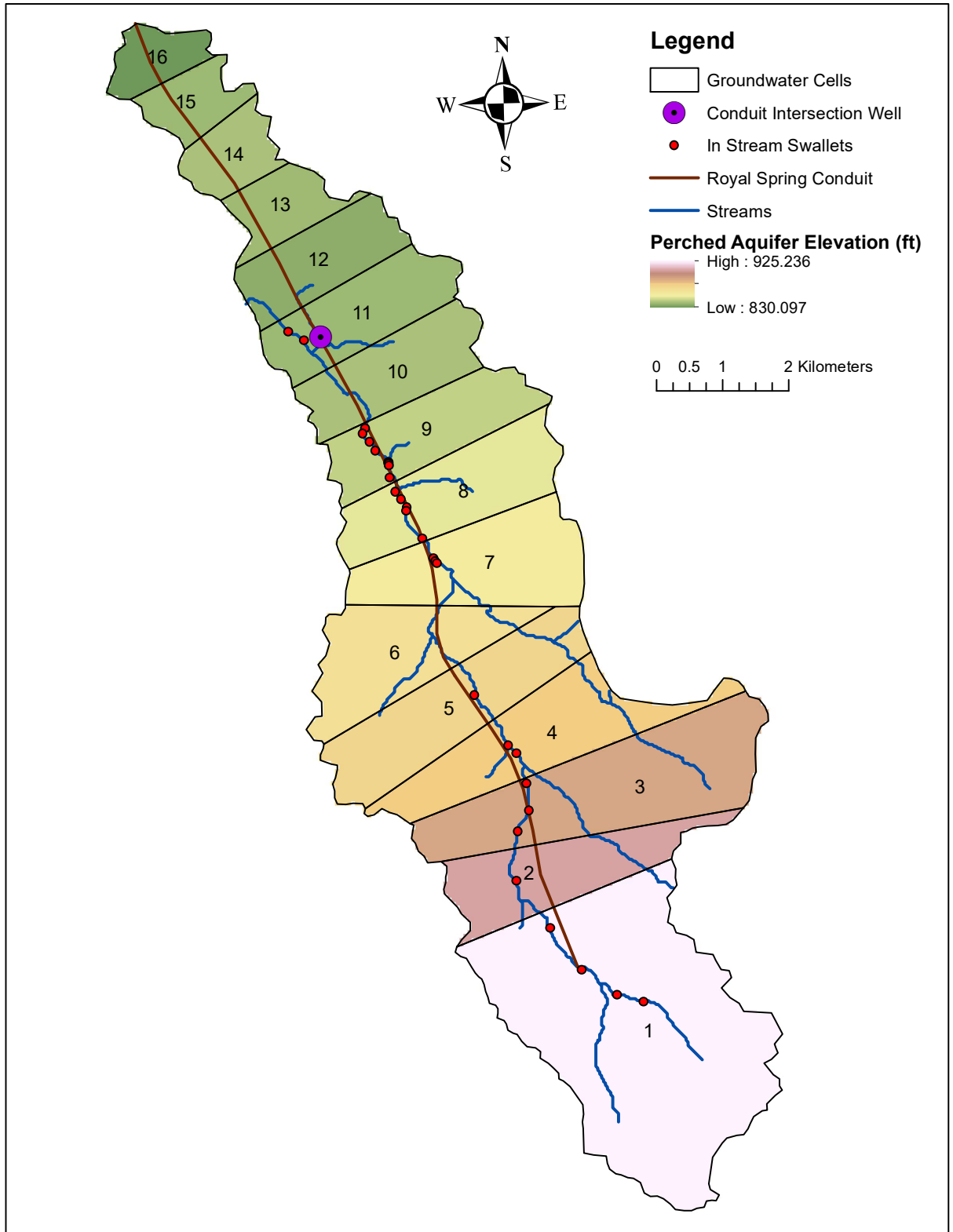


Figure 13. Averaged Cane Run Bed Elevations

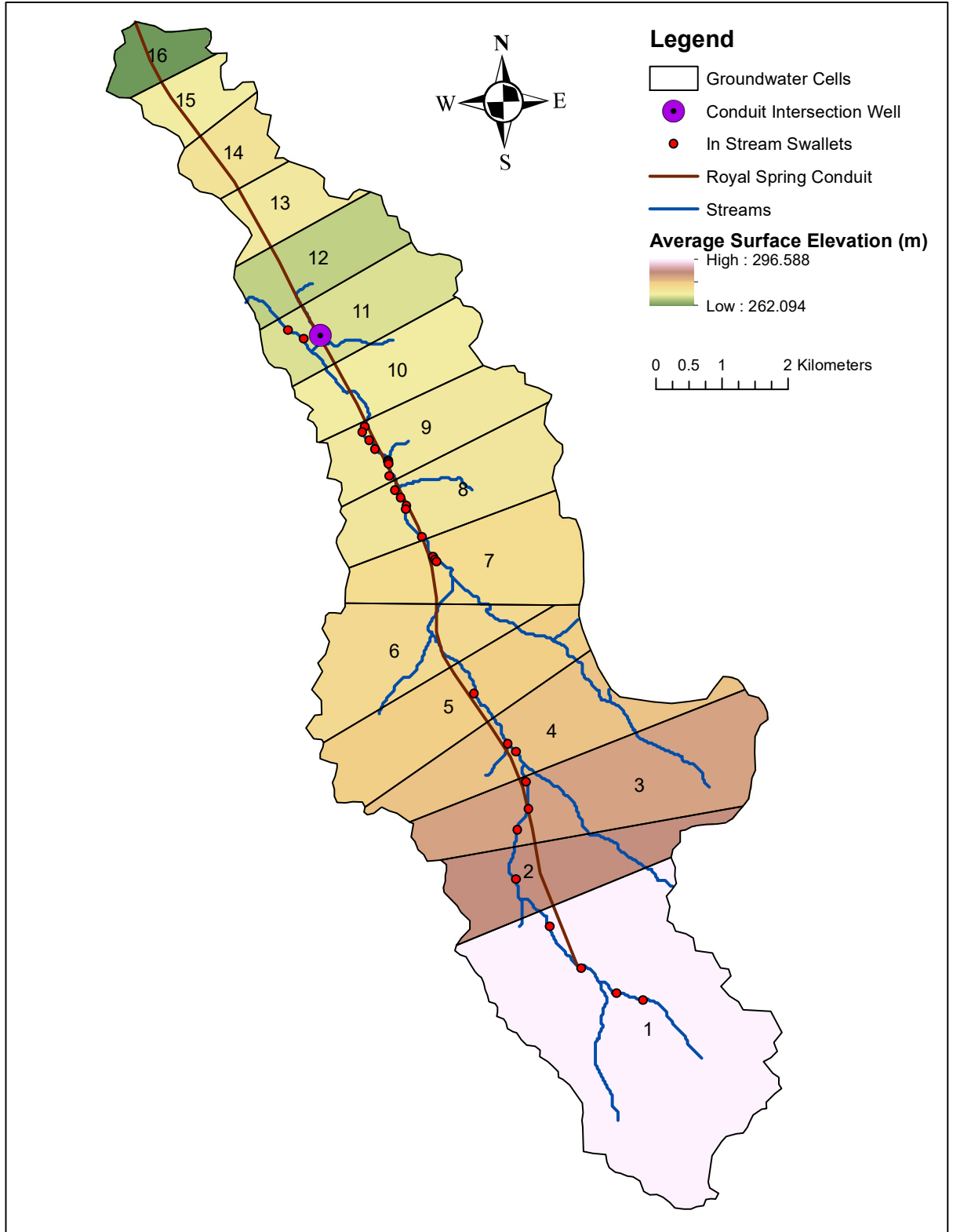


Figure 14. Average Surface Elevations

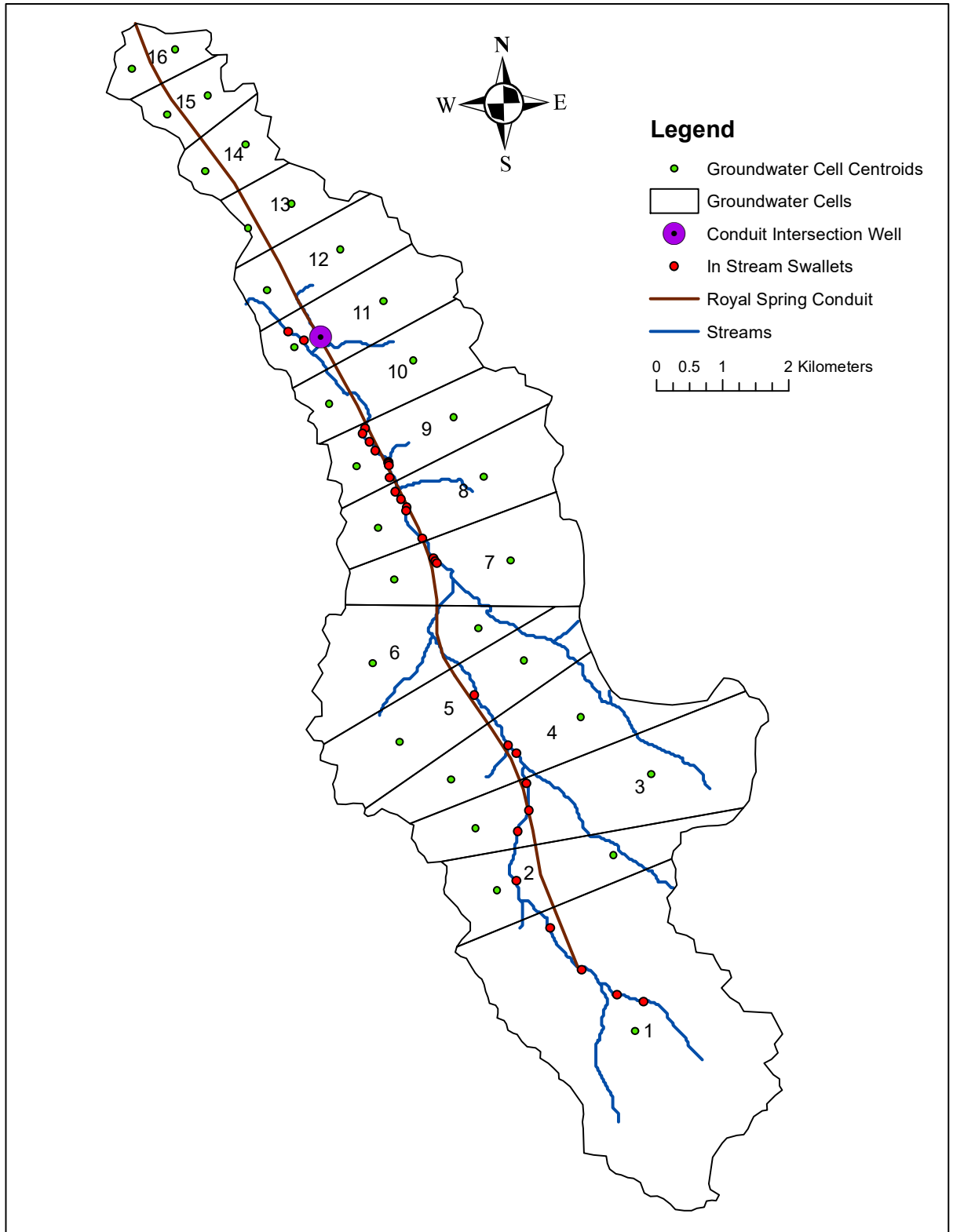


Figure 15. Centroids of Groundwater Cells

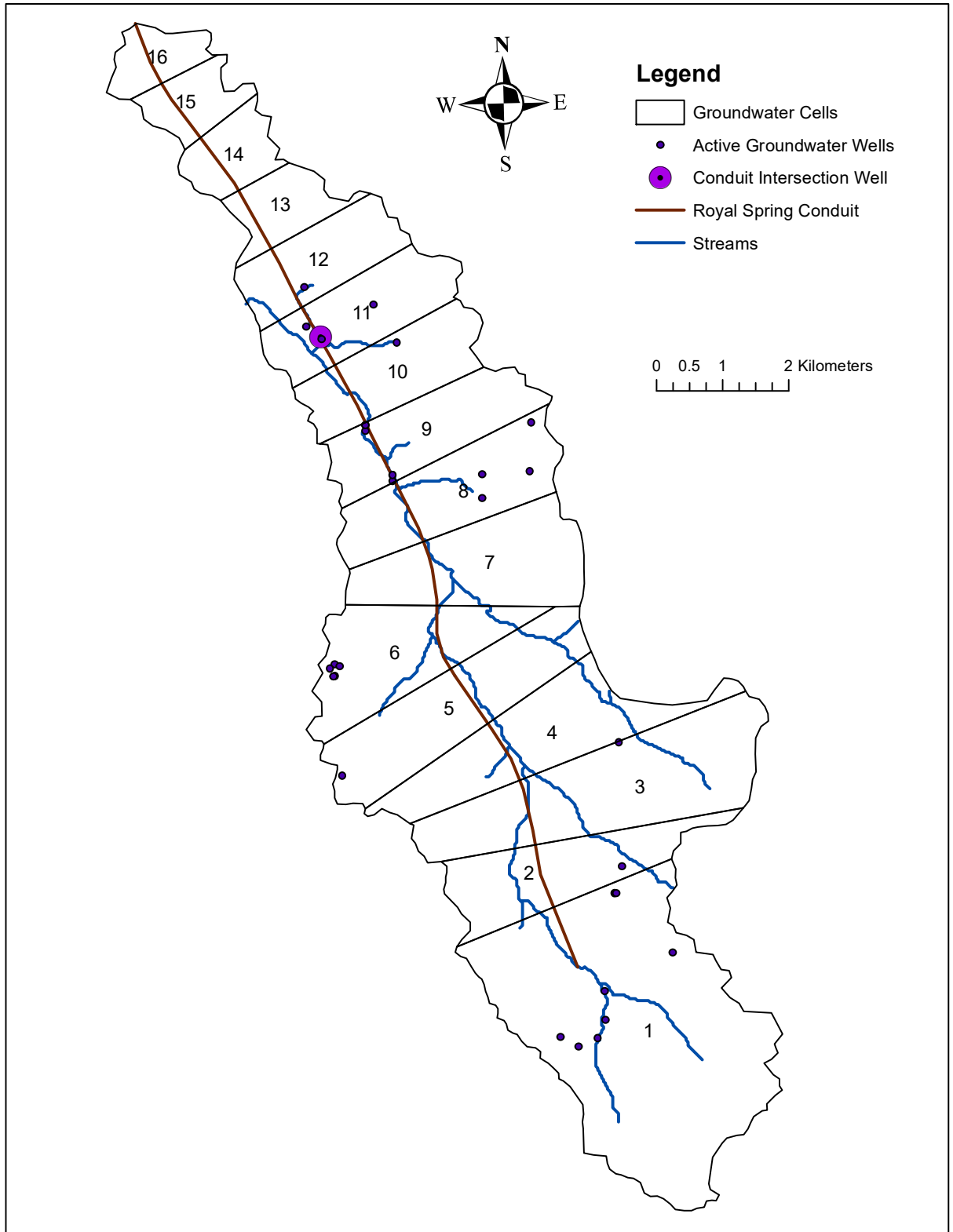


Figure 16. Active Groundwater Wells

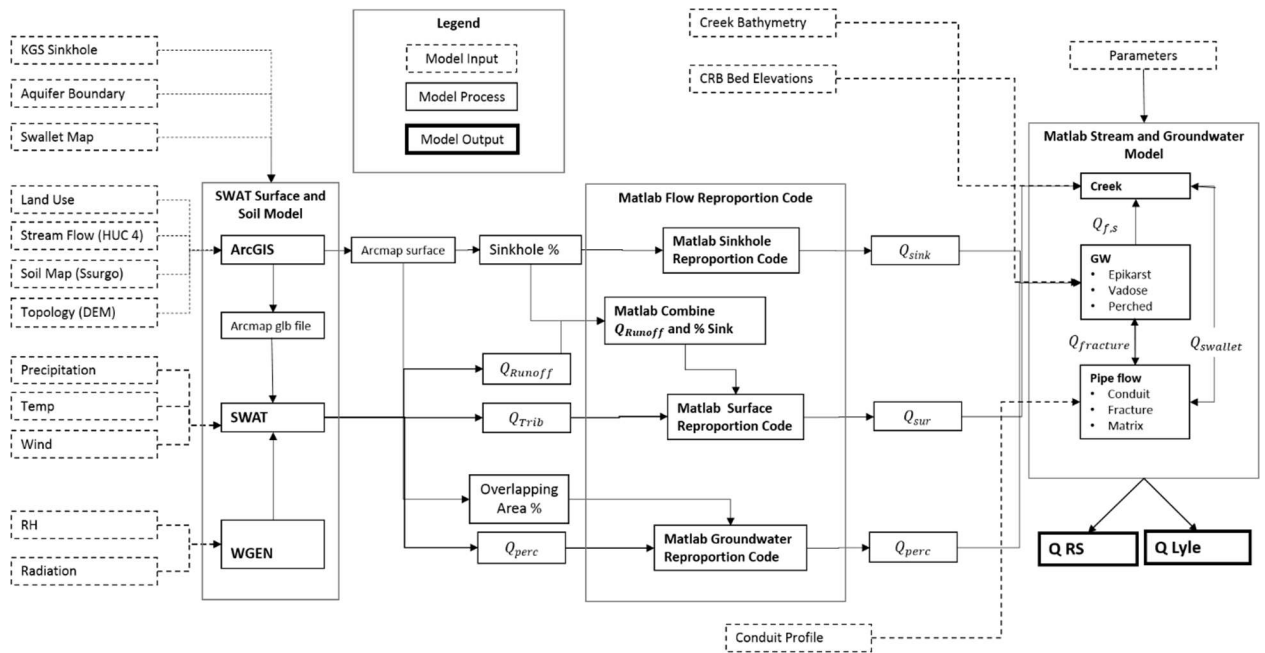


Figure 17. Model Workflow Schematic

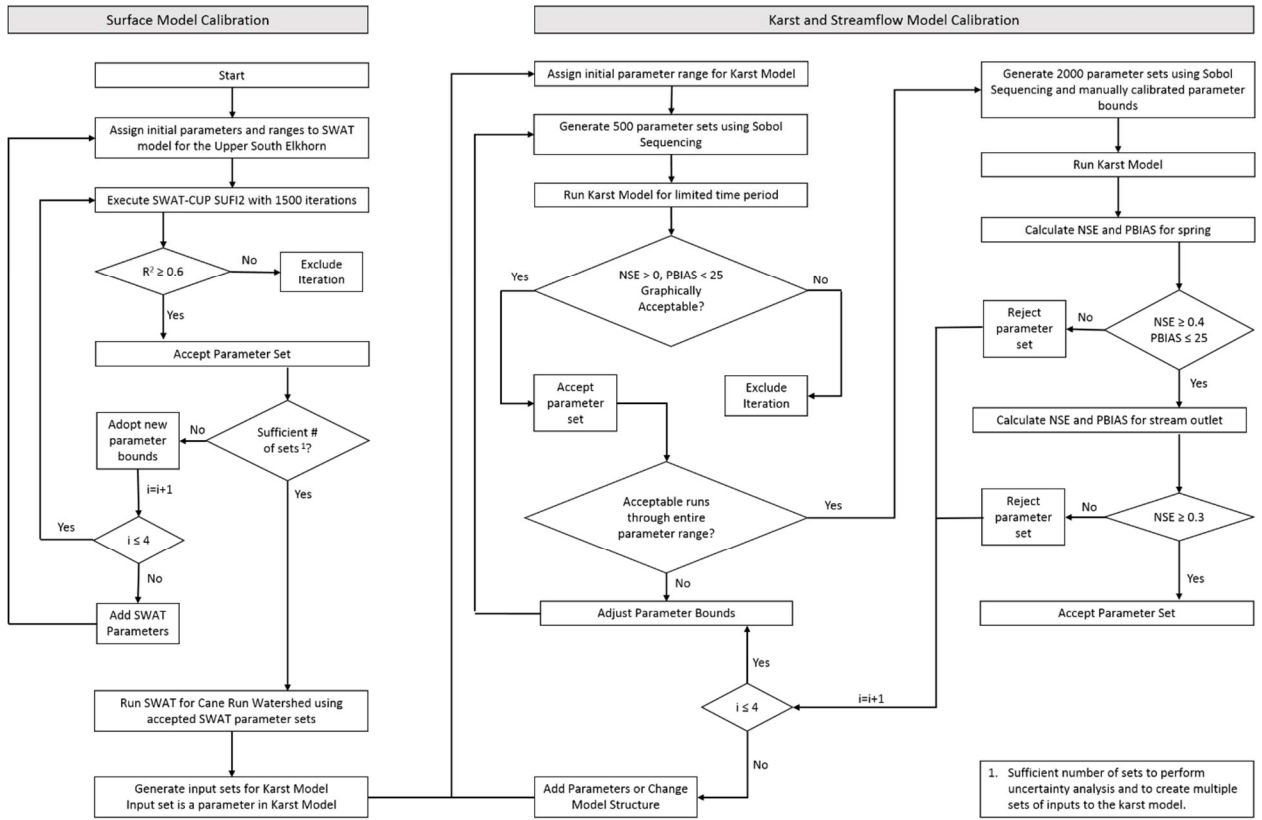


Figure 18. Model Calibration Flow Diagram

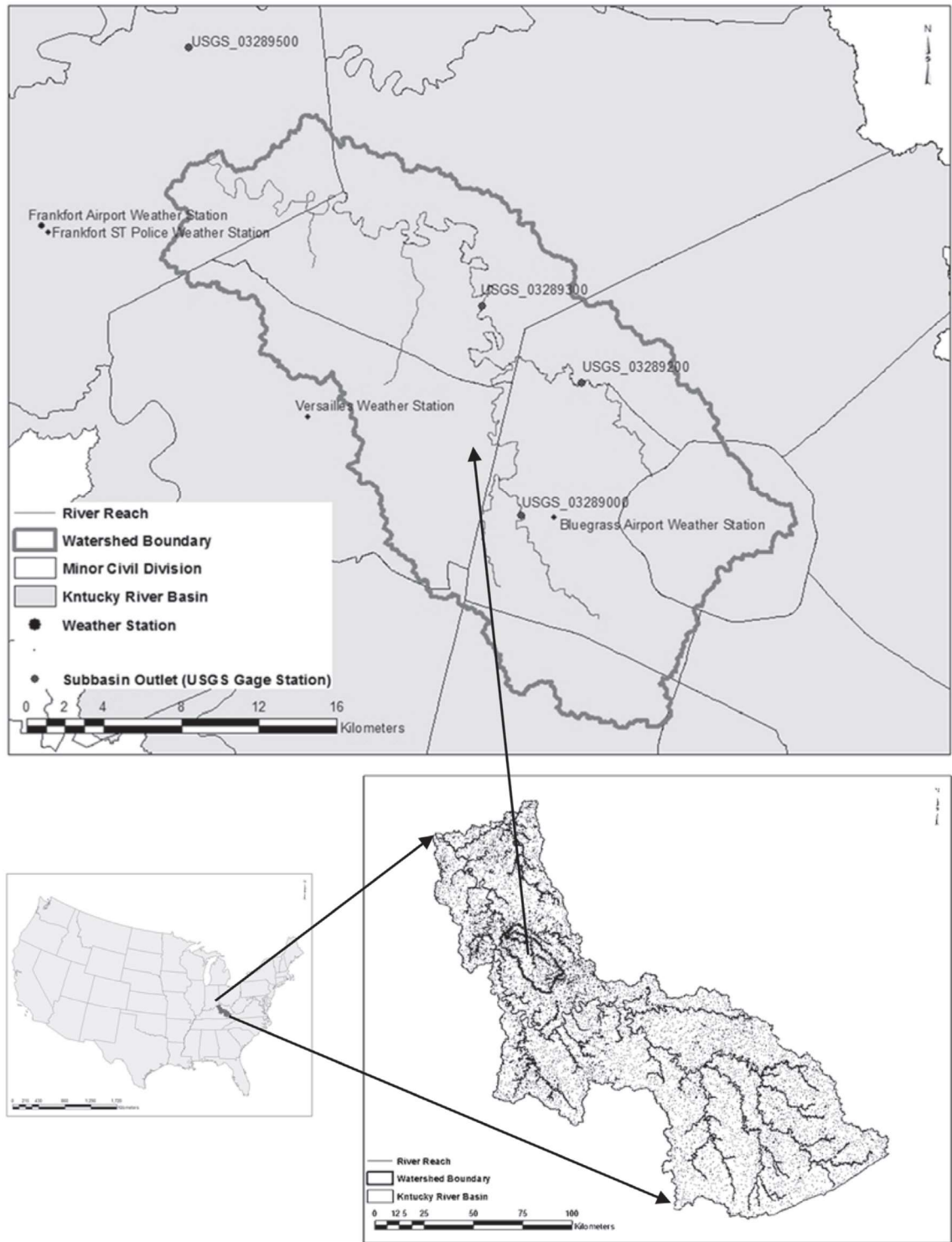


Figure 19. Map of South Elkhorn Watershed. From Al Aamery et al. (2016).

Chapter 5 Results

5.1) Model Evaluation Results

5.1.1) Calibration and Validation of Swat Model

The calibration of SWAT model was carried out in the Upper South Elkhorn watershed using a specific parameter set with physically meaningful ranges. The SWAT parameter selection used for model calibration was based on those most used in literature for SWAT calibration (Arnold et al., 2012, Al Aamery et al., 2016). The initial parameter ranges were chosen based on the physical meaning of the parameters as explained by Neitsch et al. (2011) and based on parameter values from a SWAT model used previously in the same watershed (Al Aamery et al., 2016). The SWAT parameters that were used and their initial values are shown in Table 12.

After the parameter selection and initial ranges were chosen, the SUFI2 optimization algorithm was executed using SWAT-CUP software (Abbaspour et al., 2007) with the initial parameter ranges for 1000 model runs. Parameter ranges were adjusted depending on the new ranges suggested by the algorithm and the physical meaning of the parameters, and the SUFI2 algorithm was executed again for 1000 model runs with the new parameter range. The parameter ranges were changed twice, because the first two executions had an insufficiently large solution space. Model runs were considered acceptable when the objective function R^2 was higher than 0.6. The first execution only produced 4 acceptable runs, and the second produced 51 acceptable runs. The final parameter ranges, shown in Table 12, produced 405 acceptable model runs. Parameter ranges from 25 of the 405 accepted model runs were selected for use in the SWAT model

of the cane Run watershed. The performance of the SWAT model was good when compared to literature. Objective function values for our hourly model were comparable to objective function values for daily models with good performance (Gassman et al., 2007).

The parameter values, as well as the performance of the parameter set measured by the R^2 value, that were used in the SWAT model of the Cane Run watershed are shown in Table 10. Out of the 13 SWAT parameters used in the Upper South Elkhorn Watershed, 6 were related to groundwater and baseflow calculations. When the SWAT model is applied to the Cane Run Watershed, only the seven parameters that are not involved in groundwater and baseflow calculations are used. This is because groundwater and baseflow calculations in the SWAT model are negated by setting the value of the deep aquifer recharge coefficient (RCHRG_DP) to 1. This adjustment is necessary for the SWAT model to be applicable in the karst watershed.

5.1.2) Calibration and Validation of Stream and Groundwater Model

The karst model was parameterized using 16 parameters. Table 9 shows the initial parameter ranges and the literature sources used to determine the initial ranges. Similarly to the SWAT model calibration, the SUFI2 optimization algorithm was used to adjust parameter ranges, however, Sobol sequencing was used to generate the parameter values for each run. Initially, sets of 500 model runs over a short time period were used to refine the parameter ranges. The parameter ranges were adjusted three times. The final values of the parameter ranges are shown in Table 9.

Adjustments made to the initial and subsequent stream and groundwater model parameter ranges suggested by the SUFI2 optimization algorithm generally agreed with our visual inspection of the distribution of accepted results across the parameter ranges. The SUFI2 optimization algorithm suggested reduction of parameter ranges where visual inspection showed that the parameter ranges were larger than the range of accepted parameter values. The SUFI2 optimization algorithm is was also able to recommend expanding parameter values, where our visual inspection was not.

After the final parameter ranges were determined, 2000 model runs were performed, using Sobol sequencing to determine the parameter values for each run. Model runs were performed from Dec 1, 2010 to Dec 31, 2017, with the first month used as a model spin-up, the next 5 years as the calibration period, and the final 2 years as a validation period. Model runs with objective function values of $NSE > 0.4$, $PBIAS < 25$ for spring discharge, and $NSE > 0.3$ for streamflow were considered acceptable. Out of the 2000 model runs, 5 runs were considered acceptable. The parameter values for the best model run are shown in Table 13, and the values of the objective functions are shown in Table 14. The spring discharge hydrograph for this run is shown in Figure 20.

When compared to literature, the performance of our model is satisfactory to good. Objective function values from our hourly model are comparable to objective function values of daily streamflow models considered acceptable (Gassman et al., 2007). The objective functions for spring discharge for our best model run surpass the satisfactory values subjected by Moriasi et al. (2007), for models with a monthly time-step. Models have significantly reduced performance measures when using a shorter-duration timestep (Gassman et al., 2007; Moriasi et al., 2007)., suggesting the satisfactory objective function

values should be reduced for our hourly model. Additionally, hourly results for springflow were aggregated into daily average springflow values. Observed hourly spring discharge was also averaged for each day and the performance of the daily aggregated model results were calculated. The performance metrics for daily results were improved, as shown in Table 14. This is consistent with results from Gassman et al. (2007), showing improved model performance when results are aggregated for larger time-steps. Given these facts, the performance of our model should be considered good.

Simulated stream and spring hydrographs were compared to measured values. Figure 20 shows the simulated spring hydrograph and observed spring hydrograph for the full simulation period. Generally, observed and simulated spring hydrograph peaks on or near the same time step, however, the simulation struggles to capture the peak flow or hydrologic events. Individual hydrologic events were also examined. Figure 21 shows a comparison between simulated and observed spring hydrographs for two hydrologic events. Figure 22 shows a comparison between simulated and observed stream hydrographs for two hydrologic events. Simulated spring hydrograph peaks roughly occur at the same time as observed hydrograph peaks, within 0 to 3 hours. Simulated stream hydrograph peaks generally precede observed stream hydrograph peaks by about 6 hours. The discrepancy in timing of simulated and observed stream hydrograph peaks may be attributed to the distance between the watershed and the precipitation and weather gages used to provide input data to the model, or the SWAT model used for surface runoff and soil water simulation being calibrated for a different watershed. Figure 21 also elucidates a potential limitation in the model. The rising limb of the spring hydrograph generally occurs during the first hour of a day. This is potentially due to the soil water percolation

input to the epikarst was calculated for a daily timestep in the SWAT model. SWAT was only able to provide hourly results for surface flows.

5.1.3) Sensitivity and Uncertainty Analysis of SWAT Model

Sensitivity of SWAT model parameters was determined using a multiple regression model, and a t-test for each parameter. Parameters with a p-value less than 0.5 are considered sensitive. The results of the sensitivity analysis for the SWAT model show that 6 out of the 13 SWAT model parameters used in the calibration procedure were sensitive parameters. These included the baseflow alpha factor, deep aquifer recharge coefficient, groundwater delay, Curve Number, Manning's roughness coefficient of the channels, and the soil available water capacity. However, only three of these parameters did not involve groundwater or baseflow and do not affect the surface runoff, lateral flow, and soil percolation values that are used as inputs to the stream and groundwater model. The three parameters that influence inputs to the stream and groundwater model were the Curve Number, Manning's roughness coefficient of the channels, and the soil available water capacity. These three parameters were also sensitive in a SWAT model for the South Elkhorn watershed from a previous study (Al Aamery et al., 2016). The results of the sensitivity analysis for the SWAT model are shown in Table 15.

5.1.4) Sensitivity and Uncertainty Analysis of Stream and Groundwater Model

The sensitivity of model parameters was determined using a multiple regression model and a t-test. Parameters with a p-value less than 0.05 were considered sensitive.

Results from the sensitivity analysis showed that the performance of the simulated spring discharge in the karst model was sensitive to 8 of the 16 karst model parameters. These conduit friction factor, saturated hydraulic conductivity, fracture density, fracture aperture, matrix porosity, pump rate, epikarst threshold height, and Manning's roughness coefficient. These results are shown in Table 16. The sensitive parameters to springflow are logical. The conduit friction factor is important in conduit flow equations that control spring discharge. The sensitivity of the epikarst threshold height may elucidate the importance of the timing of the epikarst to fracture flow activation during hydrologic events. The saturated hydraulic conductivity is an important parameter in the timing and flowrates of several karst pathways. The pump rate could potentially affect the head driving matrix and fracture flow into the conduit. The sensitivity of the fracture density and fracture aperture elucidates that the fracture-flow pathway may be an important component of spring flow. The sensitivity of the matrix porosity may highlight the effect of aquifer storage on spring hydrograph behavior. The sensitivity of the Manning's roughness coefficient on spring discharge may highlight how spring discharge is in some ways correlated to streamflow, which could influence subsurface pressure gradients via swallets.

Sensitivity analysis results also showed that the performance of simulated streamflow was sensitive to 5 of the 16 model parameters. These included: Manning's roughness coefficient, the epikarst threshold height, the fracture aperture, fracture density, and the saturated hydraulic conductivity. These results are shown in Table 17. The sensitive parameters of Manning's roughness coefficient is not surprising. Manning's roughness coefficient controls the calculations for stream height and flowrate. The sensitivity of the epikarst threshold height, the fracture aperture, fracture density, and the saturated hydraulic

conductivity was not expected, and suggests that swallet reversals and fracture flow into the stream network could be important pathways in the system.

In total 8 of the 16 parameters were sensitive, Manning's roughness coefficient, the epikarst threshold height, the fracture aperture, fracture density, and the saturated hydraulic conductivity sensitive for both springflow and streamflow. This suggests that both subsurface and surface process are important for both springflow and streamflow.

The average springflow ± 1 standard deviation of all acceptable model runs is shown in Figure 23a. This helps illustrate the uncertainty in the model. The average standard deviation in the model simulation was 0.032 (cms). The uncertainty of the model as measured by the thickness of the 95 PPU of accepted model runs is shown in Figure 23b. The average thickness of the 95 PPU was 0.28 (cms). The observed springflow was contained by the 95 PPU during 28% of the model timesteps. This value is lower than what is recommended by Abbaspour (2007) for models with high quality observation data, however it is within acceptable values for data of a lower quality. The observed spring discharge at the Royal Springs Gage (USGS 03288110) is downstream from where abstractions made by the Georgetown Municipal Water and Wastewater Service are made. Spring discharge data was adjusted for these abstractions; however, some error still exists. Additionally, the recommendations made by Abbaspour (2007) are for models with a daily timestep, and as previously mentioned, recommended levels should be lower for models with an hourly time-step.

5.2) Pathways during Hydrologic Events and Recession Periods

Modelled spring flow for a well performing model run is shown in Figure 20. This figure also includes a two-month window with subsequent plots detailing the total fracture and swallet flowrates exchanges with the phreatic conduit (Figure 24a), the total contribution to spring discharge from karst pathways (Figure 24b), and the total contribution to stream flow from pathways (Figure 24c). As can be seen in the two-month windows, fracture flow dominates the spring, fractures are either in a state of recharge by the epikarst, perched aquifer, or saturated matrix, or they are draining stored water to the spring. The surface water outlet is dominated by runoff. Other pathways are swallet flow to the spring, swallet reversal (i.e., from the conduit to the surface stream), sinkholes and perched aquifers recharging the fracture network, and hillside springs into the stream.

Specific hydrologic events are evaluated more closely for hydrologic events, including moderate and extreme events. Hydrologic events with over 51mm (approximately 2 inches) were considered extreme events. The selection of extreme events used in the evaluation represented all four seasons and several different years. Karst pathway contributions to spring discharge during extreme hydrologic events are shown in Figure 25b, and during moderate hydrologic events in Figure 26b. Additionally, total fracture and swallet flow exchanged with the phreatic conduit for extreme hydrologic events are depicted in Figures 25a, and for moderate hydrologic events in Figure 26b.

During both extreme and moderate hydrologic events, fracture flow to the spring dominates the hydrograph. Initially concentrated water from the epikarst to the fractures drives the rising limb of the hydrograph. The end of concentrated recharge from the epikarst to the fractures coincides with the peak flow and spring hydrograph recession which is driven by drained storage water in from the fractures, recharged during the event

from the epikarst. During all five extreme events investigated, swallet reversals occur, with the peak reversal coinciding with the peak fracture flow to the conduit. Swallets only contribute flow to the spring during the hydrograph recession. Swallets acted as overflow springs during the peak of each extreme event. During moderate events, swallet flow did also reverse and acted as overflow springs and fracture flow still dominated the spring hydrograph with concentrated recharge to the fractures from the epikarst driving the rising limb of the hydrograph, peak flow occurring at the end of the epikarst contribution, and stored water in the fractures, attributed to epikarst recharge, driving the spring recession. Swallets contributed some flow to the spring hydrograph during the recession of moderate hydrologic events.

During both extreme and moderate hydrologic events, surface runoff and lateral flow dominated stream hydrographs. Hillside springs and swallet reversals also contributed to stream hydrographs during both extreme and moderate hydrologic events. Surface runoff drove the rising limb and peak of the stream hydrograph. Hillside springs and swallet reversals drove more of the flow during the hydrograph recession. Contributions from hillside springs and swallet reversals to streamflow were more pronounced in extreme events than in moderate hydrologic events.

Springflow pathways during recession periods were examined. Figure 24b shows a two-month window with several recession periods. During these recessions, fracture pathways are dominant. However, unlike hydrologic events where epikarst recharge to the fracture network and drainage of stored water from the event dominate, the perched aquifer and matrix water also contribute to fracture flow. During these recessions stored fracture water is the dominant fracture flow pathway for the first 5-10 days of the recession. Then

contributions are equal to or greater than the epikarst recharge to the fractures and draining fracture storage. Stored fracture water is the dominate fracture flow pathway for the first 5-10 days of the recession.

5.3) Annual Averages of Karst Pathways

Calculations were performed for annual estimates. The contribution of karst pathways identified in Figure 2 to total spring flow and surface stream flow were investigated for model runs with acceptable performance criteria.

Pathways contributing to total spring flow will enter the conduit network through either a swallet, the fracture network or from the saturated bedrock matrix. The total percent of spring discharge from swallet, fracture, and matrix pathways are displayed in Table 18. Fracture pathways dominate the spring hydrograph with matrix pathways contributing virtually zero flow to the spring. Several pathways through the fracture network contribute to spring discharge including concentrated recharge from the epikarst, recharge from sinkholes, diffuse recharge from the perched aquifer, and flow from the saturated matrix. Additionally, the fracture network has the ability to store water and release it after flow into the fracture network from the various sources has ceased and can contribute to the spring hydrograph. The total percent of spring discharge resulting from each fracture pathway is shown in Table 18, with the epikarst pathway, perched aquifer pathway, and drained fracture storage dominating. The pathways that recharge the storage volume in the fracture network include the conduit, matrix, epikarst, sinkholes, and perched

aquifer. The total percentage of fracture storage volume gained from each pathway is depicted in Table 19. The epikarst dominates recharge of fracture storage.

Pathways contributing to the total surface streamflow include surface runoff and lateral flow, swallet reversals, and fracture flow from hillside springs. The total percent of streamflow from each pathway is shown in Table 18. Surface runoff and lateral flow constitute the majority of streamflow. The pathway contributions to total streamflow during extreme hydrologic events are shown in Figure 25c and during moderate hydrologic events in Figure 26c. During extreme hydrologic events, surface runoff and lateral flow drives the rising limb and peak of the hydrograph. Fracture flow from hillside springs and swallet reversals increases during the recession and in some secondary hydrograph peaks. During moderate hydrologic events surface runoff and lateral flow is the only pathway contributing to streamflow.

Annually, water will leave the basin via three pathways, streamflow, spring discharge, and pumping. The total percentage of basin outflow from each outlet is shown in Table 18. The majority of flow exits the basin through the spring.

5.4) Residence Time and Storage Estimates

Residence time distributions were calculated for the model runs with acceptable performance criteria. The median residence time in the swallets, conduit, fracture network, saturated bedrock matrix, epikarst, and the perched aquifer was calculated. The mean residence time in each karst feature calculated from acceptable model runs are displayed in Table 20. Swallets have the shortest mean residence time, on the order of minutes,

reflective of the small total volume and relatively high velocities. The saturated bedrock matrix had the highest mean residence time on the order 1 to 5 years, reflective of small fluxes between the matrix and other karst features. The mean of residence time of each karst feature during winter, spring, summer, and fall for acceptable model runs are displayed in Table 20. The largest difference in residence time in any season from the all-season mean was seen in the matrix, with a 1.3 times longer residence time during fall than the average across all seasons.

Storage volumes in the fracture network, saturated bedrock matrix, epikarst, and perched aquifer were calculated for model runs with acceptable performance criteria. The mean storage volume in each storage reservoir are displayed in Table 21. The saturated matrix had the highest mean storage volume, at an order of magnitude greater than the fracture network, perched aquifer, and the epikarst.

Table13. Karst Model Parameters Calibrated Values

Parameter Name	Symbol	Accepted Runs Ranges		Best Run	Units
		Min	Max		
Matrix Porosity	n_m	1.14×10^{-3}	5.25×10^{-3}	1.59×10^{-3}	%
Saturated Hydraulic Conductivity	K_s	1.84×10^{-9}	6.70×10^{-9}	1.84×10^{-9}	m s^{-1}
Epikarst Porosity	n_{ep}	0.043	0.262	0.111	%
Epikarst-Fracture Threshold Height	ep_{th}	0.011	0.137	0.030	m
Pump Rate	q_{pump}	9.42×10^{-5}	1.53×10^{-3}	9.42×10^{-5}	$\text{m}^3 \text{s}^{-1}$
SWAT Run	SWAT	12	25	12	-
Fracture Density	N	0.012	0.357	0.357	m^{-1}
Manning's n	n	0.099	0.192	0.011	$\text{m}^{1/6}$
Fracture Aperture	b	1.08×10^{-3}	0.24	1.08×10^{-3}	m
Flood Wave Coefficient	k_s	0.090	0.499	0.325	-
Conduit Friction Factor	f_c	0.046	0.091	0.046	-
Swallet Friction Factor	f_s	0.128	0.349	0.246	-
Swallet Tortuosity	τ_s	1.513	1.871	1.844	m/m
Local Curvature Weighting Factor	α_{LC}	0.024	0.201	0.112	-
Fracture Lateral Distance Adjustment	dx_f	0.032	0.699	0.699	-
Matrix Lateral Distance Adjustment	dx_m	0.566	0.886	0.683	-

Table 14. Best Model Run Performance

	Hourly	Daily
NSE Calibration	0.46	0.50
PBIAS Calibration	11.56	8.91
NSE Validation	0.37	0.40
PBIAS Validation	9.21	11.61
NSE Creek	0.50	0.66
PBIAS Creek	16.76	16.59

Table 15. Sensitivity Analysis Results for SWAT Parameters in Upper South Elkhorn

Parameter Name	t-Stat	P-Value
CN2.mgt	7.43	0.00
ALPHA_BF.gw	13.99	0.00
CH_N2.rte	-15.65	0.00
SOL_AWC(..).sol	-16.02	0.00
GW_DELAY.gw	-54.89	0.00
RCHRG_DP.gw	3.92	0.00
ESCO.bsn	1.70	0.09
SURLAG.bsn	1.58	0.11
OV_N.hru	0.88	0.38
REVAPMN.gw	-0.59	0.56
GW_REVAP.gw	0.41	0.68
EPCO.bsn	0.28	0.78
GWQMN.gw	0.12	0.90

Table 16. Sensitivity Analysis Results for Karst Parameters on Spring Discharge

Parameter	<i>t Stat</i>	<i>P-value</i>
f_c	34.65	0.00
K_s	-13.39	0.00
N	-13.07	0.00
b	-8.87	0.00
n_m	-7.13	0.00
q_{pump}	4.09	0.00
ep_{th}	-3.03	0.00
n	-2.62	0.01
n_{ep}	-1.71	0.09
τ_s	-1.11	0.27
dx_f	0.96	0.34
SWAT Run	-0.92	0.36
dx_m	0.53	0.60
α_{LC}	0.50	0.62
f_s	-0.29	0.77
k_s	0.27	0.78

Table 17. Sensitivity Analysis Results for Karst Parameters on Streamflow

Parameter	<i>t Stat</i>	<i>P-value</i>
b	8.72	0.00
N	7.43	0.00
n	5.61	0.00
K_s	-3.19	0.00
ep_{th}	-2.11	0.04
q_{pump}	1.89	0.06
f_s	1.64	0.10
α_{LC}	1.29	0.20
τ_s	1.21	0.22
f_c	-1.00	0.32
n_m	-0.48	0.63
dx_m	-0.31	0.75
SWAT Run	-0.19	0.85
n_{ep}	-0.10	0.92
dx_f	-0.06	0.95
k_s	-0.05	0.96

Table 18. Karst Pathways

Individual pathway contributions to spring discharge and streamflow are shown, as well as the contribution of spring discharge, stream outflow, and aquifer pumping on total basin outflow.

Pathway	Flow (cms)		Percentage		
	Mean	Stdev	Mean	Stdev	
Swallet	0.041	0.020	5.9%	2.9%	
Matrix	0.000	0.000	0.0%	0.0%	
Fracture Sources	Epikarst	0.227	0.053	32.7%	7.6%
	Sinkholes	0.004	0.001	0.6%	0.1%
	Perched Aquifer	0.188	0.111	27.1%	15.9%
	Matrix	0.059	0.075	8.4%	10.8%
	Total Drainable Storage	0.175	0.073	25.2%	10.5%
Fractures	0.654	0.020	94.0%	2.9%	
Total Spring Discharge	0.695	0.032	100%		
Runoff and Lateral Flow	0.212	0.024	46.8%	5.3%	
Hillside Springs (Fractures)	0.134	0.040	29.6%	8.8%	
Swallet Reversals	0.107	0.063	23.6%	13.9%	
Total Streamflow	0.452	0.038	100.0%		
Total Spring Discharge	0.695	0.032	60.0%	2.8%	
Total Streamflow	0.452	0.038	39.1%	3.3%	
Total Pumped Volume	0.011	0.008	0.9%	0.7%	
Total System Outflow	1.158	0.056	100.0%		

Table 19. Fracture Storage Sources

Individual pathway contributions to total fracture drainable storage are shown.

	Mean	Stdev
Conduit	0.0%	0.0%
Epikarst	96.3%	2.8%
Matrix	0.1%	0.2%
Perched Aquifer	2.6%	2.7%
Sinkholes	0.9%	0.1%

Table 20. Mean Residence Times for Karst Features

Note that time units are different for each feature.

Feature	Annual		Winter		Spring		Summer		Fall	
	Mean	Stdev	Mean	Stdev	Mean	Stdev	Mean	Stdev	Mean	Stdev
Swallet, min	20.6	8.6	24.6	11.7	20.6	9.0	16.0	5.8	23.3	6.8
Conduit, hrs	10.6	1.0	8.7	0.6	8.8	0.5	13.5	1.1	16.5	2.3
Fractures, days	3.7	2.6	3.5	2.3	3.6	2.5	3.9	3.0	3.8	3.0
Matrix, days	680	560	1591	1446	489	321	422	351	1066	992
Epikarst, hrs	23.0	14.2	24.3	14.9	24.1	14.8	20.7	13.1	19.6	12.2
Perched Aquifer, days	61.0	68.6	68.2	84.1	57.8	62.9	57.9	62.5	67.1	79.4

Table 21. Mean Storage Volume in Karst Aquifer Storage Reservoirs.

Values are in Cubic Meters.

Reservoir	Mean	Standard Deviation
Fractures	2.25×10^5	1.35×10^5
Matrix	1.02×10^6	4.026×10^5
Epikarst	3.75×10^5	4.24×10^5
Perched Aquifer	6.51×10^5	4.77×10^5

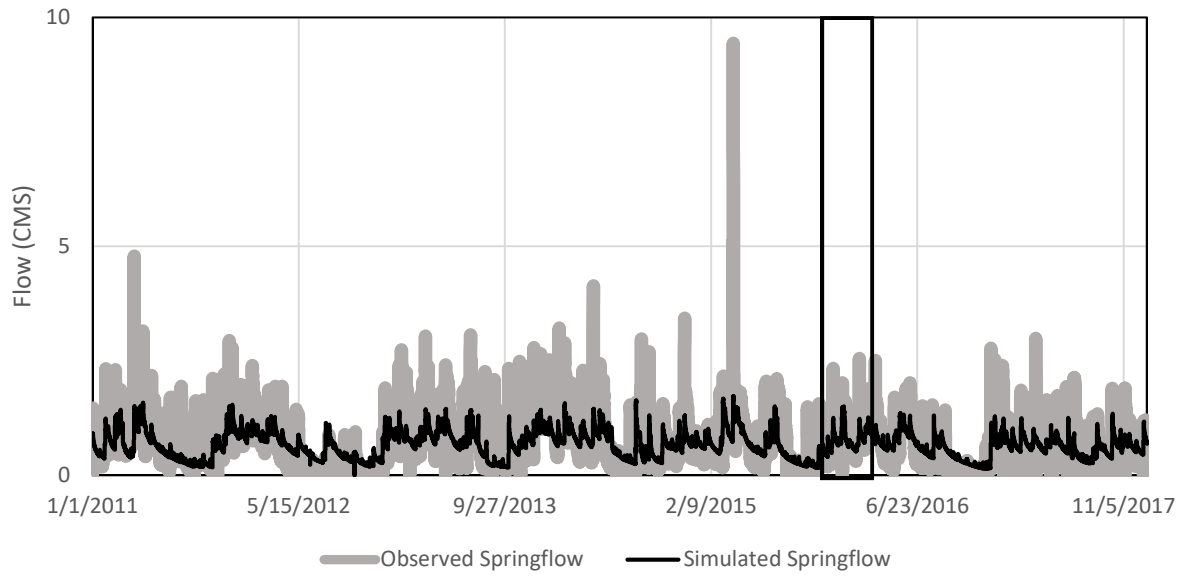


Figure 20. Spring Discharge for a Well Performing Model Run. Details of the time period in the window are shown in Figure 24.

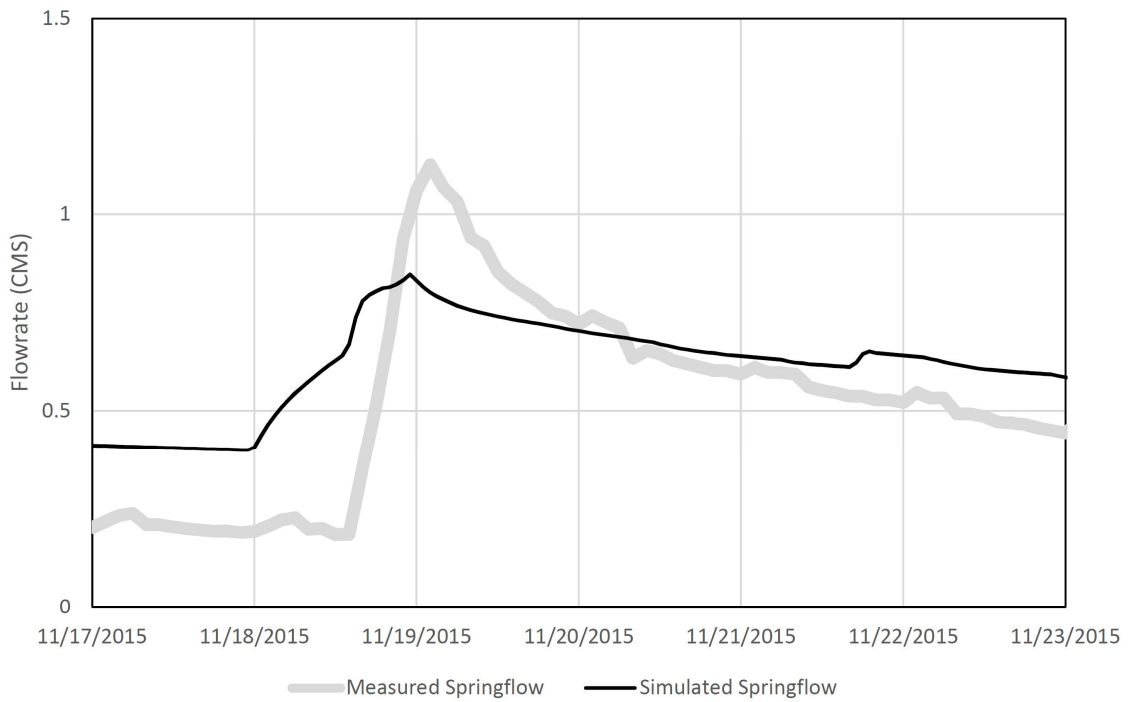
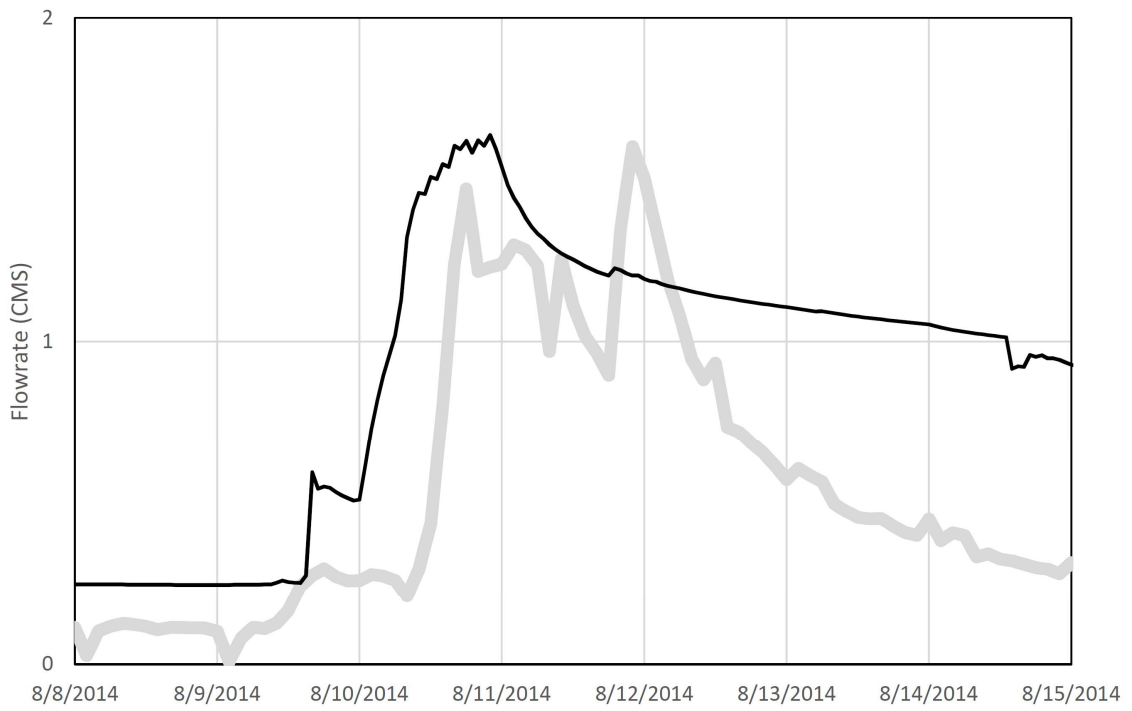


Figure 21. Simulated and Observed Spring Hydrographs for two Hydrologic Events

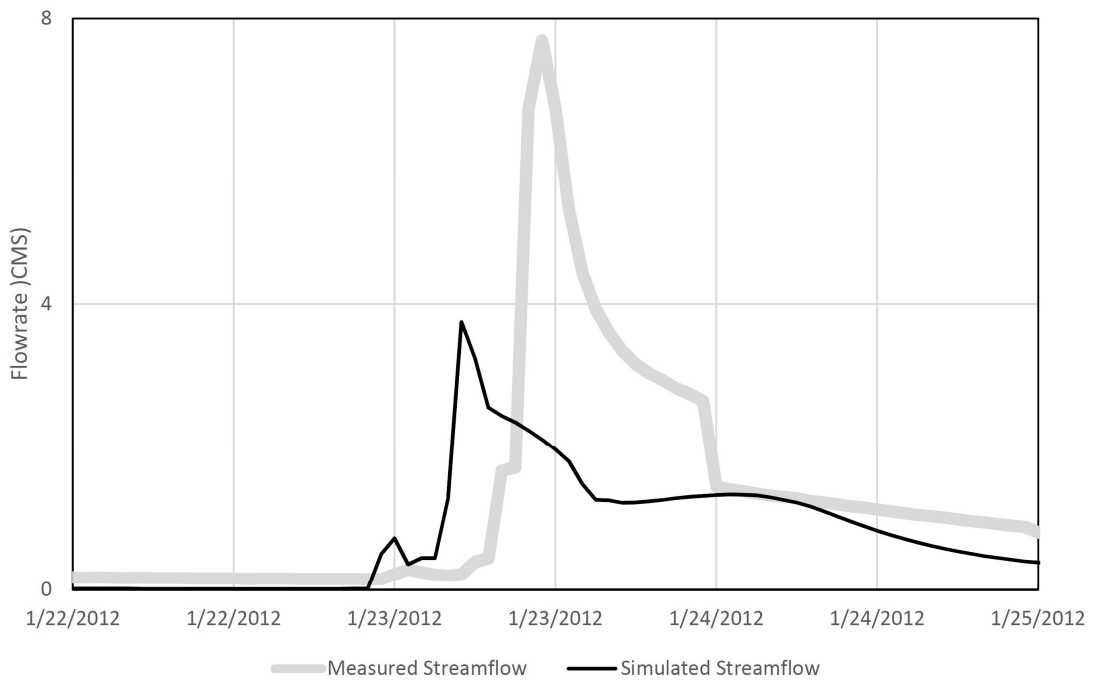
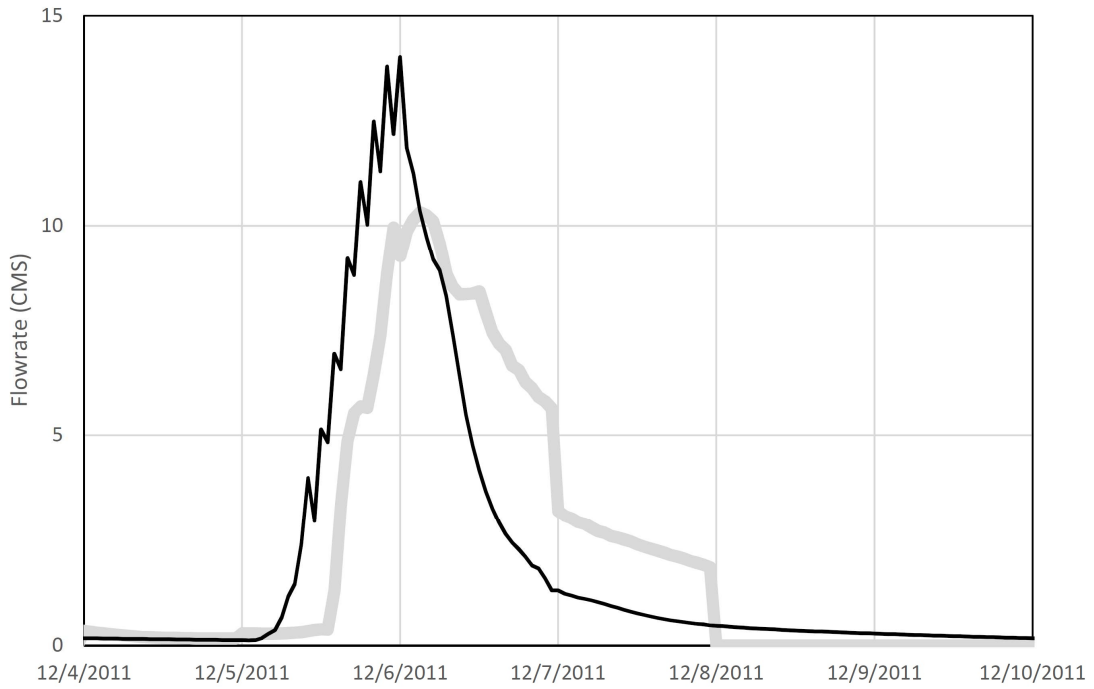


Figure 22. Simulated and Observed Stream Hydrographs for two Hydrologic Events

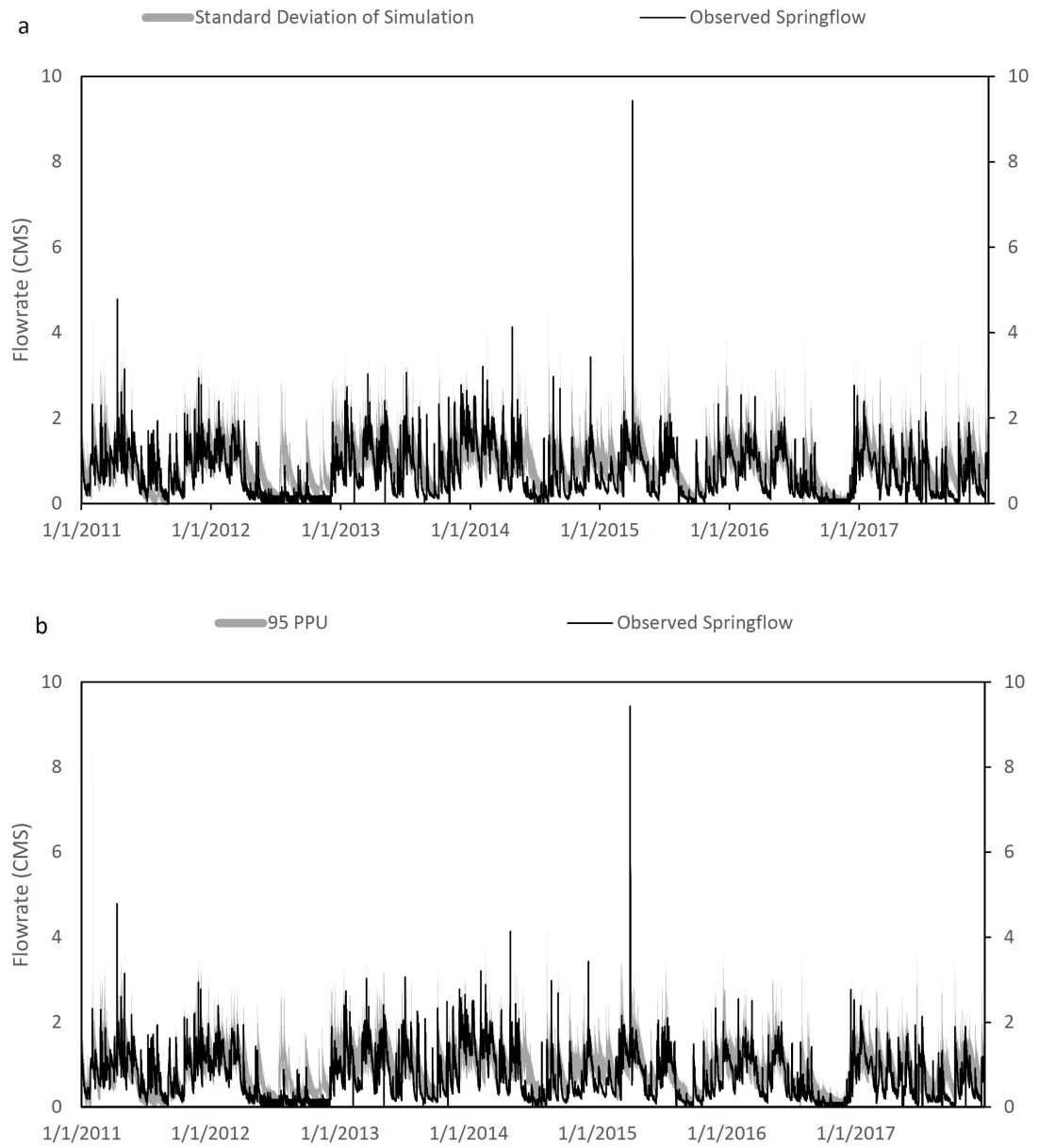


Figure 23. Model Uncertainty by a) Standard Deviation from the Mean Simulated Streamflow and b) 95% Prediction Uncertainty

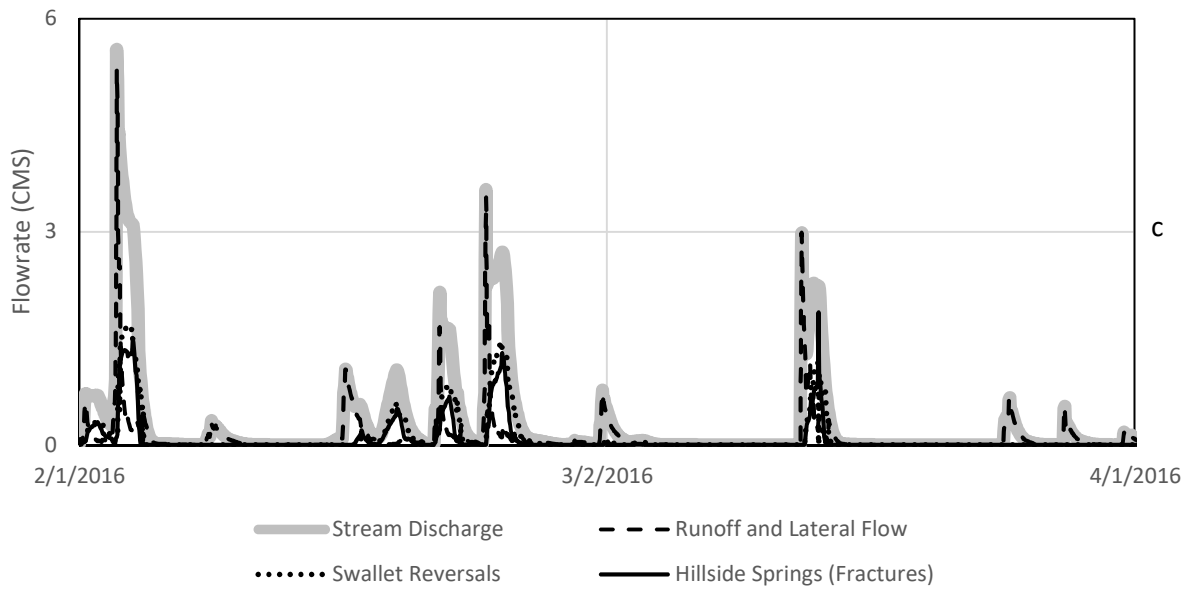
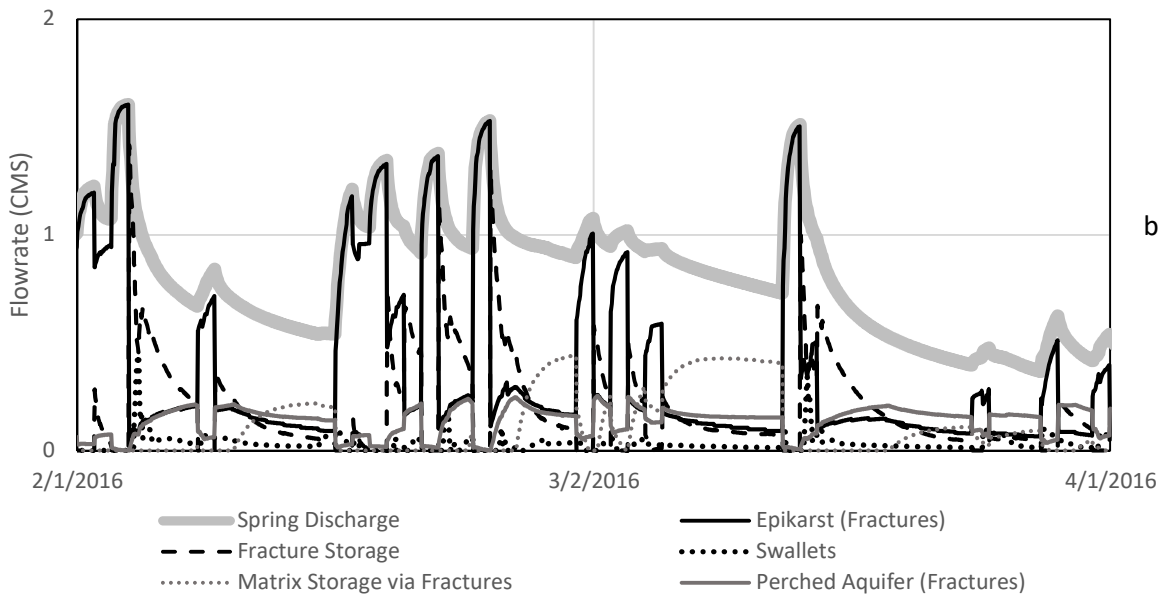
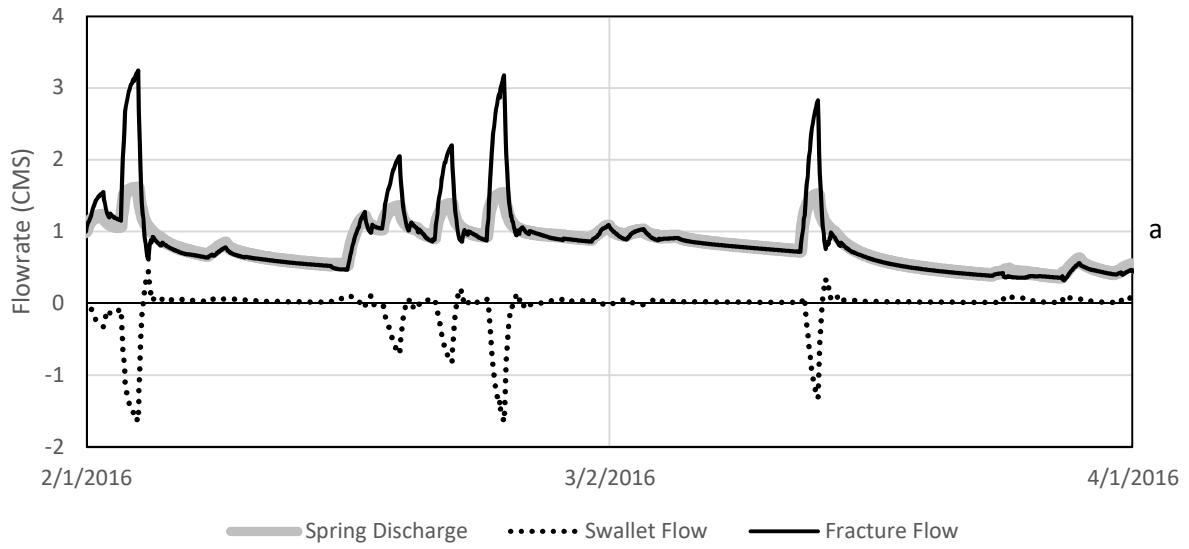


Figure 24. Model Results for 2-Month Window a) Spring Discharge with Total Fracture and Swallet Flow. b) Total Karst Pathway Contributions to Spring Discharge. c) Pathway Contributions to Stream Discharge.

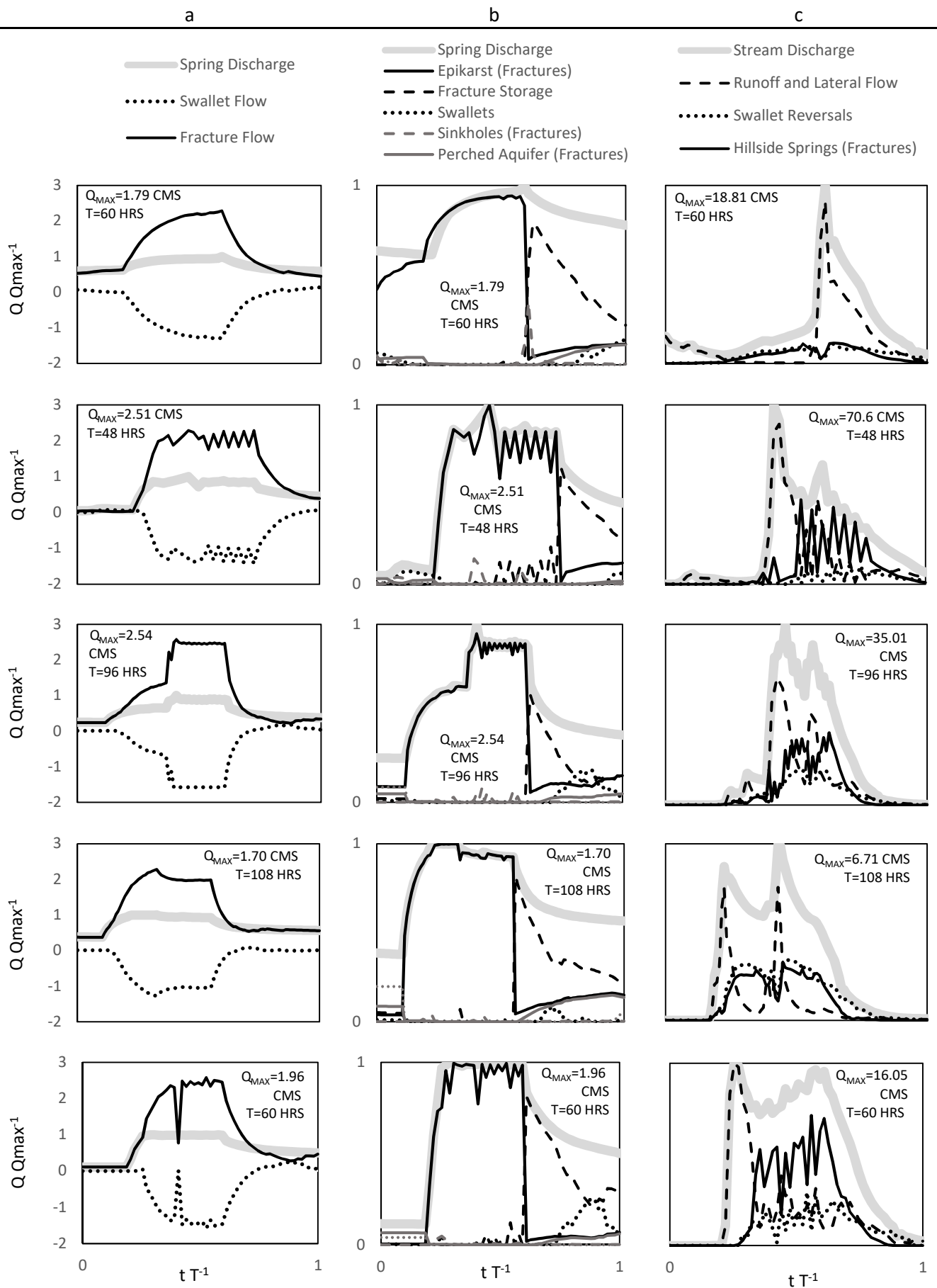


Figure 25. Model Results during Extreme Hydrologic Events. a) Modeled Spring Discharge with Swallet, Matrix, and Fracture Fluxes. Flowrates are normalized to the maximum spring discharge and the x-axis is normalized to the duration of the event. The maximum flowrate in cubic meters per second and the duration of the event in hours is displayed in each plot. Some fracture flow values were omitted because of anomalous behavior. b) Modeled Spring Discharge with Karst Pathway Contributions: swallet flow, epikarst recharge to fractures, sinkhole recharge to fractures, perched aquifer recharge to fractures, and draining fracture storage. Flowrates are normalized to the maximum spring discharge and the x-axis is normalized to the duration of the event. The maximum flowrate in cubic meters per second and the duration of the event in hours is displayed in each plot. c) Modeled Surface Stream Outflow with Pathway Contributions: surface runoff and lateral flow, fracture overflow at hillside springs, and swallet reversal flow, all shown in cubic meters per second. Flowrates are normalized to the maximum stream discharge and the x-axis is normalized to the duration of the event. The maximum flowrate in cubic meters per second and the duration of the event in hours is displayed in each plot. Extreme hydrologic events (top to bottom) are as follows: July 21, 2013 (77.2 mm), August 8, 2014 (166.9 mm), April 2, 2015 (162.6 mm), February 28, 2017 (54.9 mm), and October 8, 2017 (103.4 mm).

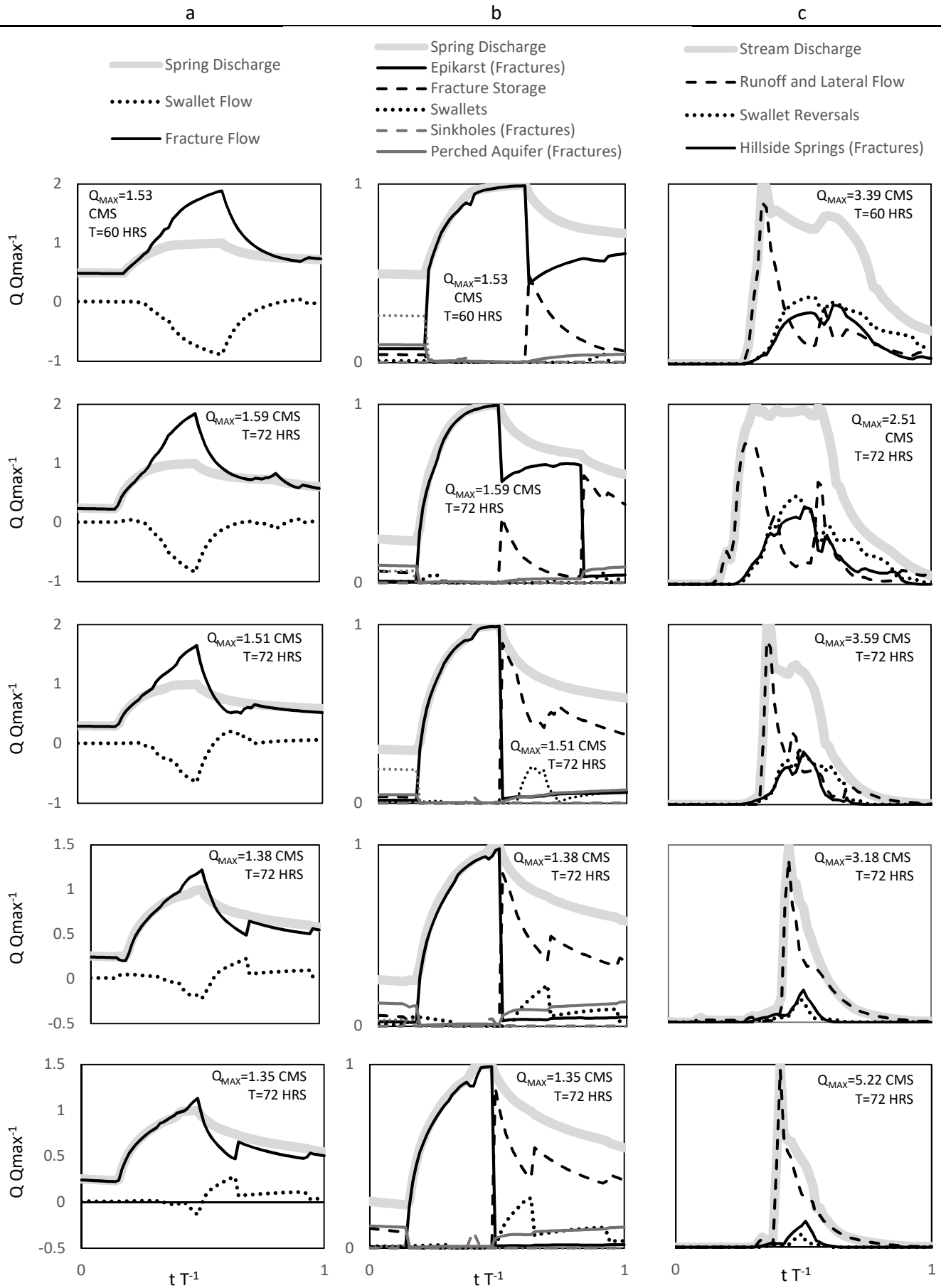


Figure 26. Model Results during Moderate Hydrologic Events. a) Modeled Spring Discharge with Swallet, Matrix, and Fracture Fluxes. Flowrates are normalized to the maximum spring discharge and the x-axis is normalized to the duration of the event. The maximum flowrate in cubic meters per second and the duration of the event in hours is displayed in each plot. b) Modeled Spring Discharge with Karst Pathway Contributions: swallet flow, epikarst recharge to fractures, sinkhole recharge to fractures, perched aquifer recharge to fractures, and draining fracture storage. Flowrates are normalized to the maximum spring discharge and the x-axis is normalized to the duration of the event. The maximum flowrate in cubic meters per second and the duration of the event in hours is displayed in each plot. c) Modeled Surface Stream Outflow with Pathway Contributions: surface runoff and lateral flow, fracture overflow at hillside springs, and swallet reversal flow, all shown in cubic meters per second. Flowrates are normalized to the maximum stream discharge and the x-axis is normalized to the duration of the event. The maximum flowrate in cubic meters per second and the duration of the event in hours is displayed in each plot. Moderate hydrologic events (top to bottom) are as follows: January 11, 2012 (28.2 mm), May 12, 2012 (48.0 mm), November 11, 2015 (22.4 mm), April 10, 2016 (17.0 mm), and August 22, 2017 (27.2 mm).

Chapter 6 Discussion

6.1) Net Hydraulic Pathway Results

Modelling results provide evidence of hydrologic pathways dominated by fracture flow, epikarst transfer and runoff. Modelling ensemble analyses consistently pointed to a high fracture-matrix permeability ratio for the groundwater basin. Springflow was about 70% drainage while streamflow surface outlet is 30% of drainage, annually. Hydrologic pathways contributing to springflow are soil to epikarst to fracture network connectivity during hydrologic events, draining of the fracture network during recession and baseflow periods, and to a lesser degree pirating of runoff by swallets. Pathways contributing to the streamflow surface outlet are runoff, hillside springs from the overflowing fracture network, and swallet reversal when the near full fracture network pressures and overflows the cave system.

All modelled possible pathways are shown in Figure 27, and then weighted solid lines show the seven main hydrologic pathways found to occur in this fluviokarst system. The spring hydrograph is dominated by water originating as infiltrated soil water and traveling through the fracture network. Water percolates from soil to the epikarst to the fracture network to the conduit and then exits at the springhead (see heavy weighted line a in Figure 27). The pathway contributes 95% of the springflow during hydrologic events and 57% of the springflow annually. During hydrologic events, the epikarst is highly active and the pathway is connected from the soil to the springhead. During initial recession periods, the epikarst becomes inactive but the fracture network drains to supply water to the spring. As the recession continues and during low-flow periods, the stored water in the perched aquifer, and stored water in the saturated matrix begin to recharge the fracture

network. Relatively small contributions of surface streamflow contribute to the spring hydrograph during throughout hydrologic events, especially during the low and moderate flow hydrologic events. Surface streamflow is pirated by the more than fifty fluviokarst swallets. Water travels vertically to the phreatic conduit located approximately 18 meters below the surface streambed and then travels to the spring (see medium weighted line b in Figure 27). The surface streamflow swallet pathway contributes approximately just 5% to the spring hydrograph during hydrologic events, and just 6% contribution to the spring annually. Modelling results suggest matrix associated sources of water and their pathways provide very small to near zero contributions to springflow in this system.

Modelling results suggest three hydrologic pathways contribute to the streamflow hydrograph at the watershed's surface outlet. The surface stream is only active during hydrologic events. Surface runoff travels to the watershed's surface outlet via the surface stream network and contributes 47% of the water to the outlet annually (see medium weighted line c in Figure 27). The second and third event-activated pathways convey water via the subsurface fracture network. Hillside springs contribute 30% annually to the watershed's surface outlet. The hydrologic pathway is defined by water percolation from soil to the epikarst to the fracture network to hillside springs to the stream network to the watershed outlet (see medium weighted line d in Figure 27). Activation of the hillside springs occurs when the potentiometric surface of the fracture network exceeds the surface stream, and the pathway is activated $15(\pm 5)$ times per year in the Cane Run Royal Spring system. Swallet reversal, defined when the in-stream fluviokarst features act as overflow springs (see medium weighted line e in Figure 27), contribute 23% annually to the watershed's surface outlet. Swallet reversal is associated with moderate precipitation

events falling on wet soils to extreme rainfall events. The fracture network fills near to the epikarst across the landscape, which is well above of the surface stream elevation, and thus places a substantial pressure head the conduit system and overflow occurs at the swallets. The hydrologic pathways is defined by water percolation from soil to the epikarst to the fracture network to the conduit to swallets to the surface stream to the watershed's surface outlet. Swallet reversal occurs $10(\pm 4)$ times per year in the study system.

6.2) Fluviokarst Features

Hydrologic pathways and their connectivity are perhaps understudied for fluviokarst systems, and the present study points out some features of fluviokarst systems that might be considered in future research. Characteristics of the fluviokarst system are surface and subsurface outlets to the drainage basin showing similar order of magnitude conveyance of water and in-stream coupling via the swallet features.

In the present study system, model optimization shows the fracture-matrix permeability ratio as rather high (10^5 to 10^8), which places the system in the regime of fracture flow dominating subsurface karst drainage and minimal contributions from the matrix (Matthai and Belayneh, 2004). Surely this result is evident for our pathway analyses (Figure 27) and the results in Figures 24 through 26, where the hydrologic pathway via the fractures to the conduit dominate springflow. Additionally, this concept can be further extended for fluviokarst. For fluviokarst systems with high fracture-matrix permeability ratios, the pronounced influence of fracture flow to *both* surface and subsurface outlets of the stream and spring, respectively should be considered. Combined, hillside springs and

swallet reversal constitute roughly 50% of the water contribution to the watershed's surface outlet. Modelling results provide evidence that the hillside springs and swallet reversal occur due to the pressure head of the fracture flow network and subsequent conveyance of water through the network. This is perhaps a surprising result given the optical nature of runoff and the perceived flashiness of the fluviokarst surface stream. These findings were further validated the results through field visits during the late winter and early spring periods of 2019 and found the creek's inundation and active hillside springs extending several days after runoff ceased. We were not able to survey the in-stream swallets during these times due to safety hazards, but this serves as future research.

In future work, researchers might consider the potential of fluviokarst systems with high fracture-matrix permeability ratio to have fracture flow dominating both surface and subsurface outlets. A caveat to this concept will be systems with poorly drained soils or high impervious surfaces across the watershed, which might lead to runoff dominating water's contribution to the surface flow outlet.

In addition to the multiple outlets, the 'fluviokarst' classification invokes the presence of in-stream coupling of surface stream and subsurface high porosity zones via the swallet features. During the onset of storm events, the researchers observed as the surface stream spills to swallet for minutes to a half hour, then fills the swallet completely and the stream overtops the swallet. We drive downstream about one kilometer to the next set of swallets and observe the same phenomena. This optical nature of the swallets has led a persistence of the features as sinks the past 40 years, although flow reversal has never been discounted. Investigation of the swallets during flood events has been sparse due to safety considerations, and the potential of researchers being sucked down the larger

swallets, and we have only one named and documented estavelle in the system (Thraillkill et al., 1991). Modelling results herein provide evidence that net swallet reversal exceeds swallet sink capacity by approximately $5(\pm 2)$ times in the Cane Run Royal Spring basin. In hindsight, the fluviokarst features should be more aptly named estavelles in this study system. A recent fluviokarst study examined the potential downstream ecosystem effects of such flow reversal (Hensley and Cohen, 2016). That study coupled with the present study places emphasis on considering the estavelle behavior in future work for similar systems.

6.3) Implications for Studying Fluviokarst Springflow

One implication of the behavior identified in this fluviokarst system is the inference of recession analyses and transfer functions from previous research to be applicable, or lack thereof, to fluviokarst systems. In karst studies, often inflections and shifts in recession curves are interpreted to reflect shifts in the transfer of water associated with activation of a different storage zone in the karst subsurface with a different porosity, transfer and storage characteristics (Talarovich and Krothe, 1998; Baedke and Krothe, 2001; Pinault et al., 2001; Worthington et al., 2007; Fiorillo, 2011; Hosseini et al., 2017; Xu et al., 2018). In the present study, inflections in the recession of the spring hydrograph are shown to be associated with the ceasing of activity of the hillside springs, swallet reversals, and the epikarst to fracture pathway. As these exits stop conveying water to the surface stream and surface water outlet, the hydraulics of the fracture flow pressure head changes leading to a more gradual gradient in the springflow recession curve. We elaborate on this concept below.

Our modelling evidence suggests the structure of the fluviokarst spring hydrograph reflects shifts in inputs to, or outputs from, the fracture network, as opposed to shifts in the transfer of water from storage zones with different porosity. The spring hydrograph can exhibit a blocky structure with abrupt inflection points. Additional rainfall to the basin does not account for the blocky structure, and the hydrograph structure occurs for both modelling results and data results. Analyses of our modelling results (see Figures 24 through 26) shows the inflections are due to ceasing of discharge from the fracture network at hillside springs, ceasing of discharge via swallet reversal, and the onset or ceasing of epikarst recharge to the fracture network. As the inputs and outputs to the fracture network change, so too does the recession of the water flowrate through the conduit system to the spring.

The structure and interpretation of the fluviokarst spring hydrograph is contrary to interpretations in many past karst studies. Often inflections and shifts in recession curves are interpreted to reflect shifts in the transfer of water associated with activation of a different storage zones in the karst subsurface with a different porosity and transfer and storage characteristics (Fiorillo, 2014; Xu et al., 2018). Such studies suggest phenomena such as shifting from conduit dominated transfer to fracture flow to matrix water transfer, and thus reflecting a change from tertiary to secondary to primary porosity. Springflow for the fluviokarst system in the present study is shown to nearly always be dominated by flow from the fracture network. Researchers might consider the potential for ceasing of swallet reversal, hillside spring outlets, and epikarst recharge shifts to control inflection of recession curves for fluviokarst systems.

Related to the hydrograph structure, interpretation of the dominant transfer mechanisms of the fluviokarst system studied here is contrary to the often cited interpretations for dual-transfer (i.e., quick- and slow-flow) or triunal-transfer (i.e., quick-, intermediate-, and slow-flow) in karst studies (e.g., Pinault et al., 2001; Worthington, 2007; Long, 2009). In this fluviokarst system, relative transfer as quick- or slow- reflects varying conditions of the fracture flow network. The springflow hydrograph in our system most often displays dual-transfer, and the ‘quick-flow’ component occurs when the epikarst is actively supplying transfer to the fracture network as well as during the larger hydrologic events when hillside springs and swallet reversal are active exits from the fracture network. The ‘slow-flow’ component occurs when the fracture network is draining or the matrix or perched aquifer is recharging the fracture network. At times, a triunal-transfer can be inferred for this system when shifts in epikarst activity, hillside springs, or swallet reversal are substantially separated from one another in time and shift behavior of the fracture network such that transfer shifts are observed at the springhead.

The quick-flow observed at the fluviokarst springhead is contrary to more traditionally defined direct underground runoff such as from sinking streams or landscape sinkholes. These direct underground runoff contributions do exist in this fluviokarst system (see Figures 25 and 26) and account for about 6% of the springflow annually (Table 18). However, these components do not constitute quick-flow on the rising limb of the spring hydrograph because the system is phreatic and piston flow occurs first, and the contribution of the direct runoff is small relative to the soil to epikarst to fracture contribution.

Quick-, intermediate- and slow-flow observed in this system are also contrary to the often cited where karst studies infer conduit, epikarst/fracture, and matrix associated transfers (Worthington, 2007). Modelling results provide evidence the present study system has a high fracture-matrix permeability ratio, so matrix flow does not directly contribute appreciable transfers to the spring hydrograph. The matrix only contributed flow to the spring by providing recharge to the fracture network during recession and baseflow periods. Perhaps the quick-flow in this study could be associated with the epikarst, but the connectivity reflects the high input of the epikarst to the fracture network. The quick- and slow-flow dual-transfer seems reasonable for the surface outlet during hydrologic events where transfers occur from direct surface runoff or subsurface sources, albeit the subsurface sources are active hillside springs from the fracture network and swallet reversal. Researchers might consider the interpretation herein when investigating other similar fluviokarst systems.

6.4) Advantages and Disadvantages of the Numeric Model for Fluviokarst

Results suggest the utility of the formulated numerical model for applications to fluviokarst systems. One advantage of the numerical model presented here is the capability to handle the hydrologic and hydraulic complexity of fluviokarst. The mature fluviokarst system is perhaps even more complex than springflow dominated karst drainages due to the similar order of magnitude dependence of both surface outflows and karst outflows from the drainage network. As mentioned previously, the complexity of the over fifty in-stream estavelles and numerous water exits produces difficulty in more traditional inference of source allocation of the karst spring hydrograph. For this reason, our

numerical modelling provides an approach to consider 20+ potential pathways for which water can move from precipitation through the surface-subsurface fluviokarst system to the four exits (see Figure 2).

Another advantage was the model structure was able to omit our prior biases of how the system might be behaving. *A priori* we anticipated reasonable contributions to the spring hydrograph from sinking streams (quick-flow), the fracture network, and the saturated rock matrix as well as the behavior of swallets to pirate surface streamflow to the subsurface conduit. Our prior biases were based on previous karst literature that tends to emphasize the three end-member concept in a number of papers (e.g., Pinault et al., 2001; White, 2002; Worthington, 2007; Long, 2009) and the optical nature of the swallets as sinks during our field reconnaissance. Nevertheless, we recognized the potential for the fracture network or rock matrix to dominate subsurface flows, as detailed in some papers (Matthai and Belayneh, 2004), and the potential for flow reversal of fluviokarst features (Chen and Goldscheider, 2014; Hensley and Cohen, 2016), including one named estavelle in our system (Thraillkill et al., 1991). Therefore, we used a wide range of prior parameterization to consider all potential storage zones and transfers contribution to karst transfer phenomena. Optimization of the model structure allowed an un-biased parameterization detailed in the model evaluation of the 20+ pathways by using the multiple objective functions for both spring and surface outlets and performing robust Sobol sequencing for the parameters considered.

Disadvantages of applying the numerical model are its computational expense and the need for a well-studied karst system ahead of time. The computational time associated with solving the system of equations that couples the Richards equation, cubic law, Darcian

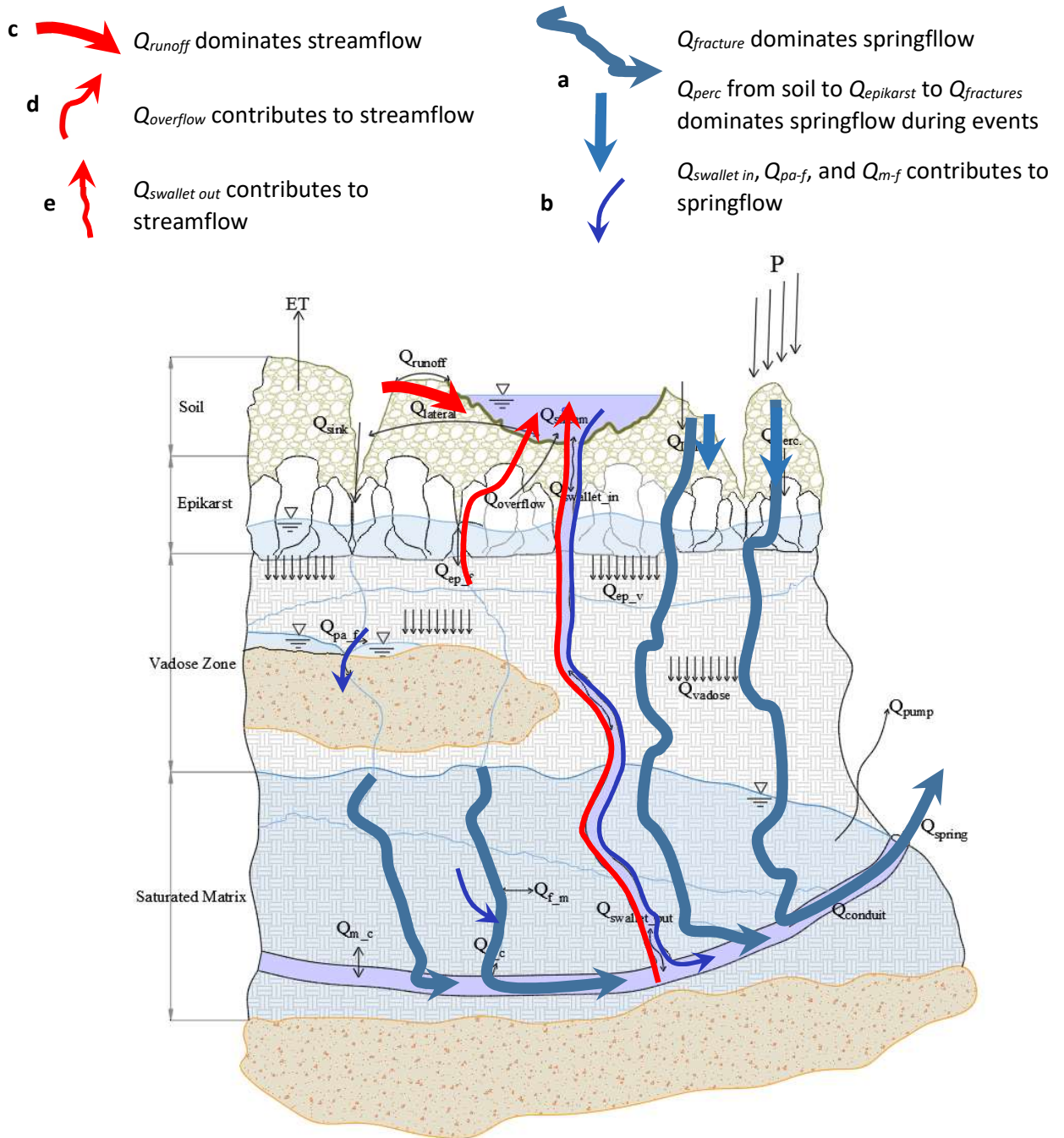
flow, open channel flow and pipeflow hydraulics was at times excessive. The computational time for calibration and validation runs with 2000 Sobol simulations required three days on a Lipscomb Computer Cluster for the eight-year simulation time at hourly time step. Model optimization would have been impractical were it not for the Lipscomb Computer Cluster, recently constructed by the University of Kentucky. Future research might investigate further programming efficiency of the code. Second, as mentioned, the study system was well characterized in terms of its subsurface conduit and surface and subsurface characteristics from previous tracer tests, lidar mapping, electrical resistivity mapping, research well drillings and data collection, isotope tracer studies, data-driven water budgets, and routine long term and event-based water quality measurements. This prior information made characterization of the model domain, and especially the subsurface conduit, feasible. Future research might advance tomography research for practical and new technology considerations to make application of numerical modelling more feasible in fluviokarst.

Another disadvantage of our numeric model was the treatment of fracture heterogeneity. We accounted fracture heterogeneity at a sub-basin scale by adjusting the fracture density in each groundwater cell based on the structural curvature of the rock members, which is assumed to correlate to higher stresses in the bedrock (Harris et al., 1960; Hanks et al., 1997). However, we recognize that structural rock folding is not the only factor driving fracture heterogeneity (Lamarche et al., 2012), and that fracture heterogeneity may be observed at smaller scales (Faybishenko et al., 2000).

Additionally, a potential model limitation is the simulation of soil water percolation was performed on a daily basis in SWAT, despite the surface flows being calculated for

hourly time-steps. This research suggests that the soil to epikarst to fracture network pathway is the dominant pathway controlling the hydrograph at the studied spring. Future research may be able to improve the results of this model by simulating soil water processes on an hourly time-step.

Figure 27. Major hydrologic pathways of the fluviokarst systems evidenced by the numerical modelling.



Chapter 7 Conclusion

The conclusion of this thesis research is as follows:

1. The Cane Run Royal Spring basin is aptly classified as a fluviokarst basin in the inner bluegrass. Springflow was about 70% drainage while streamflow surface outlet is 30% of drainage, annually.
2. Five pathways control springflow, and three pathways control streamflow at the watershed outlet. Hydrologic pathways contributing to springflow are soil to epikarst to fracture network connectivity during hydrologic events, draining of the fracture network during the initial recession periods, soil to epikarst to vadose zone to perched aquifer to fracture network during recession and baseflow periods, and to a lesser degree matrix recharge to fractures during recession and baseflow periods, and pirating of runoff by swallets. Pathways contributing to the streamflow surface outlet are runoff, hillside springs from the overflowing fracture network, and swallet reversal when the near full fracture network pressures and overflows the cave system.
3. Fluviokarst landscapes with high fracture-matrix permeability ratios contain fractures that may strongly influence both the springflow and surface streamflow. Fracture flow controls 95% of springflow and 25% of streamflow in this basin.

4. Swallet features may be just as important as sources to the streamflow during high rainfall events as sinks from the streamflow in fluviokarst basins, which is contrary their optical nature as sinks.
5. Inflections in the spring hydrograph represent shifts in the surface and subsurface connectivity via the fractures, as opposed to shifts in dominant storage zones draining water from the karst portion of the basin. Related, transfer mechanisms inferred with hydrograph analyses reflect hydraulic shifts as opposed to porosity zone shifts at the spring. The implication is existing methods of dual- and triunal hydrograph separation of karst springflow may not be directly transferrable to fluviokarst springs.
6. The developed numerical model uses a combined discrete-continuum (CDC) hybrid approach and captures fluvial, karst, and connected fluvial-karst pathways of the basin. The most sensitive parameters controlling surface flow or subsurface flow objective functions were fracture density, aperture thickness, friction coefficients, and the saturated hydraulic conductivity of the rock matrix.
7. Advantages and disadvantages of the model might be considered in future work. The model can provide evidence of dominant pathways in complex terrane and relaxes *a priori* constraints, i.e., potential bias, of the modeler when parameterizing the model. However, the modelling is computationally expensive and requires previously studied and mapped cave and stream networks.

List of Symbols

A	=	cross-sectional area of a stream reach
A_c	=	cross-sectional area of conduit
A_{cell}	=	area of groundwater cell
$A_{m,c}$	=	surface area of the conduit
$A_{pa,f}$	=	area of fracture and perched aquifer flow exchange
$A_{f,m}$	=	area of fracture and matrix flow exchange
A_{sink}	=	area of sinkhole drainage within a sub-watershed
$A_{swallet}$	=	cross-sectional area of swallet
A_{ws}	=	area of a sub-watershed
AWC	=	available water capacity
b	=	fracture aperture
c	=	flood wave celerity
c_p	=	specific heat at constant pressure
c_{weir}	=	weir constant
COV_{sol}	=	soil cover index
CN	=	curve number
CV	=	aboveground biomass and residue
d	=	diameter of pipe, conduit, or swallet
dx	=	flowpath distance (Darcy's Law and cubic law)
D	=	diameter of conduit or swallet
$D(\theta)$	=	diffusivity
e_z	=	water vapor pressure of air at height z
e_z^0	=	saturation vapor pressure of air at height z
E	=	depth rate evaporation
E_s	=	maximum soil evaporation on a given day
E'_0	=	potential evapotranspiration
$E_{soil,ly}$	=	evaporative demand for given soil layer
E_t	=	maximum transpiration on a given day
f	=	Darcy-Weisbach friction factor
f_{inf}	=	infiltration rate
F_{inf}	=	cumulative infiltration
FC	=	amount of water in the soil profile at field capacity
g	=	gravitational acceleration
h	=	hydraulic head
h_{bkf}	=	bankfull height of stream reach
h_{ep}	=	height of water stored in epikarst
$h_{ep th}$	=	epikarst threshold height when water is delivered to fracture network
h_f	=	height of fracture network free surface relative to conduit
$h_{f max}$	=	maximum height of fracture network free surface relative to conduit
h_m	=	height of saturated matrix free surface relative to conduit

h_{pa}	=	height of perched aquifer free surface relative to top of impermeable layer
$h_{pa\ th}$	=	height of perched aquifer threshold, conceptual horizontal fracture
h_{stream}	=	height of water in stream reach
$h_{swallet}$	=	height of water stored in a swallet relative to a conduit node
H	=	height of water in a stream reach
H_{net}	=	net radiation
H_{pa}	=	height of bottom of perched aquifer relative to conduit
ΔH_{stream}	=	elevation difference between stream reach bed and conduit section
$H_{swallet}$	=	elevation difference between the creek (top of swallet), and the conduit
k	=	permeability
k_s	=	flood wave coefficient
$K(\theta)$	=	hydraulic conductivity
K	=	storage time constant
K_e	=	s effective hydraulic conductivity
K_s	=	saturated hydraulic conductivity
K_{sat}	=	saturated hydraulic conductivity
l	=	flowpath length
l_c	=	straight-line distance between conduit nodes
L_c	=	straight-line length of conduit in a groundwater cell
L_{hill}	=	hillslope length
L_{slp}	=	subbasin slope length
L_{stream}	=	length of stream reach
$L_{swallet}$	=	total length of swallet segment
n	=	Manning's n
n_{ch}	=	Manning's n for channel flow
n_m	=	saturated porosity of bulk rock
n_{ov}	=	Manning's roughness coefficient for overland flow
n_{ep}	=	saturated porosity in epikarst
\hat{n}	=	unit vector normal to control surface
N	=	fracture density
p_c	=	pressure at a conduit node
q	=	flowrate per unit area
q_{ch}	=	channel flowrate
q_f	=	flow per unit area in fracture network
$q_{f,c}$	=	flow exchange velocity between fracture network and conduit
$q_{f,s}$	=	flow exchange velocity between fracture network and stream
$q_{m,c}$	=	flow exchange velocity between saturated matrix and conduit
	=	flow per unit width between the perched aquifer and the fracture network
$q_{pa,f}$		
Q	=	volumetric flowrate

Q_c	=	volumetric flowrate in conduit
Q_{dn}	=	volumetric flowrate out of a stream reach to a downstream reach
$Q_{ep,f}$	=	volumetric flowrate of water entering fracture network from epikarst
$Q_{ep,v}$	=	volumetric flowrate of water entering vadose zone from epikarst
$Q_{ep,stream}$	=	volumetric flowrate of epikarst overflow to stream
$Q_{f,c}$	=	volumetric flow exchange rate between fracture network and conduit
$Q_{f,m}$	=	volumetric flow exchange rate between fracture network and matrix
$Q_{f,s}$	=	volumetric flow exchange rate between fracture network and stream
Q_{in}	=	volumetric flow from stream into swallet
Q_{inf}	=	volumetric flow into soil layer
$Q_{Lateral}$	=	total volumetric lateral soil flow within a sub-watershed
Q_{lat}	=	volumetric lateral soil flow delivered to a stream or tributary
$Q_{m,c}$	=	volumetric flow exchange rate between saturated matrix and conduit
Q_{net}	=	net volumetric flowrate in/out of a control volume
Q_{over}	=	volumetric flowrate from fracture network to streams via hillside springs
$Q_{pa,f}$	=	volumetric flow exchange between perched aquifer and fracture network
Q_{perc}	=	volumetric flowrate entering epikarst from soil layer
Q_r	=	volumetric flow per Manning's Equation used in Jones Equation
Q_{Runoff}	=	total volumetric surface runoff in a sub-watershed
Q_{sink}	=	volumetric flowrate of water entering fracture network from sinkholes
Q_{sur}	=	volumetric surface runoff delivered to a stream or tributary
Q_{surf}	=	surface runoff discharged to the main channel on a given day
$Q_{swallet}$	=	volumetric flowrate in swallet
$Q_{swall-in}$	=	volumetric flowrate into swallet from stream (negative values for reversals)
$Q_{swall-out}$	=	volumetric flowrate into conduit from swallets
Q_{trib}	=	volumetric flow from tributaries
Q_{up}	=	volumetric flowrate into a stream reach from an upstream reach
Q_{vadose}	=	of the percolating vadose zone water reaching the saturated matrix
r_a	=	diffusion resistance of the air layer
R	=	hydraulic radius
$R_{\Delta t}$	=	amount of rain falling during the time step

s	=	bed slope of stream reach
slp_{ch}	=	channel slope
$surlag$	=	surface runoff lag coefficient
S	=	source/sink term
S_0	=	bed slope of stream reach
SC	=	storage coefficient
SAT_{ly}	=	amount of water in the soil layer when completely saturated
SW	=	soil water content
t	=	time
t_{ch}	=	time of concentration for channel flow
t_{conc}	=	time of concentration
t_{ov}	=	time of concentration for overland flow
TT_{lag}	=	lateral flow travel time
TT_{perc}	=	travel time for percolation
u	=	model velocity
v	=	flow velocity
v_c	=	flow velocity in conduit segment
$v_{swallet}$	=	flow velocity in swallet
$v(\theta)$	=	velocity of vadose zone trailing wave
\hat{v}	=	fluid velocity vector
V	=	volume
V_{ep}	=	volume of stored water in epikarst
V_f	=	volume of stored water in fracture network
V_{in}	=	volume of inflow to stream or tributary
V_m	=	volume of stored water in saturated matrix
V_{out}	=	volume of outflow of stream/tributary
V_{pa}	=	volume of stored water in perched aquifer
$V_{swallet}$	=	volume of water stored in a swallet
w_{perc}	=	water percolating to underlying soil layer
WP	=	water content at wilting point
x	=	spatial coordinate
X	=	weighting factor
X_{stream}	=	horizontal distance between a stream reach and conduit node
Δx_{cell}	=	distance between conduit and area-weighted center of groundwater cell
z	=	elevation
z_c	=	elevation of conduit node
z_{spring}	=	elevation of spring
γ	=	specific weight
γ_p	=	psychometric constant
ρ	=	density
ϵ	=	Brooks-Corey coefficient
ϕ_{soil}	=	porosity of the soil
ϕ_d	=	drainable porosity of the soil

θ	=	volumetric water content
θ_r	=	residual volumetric water content
θ_s	=	saturated volumetric water content
τ_c	=	tortuosity of conduit
τ_c	=	tortuosity of swallet
μ	=	viscosity
π	=	ratio between the circumference and diameter of a circle
Ψ_{wf}	=	wetting front matric potential
λ	=	latent heat flux density
Δ	=	slope of the saturation vapor pressure-temperature curve
∇P	=	pressure gradient
$\Delta\theta_v$	=	change in volumetric moisture content across the wetting front

References

- Abbaspour, K. C. (2007). User manual for SWAT-CUP, SWAT calibration and uncertainty analysis programs. Swiss Federal Institute of Aquatic Science and Technology, Eawag, Duebendorf, Switzerland, 93.
- Al Aamery, N., Fox, J. F., & Snyder, M. (2016). Evaluation of climate modeling factors impacting the variance of streamflow. *Journal of Hydrology*, 542, 125-142.
- Amatya, D. M., Jha, M., Edwards, A. E., Williams, T. M., & Hitchcock, D. R. (2011). SWAT-based streamflow and embayment modeling of karst-affected chapel branch watershed, South Carolina. *Transactions of the ASABE*, 54(4), 1311-1323.
- Arnold, J.G., J.R. Williams, and D.R. Maidment. 1995. Continuous-time water and sediment routing model for large basins. *Journal of Hydraulic Engineering* 121(2): 171-183.
- Arnold, J.G., Moriasi, D.N., Gassman, P.W., Abbaspour, K.C., White, M.J., Srinivasan, R., Santhi, C., Harmel, R.D., van Griensven, A., Van Leiw, M.W., Kannan, N., Jha, M. K., 2012. SWAT: Model use, calibration, and validation. *Am. Soc. Agricult. Biol. Eng.* 55 (4), 1491–1508.
- Baedke SJ, Krothe NC (2001) Derivation of effective hydraulic parameters of a karst aquifer from discharge hydrograph analysis. *Water Resour Res* 37:13–19. doi: <https://doi.org/10.1029/2000WR900247>
- Baffaut, C., & Benson, V. W. (2009). Modeling flow and pollutant transport in a karst watershed with SWAT. *Transactions of the ASABE*, 52(2), 469-479.
- Bandy, A. M., Cook, K., Fryar, A. E., & Zhu, J. (2019). Differential transport of *Escherichia coli* isolates compared to abiotic tracers in a karst aquifer. *Groundwater*.
- Bear, J., Tsand, C.F., de Marsily, G. (eds.), 1993. Flow and contaminant transport in fractured rock. Academic Press, San Diego, CA.
- Baedke, S. J., & Krothe, N. C. (2001). Derivation of effective hydraulic parameters of a karst aquifer from discharge hydrograph analysis. *Water Resources Research*, 37(1), 13-19.
- Bicalho CC, Batiot-Guilhe C, Taupin JD, Patris N, Van Exter S, Jourde H (2017) A conceptual model for groundwater circulation using isotopes and geochemical tracers coupled with hydrodynamics: A case study of the Lez karst system, France. *Chem Geol* 1–17. doi: 10.1016/j.chemgeo.2017.08.014
- Brooks, R. H., & Corey, A. T. (1964). Hydraulic properties of porous media and their

- relation to drainage design. *Transactions of the ASAE*, 7(1), 26-0028.
- Chang Y, Wu J, Jiang G, Zhao X, Zhang Q (2019) Investigating the appropriate model structure for simulation of a karst catchment from the aspect of spatial complexity. *Environ Earth Sci* 78:1–19. doi: 10.1007/s12665-018-8017-y
- Chen, Z., & Goldscheider, N. (2014). Modeling spatially and temporally varied hydraulic behavior of a folded karst system with dominant conduit drainage at catchment scale, Hochifen–Gottesacker, Alps. *Journal of Hydrology*, 514, 41-52.
- Chow, V. (1959). *Open-channel hydraulics* (Vol. 1). New York: McGraw-Hill.
- Courant, R., Friedrichs, K., & Lewy, H. (1928). On the partial difference equations of mathematical physics. *Mathematische Annalen*, 100(1), 32-74.
- Cressman, E. R. (1967). *Geologic map of the Georgetown quadrangle, Scott and Fayette Counties, Kentucky*: US Geological Survey Geologic Quadrangle Map GQ-605, scale, 1:24,000.
- Cressman, E. R., & Peterson, W. L. (1986). *Ordovician system. The geology of Kentucky: a text to accompany the geologic map of Kentucky*. US Geological Survey Professional Paper.
- Currens, J. C., Taylor, C. J., Webb, S., Zhu, J., Workman, S., Agouridis, C., ... & Husic, A. (2015). Initial Findings from the Karst Water Instrumentation System Station, Royal Spring Groundwater Basin, Kentucky Horse Park 2010-2014. In *Proceedings Kentucky Water Resources Annual Symposium, Kentucky Water Resources Research Institute* (pp. 9-10).
- Delbart C, Valdes D, Barbecot F, Tognelli A, Richon P, Couchoux L (2014) Temporal variability of karst aquifer response time established by the sliding-windows cross-correlation method. *J Hydrol* 511:580–588. doi: 10.1016/j.jhydrol.2014.02.008
- Doerflinger N, Zwahlen F (1998) *Practical guide to groundwater vulnerability mapping in karstic regions*. Swiss Agency for Environment, Forest and Landscape, Berne
- Domenico, P. A., & Schwartz, F. W. 1990, *Physical and chemical hydrogeology*
- Drahovzal, J. A., Harris, D. C., Wickstrom, L. H., Walker, D., Baranoski, M. T., Keith, B., & Furer, L. C. (1992). *The East Continent Rift Basin: A New Discovery*. Kentucky Geological Survey. Special Publication, 18.
- Drysdale, R., Pierotti, L., Piccini, L., & Baldacci, F. (2001). Suspended sediments in karst spring waters near Massa (Tuscany), Italy. *Environmental Geology*, 40(8), 1037-1050.
- Engel, B., Storm, D., White, M., Arnold, J., & Arabi, M. (2007). *A Hydrologic/Water*

- Quality Model Application 1. JAWRA Journal of the American Water Resources Association, 43(5), 1223-1236.
- Ewers, O. R. (1982). Cavern development in the dimensions of length and breadth (Doctoral dissertation).
- Faybishenko, B., Doughty, C., Steiger, M., Long, J. C., Wood, T. R., Jacobsen, J. S., ... & Zawislanski, P. T. (2000). Conceptual model of the geometry and physics of water flow in a fractured basalt vadose zone. *Water resources research*, 36(12), 3499-3520.
- Fenton O, Mellander PE, Daly K, et al. (2017) Integrated assessment of agricultural nutrient pressures and legacies in karst landscapes. *Agric Ecosyst Environ* 239:246–256. doi: 10.1016/j.agee.2017.01.014
- Filipponi, M. (2009). Spatial analysis of karst conduit networks and determination of parameters controlling the speleogenesis along preferential lithostratigraphic horizons (Doctoral dissertation, Verlag nicht ermittelbar).
- Fiorillo F (2011) Tank-reservoir drainage as a simulation of the recession limb of karst spring hydrographs. *Hydrogeol J* 19:1009–1019. doi: 10.1007/s10040-011-0737-y
- Fiorillo, F. (2014). The recession of spring hydrographs, focused on karst aquifers. *Water resources management*, 28(7), 1781-1805.
- Florea, L. J., Fratesi, B., & Chavez, T. A. (2005). The reflection of karst in the online mirror: A survey within scientific databases, 1960-2005. *Journal of Cave and Karst Studies*, 229.
- Ford, D. C., & Ewers, R. O. (1978). The development of limestone cave systems in the dimensions of length and depth. *Canadian Journal of Earth Sciences*, 15(11), 1783-1798.
- Gassman, P. W., Reyes, M. R., Green, C. H., & Arnold, J. G. (2007). The soil and water assessment tool: historical development, applications, and future research directions. *Transactions of the ASABE*, 50(4), 1211-1250.
- Green, W. H., & Ampt, G. A. (1911). Studies on Soil Physics. *The Journal of Agricultural Science*, 4(1), 1-24.
- Gupta, R. S. (2008). Hydrology and hydraulic systems. Waveland Press.
- Hanks, C. L., Lorenz, J., Teufel, L., & Krumhardt, A. P. (1997). Lithologic and structural controls on natural fracture distribution and behavior within the Lisburne Group, northeastern Brooks Range and North Slope subsurface, Alaska. *AAPG bulletin*, 81(10), 1700-1720.

- Harris, J. F., Taylor, G. L., & Walper, J. L. (1960). Relation of deformational fractures in sedimentary rocks to regional and local structure. *AAPG Bulletin*, 44(12), 1853-1873.
- Hartmann, A., Weiler, M., Wagener, T., Lange, J., Kralik, M., Humer, F., Mizyed, M., Rimmer, A., Barbera, J.A., Andreo, B., Butscher, C., & Huggenberger, P. (2013). Process-based karst modelling to relate hydrodynamic and hydrochemical characteristics to system properties. *Hydrology and earth system sciences*, 17(8), 3305-3321.
- Hartmann A, Goldscheider N, Wagener T, Lange J, Weiler M (2014) Karst water resources in a changing world: Approaches, of hydrological modeling. *Rev Geophys* 1–25. doi: 10.1002/2013RG000443. Received
- Hensley, R. T., Cohen, M. J., & Korhnak, L. V. (2014). Inferring nitrogen removal in large rivers from high-resolution longitudinal profiling. *Limnology and Oceanography*, 59(4), 1152-1170.
- Herman, E. K., Toran, L., & White, W. B. (2008). Threshold events in spring discharge: evidence from sediment and continuous water level measurement. *Journal of Hydrology*, 351(1-2), 98-106.
- Hosseini SM, Ataie-Ashtiani B, Simmons CT (2017) Spring hydrograph simulation of karstic aquifers: Impacts of variable recharge area, intermediate storage and memory effects. *J Hydrol* 552:225–240. doi: 10.1016/j.jhydrol.2017.06.018
- Husic A, Fox JF, Agouridis C, Currens JC, Ford WI, Taylor CJ (2017a) Sediment carbon fate in phreatic karst (Part 1): Conceptual model development. *J Hydrol* 549:179–193. doi: 10.1016/j.jhydrol.2017.03.052
- Husic A, Fox JF, Ford WI, Agouridis C, Currens JC, Taylor CJ (2017b) Sediment carbon fate in phreatic karst (Part 2): Numerical model development and application. *J Hydrol* 549:208–219. doi: 10.1016/J.JHYDROL.2017.03.059
- Husic A, Fox J, Adams E, Backus J, Pollock E, Ford W, Agouridis C (2019a) Inland impacts of atmospheric river and tropical cyclone extremes on nitrate transport and stable isotope measurements. *Environ Earth Sci* 78:1–21. doi: <https://doi.org/10.1007/s12665-018-8018-x>
- Husic A, Fox J, Ford W, Agouridis C, Currens J, Backus J (2019b) Nitrate Pathways, Processes, and Timing in an Agricultural Karst System: Development and Application of a Numerical Model. *Water Resour Res* In Review
- Jain, S. C. (2001). *Open-channel flow*. John Wiley & Sons.

- Jeannin, P. Y. (2001). Modeling flow in phreatic and epiphreatic karst conduits in the Hölloch cave (Muotatal, Switzerland). *Water Resources Research*, 37(2), 191-200.
- Jouves, J., Viseur, S., Arfib, B., Baudement, C., Camus, H., Collon, P., & Guglielmi, Y. (2017). Speleogenesis, geometry, and topology of caves: A quantitative study of 3D karst conduits. *Geomorphology*, 298, 86-106.
- Klimchouk, A. (2004). Towards defining, delimiting and classifying epikarst: Its origin, processes and variants of geomorphic evolution. *Speleogenesis and Evolution of Karst Aquifers*, 2(1), 1-13.
- Kovács A, Perrochet P (2008) A quantitative approach to spring hydrograph decomposition. *J Hydrol* 352:16–29. doi: 10.1016/j.jhydrol.2007.12.009
- Kresic, N. (2010). Types and classifications of springs. In *Groundwater hydrology of springs* (pp. 31-85). Butterworth-Heinemann.
- Lamarche, J., Lavenu, A. P., Gauthier, B. D., Guglielmi, Y., & Jayet, O. (2012). Relationships between fracture patterns, geodynamics and mechanical stratigraphy in Carbonates (South-East Basin, France). *Tectonophysics*, 581, 231-245.
- Lamb, H. (1932). *Hydrodynamics*, § 156. Aufl., Cambridge: Univ. Press 1879–1932.
- Landrum, C., Castrignanò, A., Mueller, T., Zourarakis, D., & Zhu, J. (2013, March). LANDSCAPE SCALE ASSESSMENT OF SOIL MOISTURE VARIABILITY USING AUXILIARY SENSING TECHNOLOGIES AND MULTIVARIATE GEOSTATISTICS. In *Kentucky Water Resources Annual Symposium* (p. 33).
- Long, J., Gilmour, P., & Witherspoon, P. A. (1985). A model for steady fluid flow in random three-dimensional networks of disc-shaped fractures. *Water Resources Research*, 21(8), 1105-1115.
- Long, A. J. (2009). Hydrograph separation for karst watersheds using a two-domain rainfall-discharge model. *Journal of Hydrology*, 364, 249– 256. <https://doi-org.ezproxy.uky.edu/10.1016/j.jhydrol.2008.11.001>
- MacQuown, W. C., & Dobrovolny, E. (1968). Geologic map of the Lexington East quadrangle, Fayette and Bourbon Counties, Kentucky (No. 683).
- Malagò, A., Efstathiou, D., Bouraoui, F., Nikolaidis, N. P., Franchini, M., Bidoglio, G., & Kritsotakis, M. (2016). Regional scale hydrologic modeling of a karst-dominant geomorphology: the case study of the Island of Crete. *Journal of Hydrology*, 540, 64-81.
- Malard, A., Jeannin, P. Y., Vouillamoz, J., & Weber, E. (2015). An integrated approach

- for catchment delineation and conduit-network modeling in karst aquifers: application to a site in the Swiss tabular Jura. *Hydrogeology Journal*, 23(7), 1341-1357.
- Massei, N., Wang, H. Q., Dupont, J. P., Rodet, J., & Laignel, B. (2003). Assessment of direct transfer and resuspension of particles during turbid floods at a karstic spring. *Journal of hydrology*, 275(1-2), 109-121.
- Matthäi, S. K., & Belayneh, M. (2004). Fluid flow partitioning between fractures and a permeable rock matrix. *Geophysical Research Letters*, 31(7).
- McCoy, K. J., & Kozar, M. D. (2008). Use of sinkhole and specific capacity distributions to assess vertical gradients in a karst aquifer. *Environmental geology*, 54(5), 921-935.
- McFarlan, A. C. (1943). *Geology of Kentucky*. University of Kentucky.
- Mein, R. G., & Larson, C. L. (1973). Modeling infiltration during a steady rain. *Water resources research*, 9(2), 384-394.
- Miller, R. D. (1967). *Geologic map of the Lexington West quadrangle, Fayette and Scott Counties, Kentucky*: US Geol. Survey Geol. Quad. Map GQ-600.
- Montieth, J. L. (1965). Evapotranspiration and environment. in 'The state and movement of water in living organs'. In *Soc. Exp. Biol. Symp.* (Vol. 19, pp. 206-234). Cambridge University Press.
- Moody, L. F. (1944). Friction factors for pipe flow. *Trans. Asme*, 66, 671-684.
- Moriasi, D. N., Arnold, J. G., Van Liew, M. W., Bingner, R. L., Harmel, R. D., & Veith, T. L. (2007). Model evaluation guidelines for systematic quantification of accuracy in watershed simulations. *Transactions of the ASABE*, 50(3), 885-900.
- Munson, Bruce Roy, Theodore Hisao Okiishi, Wade W. Huebsch, and Alric P. Rothmayer. *Fluid mechanics*. Singapore: Wiley, 2013.
- Muskat, M., Wyckoff, R. D., Botset, H. G., & Meres, M. W. (1937). Flow of gas-liquid mixtures through sands. *Transactions of the AIME*, 123(01), 69-96.
- Neitsch, S. L., Arnold, J. G., Kiniry, J. R., & Williams, J. R. (2011). *Soil and water assessment tool theoretical documentation version 2009*. Texas Water Resources Institute.
- Niswonger, R. G., Prudic, D. E., & Regan, R. S. (2006). Documentation of the unsaturated-zone flow (UZf1) package for modeling unsaturated flow between the land surface and the water table with MODFLOW-2005 (No. 6-A19).

- Nsonguh Tibouo, F. (2016). Use and Evaluation of LiDAR for Mapping Sinkholes in Royal Spring Groundwater Basin.
- Palanisamy B, Workman SR (2014) Hydrologic Modeling of Flow through Sinkholes Located in Streambeds of Cane Run Stream, Kentucky. *J Hydrol Eng* 20:04014066. doi: 10.1061/(ASCE)HE.1943-5584.0001060
- Paylor R, Currens JC (2004) Royal Springs Karst Groundwater Travel Time Investigation. A report prepared for Georgetown Municipal Water and Sewer Service. Lexington, KY
- Phillips, J. D., & Walls, M. D. (2004). Flow partitioning and unstable divergence in fluviokarst evolution in central Kentucky. *Nonlinear Processes in Geophysics*, 11(3), 371-381.
- Phillips, J. D. (2015). Badass geomorphology. *Earth Surface Processes and Landforms*, 40(1), 22-33.
- Pinault, J. L., Plagnes, V., Aquilina, L., & Bakalowicz, M. (2001). Inverse modeling of the hydrological and the hydrochemical behavior of hydrosystems: characterization of karst system functioning. *Water Resources Research*, 37(8), 2191-2204.
- Puckett, J. (2015). Qualitative and Quantitative Characteristics of Fluvial Karst Features in the Cane Run Watershed.
- Reimann, T., Giese, M., Geyer, T., Liedl, R., Maréchal, J. C., & Shoemaker, W. B. (2014). Representation of water abstraction from a karst conduit with numerical discrete-continuum models. *Hydrology and Earth System Sciences*, 18(1), 227-241.
- Ritchie, J. T. (1972). Model for predicting evaporation from a row crop with incomplete cover. *Water resources research*, 8(5), 1204-1213.
- Rooij, R., Perrochet, P., & Graham, W. (2013). From rainfall to spring discharge: Coupling conduit flow, subsurface matrix flow and surface flow in karst systems using a discrete-continuum model. *Advances in water resources*, 61, 29-41.
- Sawyer AH, Zhu J, Currens JC, Atcher C, Binley A (2015) Time-lapse electrical resistivity imaging of solute transport in a karst conduit. *Hydrol Process* 29:4968–4976. doi: 10.1002/hyp.10622
- Shah RA, Jeelani G, Jacob N (2017) Estimating mean residence time of karst groundwater in mountainous catchments of Western Himalaya, India. *Hydrol Sci J* 62:1230–1242. doi: 10.1080/02626667.2017.1313420

- Sharpley, A. N., & Williams, J. R. (1990). EPIC-erosion/productivity impact calculator: 1. Model documentation.
- Shoemaker, W. B., Cunningham, K. J., Kuniandy, E. L., & Dixon, J. (2008). Effects of turbulence on hydraulic heads and parameter sensitivities in preferential groundwater flow layers. *Water resources research*, 44(3).
- Simunek, J., Sejna, M., Van Genuchten, M. T., Šimůnek, J., Šejna, M., Jacques, D., ... & Sakai, M. (1998). HYDRUS-1D. Simulating the one-dimensional movement of water, heat, and multiple solutes in variably-saturated media, version, 2.
- Sloan, P.G. and I.D. Moore. 1984. Modeling subsurface stormflow on steeply sloping forested watersheds. *Water Resources Research*. 20(12): 1815-1822.
- Smart, P. L., & Friedrich, H. (1986). Water movement and storage in the unsaturated zone of a maturely karstified carbonate aquifer, Mendip Hills, England, paper presented at the Environmental Problems in Karst Terrains and Their Solutions Conference, Natl. Water Well Assoc., Bowling Green, Ky.
- Snow, D. T. (1969). Anisotropic permeability of fractured media. *Water Resources Research*, 5(6), 1273-1289.
- Spangler LE (1982) Karst hydrogeology of northern Fayette and southern Scott counties, Kentucky. University of Kentucky
- Talarovich, S. G., & Krothe, N. C. (1998). Three-component storm hydrograph separation of a karst spring contaminated by polychlorinated biphenyls in central Indiana. *Environmental Geosciences*, 5(4), 162-176.
- Taylor CJ (1992) Ground-water occurrence and movement associated with sinkhole alignments in the Inner Bluegrass Karst Region of central Kentucky. University of Kentucky
- Thraillkill, J., & Gouzie, D. R. (1984). Discharge and travel time determinations in the Royal Spring groundwater basin, Kentucky.
- Thraillkill, J., Sullivan, S. B., & Gouzie, D. R. (1991). Flow parameters in a shallow conduit-flow carbonate aquifer, Inner Bluegrass Karst Region, Kentucky, USA. *Journal of Hydrology*, 129(1-4), 87-108.
- Nsonguh Tibouo, F. (2016). Use and Evaluation of LiDAR for Mapping Sinkholes in Royal Spring Groundwater Basin.
- Tritz, S., Guinot, V., & Jourde, H. (2011). Modelling the behaviour of a karst system catchment using non-linear hysteretic conceptual model. *Journal of hydrology*, 397(3-4), 250-262.

- UKAg (University of Kentucky Agriculture Weather Center) (2007). Research farm climate data. https://www.wagwx.ca.uky.edu/ky/data.php#Spindletop_Farm_Data. Accessed 6 Jan 2018
- UKCAFE (University of Kentucky College of Agriculture Food and the Environment) (2011). Cane Run and Royal Spring watershed-based plan, version 5. EPA Project Number C9994861-06. In: Univ. Kentucky Coll. Agric. Food Environ. www.bae.uky.edu/CaneRun/PDFs/Cane_Run_WBP_2011.pdf. Accessed 6 Jan 2018
- White, W. B. (1999). Conceptual models for karstic aquifers. *Karst modeling*, 5, 11-16.
- White, W. B. (2002). Karst hydrology: recent developments and open questions. *Engineering geology*, 65(2-3), 85-105.
- Williams, J.R. 1969. Flood routing with variable travel time or variable storage coefficients. *Transactions of the ASAE* 12(1):100-103.
- Williams, J. R., & Hann Jr, R. W. (1973). HYMO: Problem-oriented computer language for hydrologic modeling; users manual. ARS S US Agric Res Serv South Reg.
- Williams, P. W. (2008). The role of the epikarst in karst and cave hydrogeology: a review. *International Journal of Speleology*, 37(1), 1.
- Worthington SRH (2007) Groundwater residence times in unconfined carbonate aquifers. *J Cave Karst Stud* 69:94–102
- Worthington, S. R. H., & Ford, D. C. (2009). Self-organized permeability in carbonate aquifers. *Groundwater*, 47(3), 326-336.
- Xu, Z., Bassett, S. W., Hu, B., & Dyer, S. B. (2016). Long distance seawater intrusion through a karst conduit network in the Woodville Karst Plain, Florida. *Scientific reports*, 6, 32235.
- Yactayo, G. A. (2009). Modification of the SWAT model to simulate hydrologic processes in a karst-influenced watershed (Doctoral dissertation, Virginia Tech).
- Zhang Z, Chen X, Soulsby C, Cheng Q (2018) Storage dynamics, hydrological connectivity and flux ages in a karst catchment: conceptual modelling using stable isotopes. *Hydrol Earth Syst Sci* 23:51–71. doi: 10.5194/hess-23-51-2019
- Zhu J, Currens JC, Dinger JS (2011) Challenges of using electrical resistivity method to locate karst conduits-A field case in the Inner Bluegrass Region, Kentucky. *J Appl Geophys* 75:523–530. doi: 10.1016/j.jappgeo.2011.08.009
- Zimmerman, R. W., & Yeo, I. W. (2000). Fluid flow in rock fractures: From the Navier-

Stokes equations to the cubic law. Geophysical Monograph-American Geophysical Union, 122, 213-224.

Vita

Ethan Luke Adams, EIT
Place of Birth: Lexington, KY

Education:

M.S. Civil Engineering, University of Kentucky (currently enrolled).
Advisor: Dr. James Fox
Emphasis: Water Resources Engineering
B.S. Civil Engineering, University of Kentucky, 2017.
B.S. Physics, Eastern Kentucky University, 2017.

Employment

Engineer in Training, Kentucky Department of Highways, Jackson, KY (2019 – Present)
Graduate Assistant, University of Kentucky, Lexington, KY (2017 – 2019)
Survey Technician, Vaughn and Melton Consulting Engineers, Lexington, KY (2016)
Engineering Technician, Blake Adams Engineering, Stanton, KY (2011 – 2015)

Awards and Recognitions

Outstanding University Scholars Student Award (2017)
University of Kentucky University Scholar (2017)
Recipient of the Fish Scholarship (2016)
Recipient of the Kentucky Dpt. of Highways Engineering Scholarship (2016)
Recipient of the Henry Mason Lutes Scholarship (2015)
Recipient of the ECU Regents Scholarship (2012-2015)
Powell County High School Valedictorian (2012)

Professional Publications

Gerlitz, M., Adams, E., Bettel, L., Husic, A., Fox, J., Ford, W., ... & Agouridis, C. 2.6 Measuring and Modeling Morphologic Processes in Karst to Sustain Water Resources in the Future. In *Proceedings of 2019 Kentucky Water Resources Annual Symposium*.

Husic, A., Fox, J., Adams, E., Ford, W., Agouridis, C., Currens, J., & Backus, J. (2019). Nitrate Pathways, Processes, and Timing in an Agricultural Karst System: Development and Application of a Numerical Model. *Water Resources Research*, 55(3), 2079-2103.

Husic, A., Fox, J., Adams, E., Backus, J., Pollock, E., Ford, W., & Agouridis, C. (2019). Inland impacts of atmospheric river and tropical cyclone extremes on nitrate transport and stable isotope measurements. *Environmental earth sciences*, 78(1), 36.

Husic, A., Fox, J., Pollock, E. D., Ford III, W. I., Agouridis, C., Taylor, C. J., ... & Adams, E. (2018, December). Nitrate Removal in a Phreatic Karst Conduit: Estimating Nitrification and Denitrification Rates using Stable Isotopes and Numerical Modeling. In *AGU Fall Meeting Abstracts*.